Institut für Materialphysik im Weltraum

Annual Report 2014

DLR

Institut für
Materialphysik im Weltraum

Deutsches Zentrum für Luft- und Raumfahrt

Annual Report 2014

Impressum:
Institut für Materialphysik im Weltraum
Deutsches Zentrum für Luft- und Raumfahrt (DLR)
51170 Köln

Tel. +49 2203 601 2331
Fax: +49 2203 61768
e-mail: materialphysik@dlr.de

Cover image: Team of the Institute of Materials Physics in Space during the 24th DLR Parabolic Flight Campaign, Bordeaux, February 2014. The institute flew three experiments on this campaign: TEMPUS electromagnetic levitation, X-ray investigation in space environment (X-RISE), and electrostatic levitation (μg-ESL). From left to right: Christian Neumann, Isabell Jonas, Sina Asmus, Stefan Klein, Andreas Meyer, Florian Kargl, Sarah Eiteljorg, Marc Engelhardt, Stephan Schneider, Dirk Bräuer, David Heuskin, Juliane Schmitz, Jonas Valloton, Elke Sondermann, Georg Lohöfer, Maike Becker, William Hembree (Universität des Saarlandes, Saarbrücken, Germany), Stefanie Koch, Natalie Jacobs, Doug Matson (Tufts-University, USA)

Contents

1 Reports

1.1 Methods Development

Electrostatic levitation in microgravity – containerless processing of liquid metals

C. Neumann, D. Bräuer, I. Jonas,* S. Zimmermann, and A. Meyer
Institut für Materialphysik im Weltraum, Deutsches Zentrum für Luft- und Raumfahrt (DLR), 51170 Köln, Germany

Electrostatic Levitation allows for containerless processing and therefore for contactless measurements on liquid metal alloys and other sample material. Such a sample is levitated stably in an electrostatic field. To defeat the disturbing influence of gravity to these measurements a set-up to perform electrostatic levitation in microgravity (μg) is engineered within an in-house development project at our institute [1].

First μg-experience was gained when the instrument was operated on the 24th DLR parabolic flight campaign (PFC) aboard novespaces' A300 ZERO-G in February 2014. The hardware was integrated into a purpose-built rack structure meeting all PFC-requirements (Fig. 1).

FIG. 1: μg ESL integrated and operated during its maiden flight on the 24th parabolic flight campaign.

Since there is no three-dimensional potential minimum as Earnshaws Theorem states, an active position control for the sample is essential. This fact makes within others an electrostatic levitator (ESL) a technically most challenging and consuming method. It is in fact more complicated to realize than for electromagnetic-, aerodynamic- or ultrasonic levitation. However, speaking from the scientific point of view electrostatic levitation is the most suited method to investigate certain thermo physical properties of liquid materials. A small positioning force as well as a decoupling of levitation and heating make it a suitable method for investigations over a broad temperature range.

However, the 24^{th} parabolic flight campaign revealed, that the 3D position detecting system was due to a redesign. The position sensitive photodiodes which work reliably in lab environment have proved imprecise in μg environment facing thermal drift, vibration and increased g-levels.

Hence, these have been replaced by a CCD camera system using realtime image processing for measuring the sample position in three dimensions.

Furthermore the instrument was rebuilt into a 17" payload for MAPHEUS-05 (Fig. 2) including all subsystems, computing power and electrical power supply needed to carry out multiple experiments during one single flight. This sounding rocket flight configuration was tested at the drop tower, ZARM Bremen [2]. More drops with this configuration are due in January 2015 to prepare the maiden flight on MAPHEUS-05.

FIG. 2: μg ESL in MAPHEUS-05 flight configuration

In the future properties like density, surface tension, or viscosity can be examined. For viscosity measurements the oscillating drop technique is used, where an additional sinusoidal voltage is applied, which excites the sample to oscillate in a frequency near its eigenfrequency.

---

[*] Corresponding author: `isabell.jonas@dlr.de`
[1] DLR-MP - Annual Report 2013
[2] ZARM - Zentrum für angewandte Raumfahrttechnologie und Mikrogravitation, Universität Bremen

Development of a High Temperature Gradient Furnace (HGF) for X-RISE

S. Grüter, S. Klein,* and F. Kargl

Institut für Materialphysik im Weltraum, Deutsches Zentrum für Luft- und Raumfahrt (DLR), 51170 Köln, Germany

Advanced computational models of solidification need sophisticated experimental data and techniques. To this end, in-situ sample monitoring techniques provided an important step forward in recent years. In this context the study of microstructure formation during solidification using X-ray radiography (XRR) on thin film samples is now state of the art. Using this technique, grain nucleation, growth kinetics and concentration field evolution are accessible [1].

The recent development of a tiltable microfocus X-ray facility X-RISE [2] and an isothermal furnace for XRR [3] lead to promising results in understanding equiaxed dendritic growth in Al-Ge based alloy systems. However, from a technological point of view understanding the transition from columnar to equiaxed (CET) dendrite growth is imporant. For instance, for near net-shape casting the productivity could be increased by processing close to the CET at the risk of growing equiaxed instead of columnar as requested for superalloy single crystal turbine blades [4]. CET being obviously one of the major challenges in casting processes is affected by temperature gradients, growth velocities, and concentration pile ups in front of the columnar growth front. In order to increase our capabilities in this field of research a high temperature gradient furnace (HGF) is developed. This furnace shall enable us to investigate columnar growth and the CET. Combining the HGF with the tiltable facility X-RISE convective fluid flow effects can be varied or even be strongly suppressed. A systematic investigation of the CET therefore becomes possible.

The developed HGF is schematically presented in figure 1. The furnace design was based on the following requirements: The HGF shall withstand temperatures up to 1200 K. The selected material shall take into account temperature and reactivity of the melt, as well as ensure minimal absorption of X-ray beam passing through the sample by the furnace. Temperature gradients of at least up to 10 K mm^{-1} were equally key as a precise sample translation to set well defined growth velocities. The displayed multi-layered highly symmetric furnace concept was constructed by utilizing CATIA ® and verified by thermal FEM analysis using ANSYS ®.

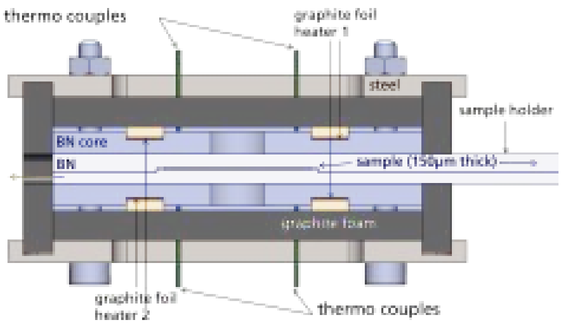

FIG. 1: Schematic cross section of the HGF

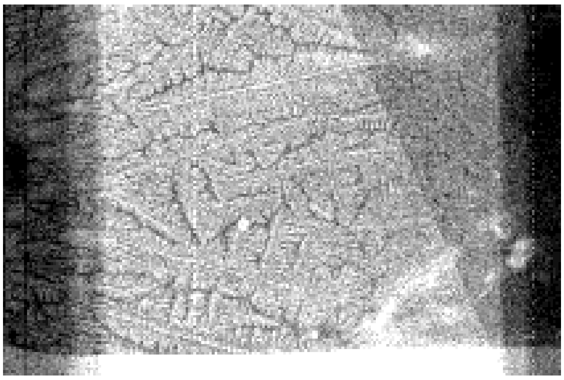

FIG. 2: XRR image of a Al-Ge sample molten and solidified by using the prototype HGF

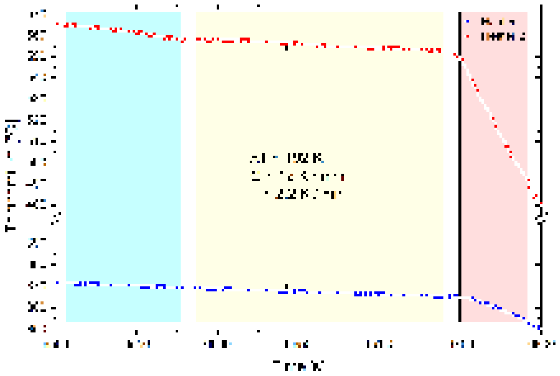

FIG. 3: Temperature-Time profile of the cooling phase of the Al-Ge alloy. The distance between the thermo couples is about 16 mm.

To experimentally verfiy this concept a prototype was built and first experiments were carried out on Al-based alloys. A XRR image of an as solidified Al-Ge alloy is presented in figure 2. This sample was solidified unter three different growth velocities by settin different cooling rates as shown in figure 3. The transformation in microstructure from cellular to columnar to equiaxed (left to right in figure 2 follows these changes.

We would like to thank all colleagues and in particular the workshop team; K. Afanasev, H. Esser, R. Henrichs, and M. Nell.

* Corresponding author: `stefan.klein@dlr.de`

[1] A.G. Murphy, D.J. Browne, W.U. Mirihanage, and R.H. Mathiesen, Acta Mater. **61**, 4595 (2013).
[2] A. Knipstein, Bachlor Thesis 2012.
[3] M. Becker, S. Klein, and F. Kargl, Annual Report 2014.
[4] A. Ludwig, I. Wagner, J. Laakmann, and P.R. Sahm, Materials Science and Engineering: A **178**, 299 (1994)

Temperature-Time Behavior of Metallic Melts Processed in Micro Gravity Levitators

G. Lohöfer*

Institut für Materialphysik im Weltraum, Deutsches Zentrum für Luft- und Raumfahrt (DLR), 51170 Köln, Germany

For investigations on high temperature metallic melts electromagnetic levitation is a well-established processing technique, which uses high frequency magnetic fields for a contactless, inductive positioning and heating of electrically conducting samples. The operation of this technique under microgravity (μg), provided by the "International Space Station" (ISS) or on board of aircrafts during parabolic flights, avoids in addition all disadvantages of this method, like turbulent fluid flows in and deformations of the levitated liquid samples, which result from the strong electromagnetic force fields necessary to support the droplet against gravity.

In preparing scientific experiments performed in the μg levitation facilities "TEMPUS" and "EML", which are used on board of aircrafts during parabolic flights and in the ISS, respectively, an important aspect within this program is the prediction of the temperature-time behavior $T(t)$ of the processed samples of mass m and specific heat c_p, described by the heat balance

$$mc_p dT/dt = P^{ind}(t) - P^{rad}(T) - P^{con}(T) - P^{flow}(T),$$

with the power input $P^{ind}(t)$, induced by the high frequency electromagnetic levitation fields, and the power losses by heat radiation $P^{rad}(T)$, heat conduction $P^{con}(T)$ through the surrounding helium or argon process atmosphere, and forced gas flow $P^{flow}(T)$. A sketch of the levitated sample is shown in Fig. 1.

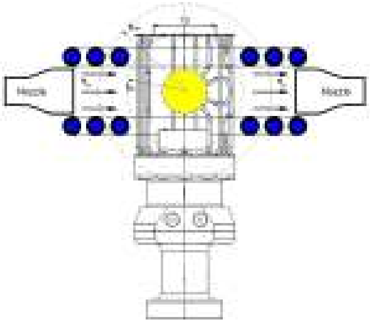

FIG. 1: Sketch of the sample (yellow) enclosed in a cage and levitated by the high frequency magnetic fields of TEMPUS between the horizontal, circular coil windings (black circles).

In Ref. [1] we already provided the necessary theoretical background for the inductive heat input by the high frequency magnetic levitation fields and the heat loss due to radiation. Subject of the present work is the detailed study of the heat loss of a sample under the additional influence of heat conduction [2] and forced gas flow in the surrounding process atmosphere.

Due to the relatively high thermal diffusivities of the process gases (He or Ar), the *conductive* heat loss from the sample of radius a to the nearby heat sinks (cage pedestal and coil) can simply be considered as stationary. Thus it can be described by [2]

$$P^{con}(T) = \frac{4\pi a}{1 - a/b_g} \frac{\lambda_{0,g}}{\alpha_g + 1} (T^{\alpha_g + 1} - (300K)^{\alpha_g + 1}),$$

where $\lambda_{0,g}$ and α_g are known gas type dependent parameters and where b_g is a gas and facility specific constant, to be determined by a calibration experiment.

Convective gas cooling means, that a heat flow, transported by diffusion (conduction) from the hot sample through the gas to the cold heat sink, is enhanced by a superposed movement of the hot gas. For gases of high thermal conductivity, like helium, and low flow velocities the resulting power loss can be considered as that one of the pure heat conduction plus a small disturbance from to the gas flow

$$P^{flow}(T) = C_g a^3 p_\infty^2 v_\infty^2 \left(1 - (300K/T)^{1+\alpha_g}\right).$$

Here p_∞ and v_∞ are the pressure and the flow speed of the atmosphere far from the sample. Again we have a gas and facility specific constant C_g, which has to be determined by a calibration experiment

Both power loss functions are checked and the calibration parameters are determined by a fit to experimental data, see Fig. 2, obtained from sample cooling tests with a solid zirconium sphere in the TEMPUS levitation facility during two μg parabolic flights in Sept. 2013 and Oct. 2014 under different atmospheric conditions (vacuum, static gas, gas flow at different velocities).

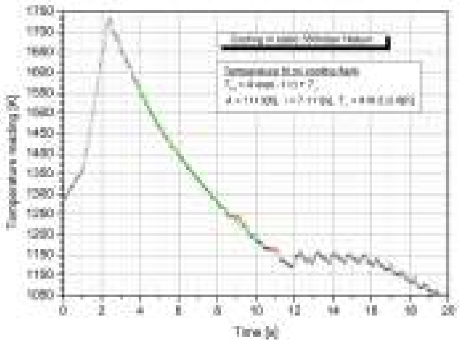

FIG. 2: Temperature-time profile (black circles) of the solid zirconium test sphere processed in TEMPUS during the 20s μg time of a parabola in a static 350mbar Helium atmosphere with a theoretical fit function to the data points (green line).

Figure 2 shows exemplarily that both power loss functions fit perfectly to the experimental data.

---

* Corresponding author: `Georg.Lohoefer@dlr.de`

[1] G. Lohöfer and I. Egry, High Temp. - High Press. **42**, 175 (2013).

[2] G. Lohöfer and S. Schneider, to appear in High Temp. - High Press. (2015).

Software for Tracking Dendrites in Equilibrium Solidification

Marcus Reinartz* and Stefan Klein

Institut für Materialphysik im Weltraum, Deutsches Zentrum für Luft- und Raumfahrt (DLR), 51170 Köln, Germany

The observation of microstructure evolution during solidification by using X-ray radiography produces a huge amount of video data. Analysing these data is time-consuming. A program is presented, which speeds up this process by semi-automated data processing. Using this program increases the amount of analysed data thereby leading to a better statistical significance.

To detect the tips of the dendrites in a video it is processed through the following steps (cf. image series in Fig. 1):
1) A region of interest (ROI) is cut out of the image. The ROI best contains only one nucleation spot. Cropping also reduces the time requirement for further processing.
2) The cropped images are denoised. The noise in the images makes it for the tracking algorithm nearly impossible to find the dendrite tips. Denoising is a crucial step in image processing. The noise is visibly reduced with the tips conserved though the subtleties of the branches vanish.
3) Thresholding transforms the image to a black-white image. The tip shape is rather insensitive on the threshold. Only for very low or very large values the whole image becomes completely white or black, respectively.
4) The final and not necessarily required step in image preparation is applying edge detection to the thresholded image. The "'Canny-edge-detector"' algorithm is used, which calculates gradient strength and direction for each point [2].
5) The first images showing no clear dendrite arms are typically deleted to enable proper dendrite arm detection. The algorithm is applied to the first image of the remaining video and searches for strong corners (dendrite tips are the strongest curved corners in the image). The determination is run iteratively by searching strong corners in every image and comparing these to the previous image. Saving these in arrays containing the coordinates of a corner for every image dendrite tracks can be extracted. From these values dendrite tip velocities can be derived as shown in Fig. 2. Calculating the velocity for every fifth image gives a smoother profile.

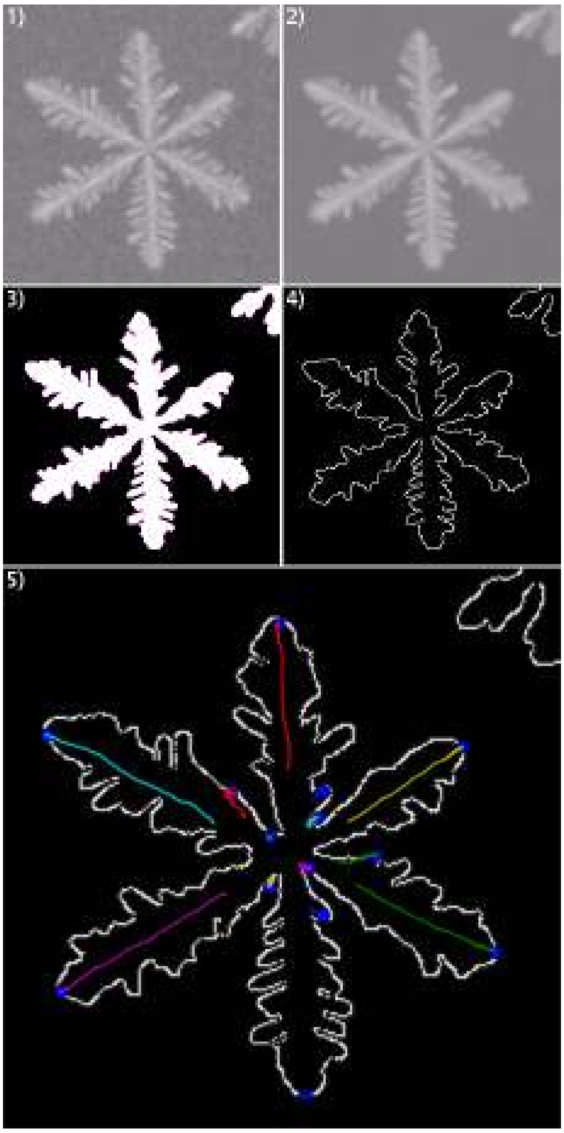

FIG. 1: The sequence of images through the analysis procedure is shown: 1) raw data as saved from the video, 2) noise reduced image, 3) denoised image after thresholding, 4) edge-image derived from the thresholded image, and 5) detected pathways (colored) of dendrites through the melt

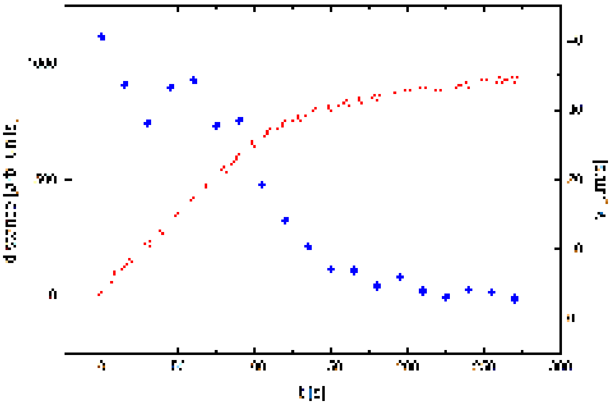

FIG. 2: Distance (red open symbols) and primary dendrite arm velocities (blue diamonds) as function of time. The data were extracted averaged over five images.

---

* Corresponding author: `marcus.reinartz@dlr.de`

[1] B.D. Lucas and T. Kanade, IJCAI, 674 (1981)
[2] J. Canny, PAMI **8**, 679 (1986)

TEMPUS parabolic flight campaigns

D. Heuskin,[*] S. Schneider, J. Schmitz, M. Engelhardt, G. Lohöfer, S. Eiteljorg, S. Asmus, D. Bräuer, S. Klein, S. Zimmermann, and J. Wessing

Institut für Materialphysik im Weltraum, Deutsches Zentrum für Luft- und Raumfahrt (DLR), 51170 Köln, Germany

With the facility "TEMPUS" (Containerless Electro-Magnetic Processing Under Microgravity conditions) electrically conductive samples of diverse alloy systems can be processed in reduced gravity. Without contact to container materials, samples are positioned by electromagnetic fields generated by a coil of 18 mm in diameter. A heating field is also produced by these coils and heats and melts the sample. While still positioned, the heater field is then switched off and the sample cools down. It remains liquid (and in most cases undercools even below its melting point) until it solidifies by chance or triggering. Before it solidifies a variety of stimulation can be applied while at the same time diagnostic tools monitor the temperature and capture video clips from the sample and measure diverse other housekeeping data. Those are used to determine thermophysical properties of the examined sample, like viscosity and surface tension, thermal expansion, or other. For this kind of measurements the oscillating drop method is used, where surface oscillations are triggered by heater pulses. From the damping of these oscillations the viscosity can be deduced and from their frequency the surface tension is calculated. The rapid advancement of phases solidifying and microstructure forming out of the undercooled melt are captured by a separate high speed camera.

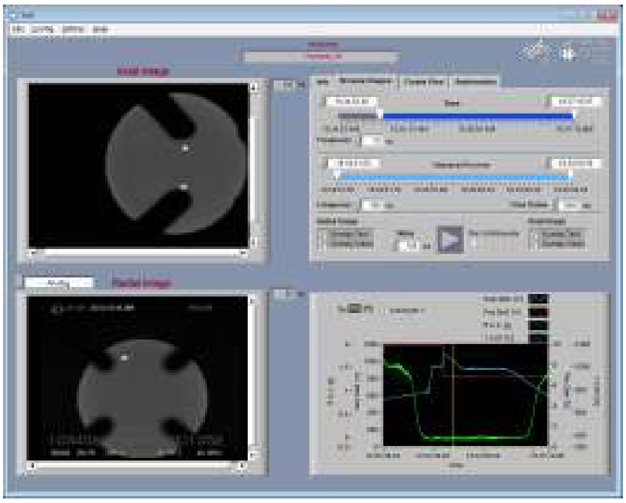

FIG. 2: Experiment with sawtooth pulses on the Zr-Ni sample. Radial (top left side) and axial (bottom left) video recording. Video settings are on the upper right side, telemetry data on the bottom right side. They comprise temperature (blue), heater (yellow) and positioner (red) voltages, and g-level (green).

In 2014, TEMPUS was flown in February and October during the 24th and 25th DLR parabolic flight campaigns. In total, the facility was operated during 8 flight days on 248 parabolas. During those, research on 44 experiment proposals from ESA, DLR-RFM, and DLR-MP could be performed. On both campaigns, the first flight days were dedicated to the observation of sample solidification, where measurements were conducted with the radial camera in high speed mode. On the other flight days this camera was used in the mode for oscillation measurement.

FIG. 1: TEMPUS experiment on last A300 Zero-G parabolic flight. The next campaign will be on the upcoming A310 Zero-G.

Aside the scientific aims some technical aspects were investigated and optimised. This included the automated recalescence detection, sample stimulation with a sawtooth shaped pulseform and the investigation of the cooling efficiency of the circulating gas system in Ar atmosphere. Measurements of the electrical conductivity with use of the SCE (sample coupling electronic) were performed on all samples. Various pulse durations were applied to investigate a possible reduction of beat frequencies. The newly employed Si_3N_4 sample holder cups showed a better thermoshock resistance compared to the former Al_2O_3 ones.

The parabolic flight campaigns are also required for the qualification of ISS EML samples demonstrating their levitation and positioning behaviour.

We would like to thank all principal investigators for their good cooperation, the space agencies DLR and ESA for the support of the campaign and W. Dreier for the fruitful discussions.

---

[*] Corresponding author: `david.heuskin@dlr.de`

Conduction of EML experiments onboard the ISS

J. Schmitz,[1,*] S. Schneider,[1] and A. Diefenbach[2]

[1] *Institut für Materialphysik im Weltraum, Deutsches Zentrum für Luft- und Raumfahrt (DLR), 51170 Köln, Germany*
[2] *DLR MUSC, Deutsches Zentrum für Luft- und Raumfahrt (DLR), 51170 Köln, Germany*

Since this year, the electromagnetic levitation facility (EML) is available onboard ISS. This device for containerless processing of metallic or semiconducting samples has been installed during Alexander Gerst's mission and enables a large scientific community to measure thermophysical properties or solidification processes in microgravity with high accuracy. On orbit, experiment durations are accessible which easily exceed those provided by parabolic flights or sounding rockets.
EML has been put into operation by performing first experiments on a Zr sample. These experiments were part of the facility commissioning and reveal the functionalities of EML, as required for scientific experiments. They give an impression of the facility performance and allow for a consolidated experiment planning.

The number and complexity of the experiments, which shall be performed in EML, are quite challenging. This is the reason why an accompanying ground support programme is necessary for support of the scientific community in planning and conduction of the experiments. In this ground support programme sample characteristics like evaporation, emissivities and coupling to the electromagnetic field were determined. With these data and the experiment concept in mind, the semi-automated experiments have been developed and written down in so-called experiment parameter sets. Lately, for the first batch of scientific EML experiments, their performance has been tested and validated in the ground based "Operational Model" of EML. During these tests the correct settings of the facility subsystems and the expected time flow of the melt cycles were verified.

FIG. 1: On orbit installation of EML. Assembly of last components to the Experiment Module, supported at MUSC.

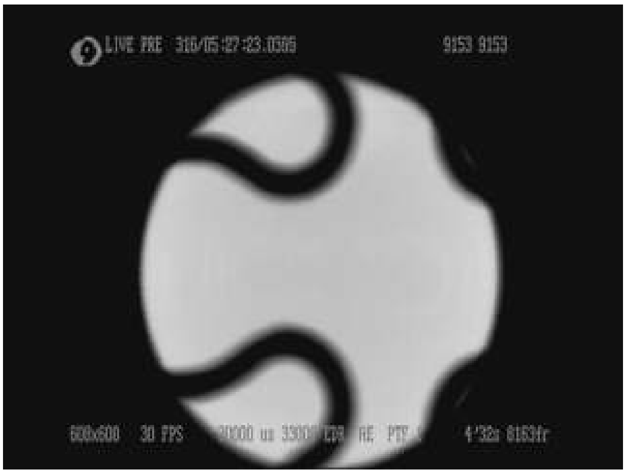

FIG. 2: Radial live video recording of the Zr sample during the facility checkout experiment (FCE). The dark patterns are wires of the cage, covering each sample.

All of these steps have already been performed for the facility checkout experiment (FCE), which was recently conducted on a solid Zr sample. In this experiment, engeneering aspects were tested, mainly the sample positioning capability with different positioning forces and perturbations.

The translational stability was good, even at low positioning forces, when no sample excitations were induced. By application of heating pulses the sample was pushed out of the equilibrium position. The effect was strong for higher heater pulses and lower positioning forces. It seems, that avoiding instantaneous heater changes by utilization of a continuous heater increase can hold the sample steady.
Sample cooling can be realized by a circulating gas flow, directed to the sample. The efficiency of He and Ar gas for cooling was shown, while almost no sample displacement was observed.
Video recording with multiple settings, sample visibilities, and download was tested for both, the axial an the radial cameras.
Also the flawless automated experiment conduction was checked, as the scientific experiments will be controlled by time and temperature limits and include automated stimuli like heater pulses or modulations.

Based on these findings further investigations will be conducted and the planned experiments will presumably be amended.

[*] Corresponding author: `Julianna.Schmitz@dlr.de`

1.2 Liquid and Melt Properties

Interdiffusion in Al-Ni alloys measured with the new high-temperature shear-cell

K. Binder and F. Kargl*

Institut für Materialphysik im Weltraum, Deutsches Zentrum für Luft- und Raumfahrt (DLR), 51170 Köln, Germany

Al-Ni base alloys exhibit a broad application area, thus they are an object of intensive research. The interdiffusion coefficients for these alloys have been predicted by molecular dynamic simulations (MDS) [1] and have been measured by long-capillary [2] and shear-cell experiments [3]. Due to the high melting-point for higher Ni-concentrations, reliable experimental data are so far only available for low Ni-concentrations ($\leq 14\,at\%$).

To overcome this limitation a novel shear-cell furnace was constructed that enables in-situ studies with X-ray radiography up to temperatures of $2073\,K$. This alumina based furnace enables processing of three diffusion-couples. The shear-cell is heated by molybdenum-meander-wire heaters and a layered graphite-foil interface between crucible and the heater improves temperature homogeneity. To reduce heat loss the complete furnace is mounted in a graphite-foam insulation. For long-time experiments the furnace is water-cooled. The shearing-bar (SB) is laterally connected and the temperature measured in the top-centre position (Inset Fig.1). Here, first experiments on Al-Ni at 22.5, 17.5 and $12.5\,at.\%$ Ni content are reported carried out at a temperature of $1423\,K$. Horizontal arrangement of the mean compositions in the furnace (cf. inset Fig.1) follows the mentioned order from left to right.

Table I shows interdiffusion coefficients of the Al-Ni interdiffusion couples following the same analyses procedure as described by Kargl et al. [4]. The data are shown for two time periods. The first period $10-100\,s$ is characterised by heating power fluctuations leading to convective flow inside the diffusion couple. The effective diffusion coefficients are increased. For the second time-period the heating power was stable. Only existing temperature-gradients in the furnace could lead to additional flow.

For Al-Ni $12.5\,at.\%$ differences in the diffusion coefficients derived for different parts of the sample appear to be minor. This points to only small disturbances. For the other two diffusion couples differences between the diffusion coefficients (left, middle, right) are still significant. This indicates that the measurements are disturbed by convective flow. This can be rationalized as follows. The shearing-bar is in contact with the shear-cell during the entire measurement acting as a thermal bridge. The thermocouple for measuring temperature is positioned near the top of the diffusion couples. Both lead to temperature gradients triggering Marangoni-flow. The Al-Ni $22.5\,at.\%$ diffusion couple is more strongly influenced being closer to the shearing bar and subjected to a lager temperature gradient.

area	period (s)	Ni at. % 10 vs 15	15 vs 20	20 vs 25
entire	10-100	10.57(1)	8.075(4)	8.262(4)
	150-300	**6.25(8)**	6,76(6)	11.1(1)
left	10-100	14.04(5)	12.30(1)	13.11(4)
	150-300	**5.36(4)**	10.7(5)	16.0(6)
middle	10-100	11.21(2)	6.754(9)	8.748(5)
	150-300	**6.6(2)**	9.1(2)	9.9(3)
right	10-100	6.88(1)	7.156(5)	5.675(8)
	150-300	**7.3(3)**	2.41(8)	8.5(1)

TABLE I: $D_{int} \cdot 10^{-9}\,\frac{m^2}{s}$ in Al-Ni alloys at 1423K

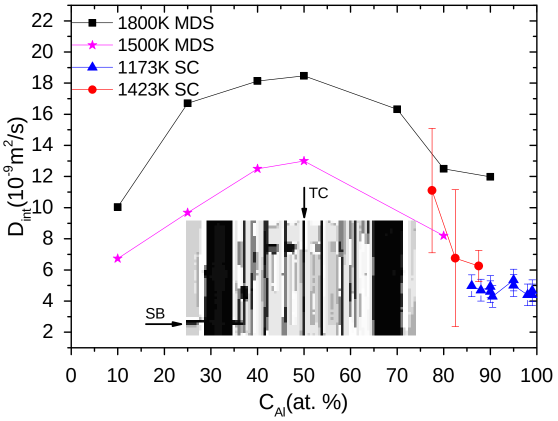

FIG. 1: Interdiffusion-coefficients in Al-Ni: MD simulation data taken from [1] (squares, stars), X-ray data at $1173\,K$ taken from [3] (triangles) and data of this work (dots). The picture-inset shows a XRR-image of the shear-cell furnace post shearing. Positions tagged by arrows: top-center: thermocouple (TC), lateral: shearing-bar (SB)

For Al-Ni $12.5\,at.\%$, which is largely unaffected by convective flow, a comparison with data of Sondermann et al. [3] shows good agreement considering temperature difference. For the lager Ni concentration the mean values of the diffusion coefficient data appear to follow the trend set by the MD simulation [1].

To conclude high-temperature interdiffusion coefficients measurements are possible with this furnace if the identified disturbance are reduced. In particular, a reduction of thermal gradients can be achieved by contacting the cell with the SB only during shearing and positioning of the thermocouple towards the top of the shear cell.

We acknowledge Airbus D&S for partial funding.

* Corresponding author: `florian.kargl@dlr.de`

[1] P.Kuhn et al. *Phys Rev B* **90**, 024309 (2014).
[2] J.Horbach et al. *Phys Rev B* **75**, 174304 (2007).
[3] E. Sondermann et al. *to be published*.
[4] F. Kargl et al. *High Temp. - High Press.* **42**, 3–21 (2013).

Influence of cross correlations on interdiffusion in Al-rich Al-Ni melts

E. Sondermann,* F. Kargl, and A. Meyer

Institut für Materialphysik im Weltraum, Deutsches Zentrum für Luft- und Raumfahrt (DLR), 51170 Köln, Germany

For the relation between interdiffusion and selfdiffusion in a binary system, Darken's equation is a widely used approximation. It connects the interdiffusion coefficient D_{AB} with the self-diffusion coefficients D_A and D_B and corresponding concentrations c_A and c_B using the thermodynamic factor Φ. A correction factor S is introduced to this equation to account for cross correlations arising from collective processes.

$$D_{AB} = \Phi S(c_B D_A + c_A D_B) \tag{1}$$

For low concentrations Φ and S are expected to approach unity and consequently D_{AB} should approach the self-diffusion coefficient of the minority component.

Here, we report on the measurement of interdiffusion in Al-rich Al-Ni melts. The interdiffusion coefficients were measured using a shear cell in combination with X-ray radiography (XRR). Within a shear cell the two parts of a diffusion pair are melted separately. This avoids segregation and flow induced by melting. XRR allows for time resolved *in-situ* measurements and detailed process control. Measurements were performed with sample diameters of 1.0 and 1.5 mm in order to check the influence of convection. Convection is stronger in samples with larger diameter.

Fig. 1 shows an almost constant interdiffusion coefficient in Al-Ni melts for Ni-concentrations between 1 and 14 at.% at 1173 K of 4.7·10^{-9} m^{2}s^{-1}. Experiments with 1.0 and 1.5 mm sample diameter give the same results within error bars. Therefore, the measurements are expected to be undisturbed by convective flow.

Self-diffusion coefficients for Nickel in Al-Ni are interpolated for T=1173 K from quasi-elastic neutron scattering (QENS) done by Meyer *et al.* [1]. As aluminum is a very weak inelastic scatterer and there is a lack of suitable isotopes, D_{Al} can be measured neither by QENS nor by classical long capillary methods.

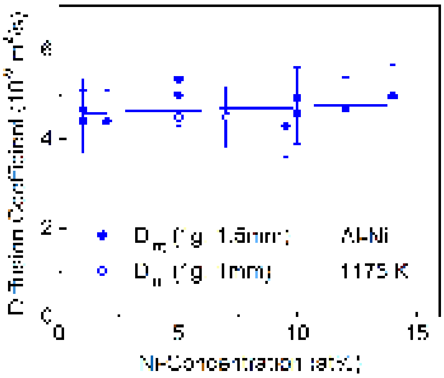

FIG. 1: Interdiffusion coefficients for Al-rich Al-Ni at 1173 K.

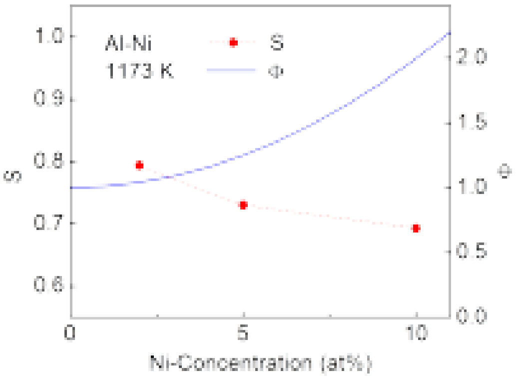

FIG. 2: Thermodynamic Factor Φ derived from [3] and cross correlation term S calculated from Φ and experimental values of Self- and Interdiffusion coefficients for Al-rich Al-Ni at 1173 K.

To apply equation 1 to our measurements we assume $D_{Al} = D_{Ni}$. This assumption is supported by computer simulations that show $D_{Al} \approx D_{Ni}$ at 1173 K [2]. Slight deviations can be neglected because D_{Al} is multiplied by the small value of c_{Ni}.

The thermodynamic factor Φ for liquid Al-Ni at 1173 K was calculated from the second derivative of Gibbs free energy with respect to concentration. Gibbs free energy was modeled from thermodynamic properties of Al-Ni by Ansara *et al.* [3]. As can be seen in fig. 2, Φ starts as expected at 1 for pure aluminum and rises with increasing Ni-content to about 2 at 10 at.% Ni.

Using the QENS and interdiffusion measurement data, findings of thermodynamic calculations and assuming $D_{Al} = D_{Ni}$, it is possible to calculate the cross correlation term S. Fig. 2 shows that S is below unity, which is typical for systems that exhibit a chemical short-range ordering. This is the case for liquid Al-Ni. S increases with decreasing Ni-content. Other than predicted [2], S is considerably below unity even for 2 at.% Ni.

This indicates, that in Al-Ni melts 2 at.% Ni cannot be regarded as a small concentration. Interdiffusion is reduced, compared to Ni-selfdiffusion. Smaller Ni-concentration is required to obtain $D_{AlNi} \approx D_{Ni}$.

* Corresponding author: `elke.sondermann@dlr.de`

[1] A. Meyer and F. Kargl and T. Unruh, unpublished.
[2] J. Horbach, unpublished.
[3] I. Ansara and N. Dupin and H. L. Lukas and B. Sundman, J. Alloy. Compd. **247**, 20 (1997).

Diffusion and Interdiffusion in Binary Metallic Melts

P. Kuhn,[1] J. Horbach,[2] F. Kargl,[1] A. Meyer,[1] and Th. Voigtmann[1]

[1] *Institut für Materialphysik im Weltraum, Deutsches Zentrum für Luft- und Raumfahrt (DLR), 51170 Köln, Germany*
[2] *Soft Matter Laboratory, IPKM, Heinrich-Heine Universität Düsseldorf, Universitätsstr. 1, 40225 Düsseldorf, Germany*

Mass transport processes in dense melts are governed by highly cooperative phenomena. In the case of binary mixtures, the self-diffusion coefficient D^s_α describes long-range transport of a tracer particle (of a given species α), and a single inter-diffusion coefficient D_{cc} describes the decay of concentration fluctuations on large scales. The Darken equation proposes a relation between these coefficients,

$$D_{cc} = L \cdot \Phi \approx [x_{\mathrm{B}} D^s_{\mathrm{A}} + x_{\mathrm{A}} D^s_{\mathrm{B}}]\,\Phi\,, \tag{1}$$

where x_α are the number concentrations. L is the Onsager kinetic coefficient. The thermodynamic factor Φ is connected to the second derivative of the Gibbs free energy G w.r.t. the concentrations.

We have investigated model binary melts at various temperatures and composition by molecular-dynamics (MD) computer simulation using recent embedded-atom potentials for Al-Ni and Zr-Ni [1]. The simulations allow to decompose the different contributions to mass transport; in particular to the inter-diffusion coefficient. A key result from these simulatons is that their composition dependence is qualitatively different, so that interdiffusion processes are described by a competition of two opposing forces, a dynamic and a thermodynamic one. The dynamic contribution can be understood as the precursor of kinetic arrest and consequently depends sensitively on control parameters.

Figure 1 shows MD simulation results for the interdiffusion coefficient in Al$_x$Ni$_{100-x}$ alloys at several temperatures. At high temperatures one observes a maximum in the interdiffusion coefficient D_{cc} as a function of composition. This concentration dependence changes qualitatively as a function of temperature. For low temperatures, the maximum observed at higher temperatures vanishes, and eventually a minimum is observed at intermediate x. Other than the interdiffusion coefficient, the self-diffusion coefficients in the MD simulation always display a minimum as a function of concentration at fixed temperature. The change in behavior observed for D_{cc} is hence the result of a kinetic slowing down and a counter-balancing increase in the thermodynamic factor Φ due to mixing. The latter dominates D_{cc} at high temperatures.

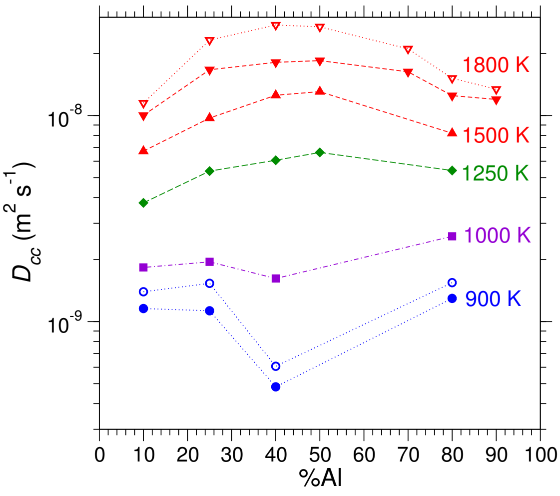

FIG. 1: Interdiffusion coefficient D_{cc} in a model Al-Ni system, from molecular-dynamics computer simulations, as a function of Al concentration at various fixed temperatures (filled symbols, as labeled). Open symbols show D_{cc} estimated from the Darken relation, Eq. (1) (without a correction, $S = 1$) for $T = 1800\,$K and $T = 900\,$K.

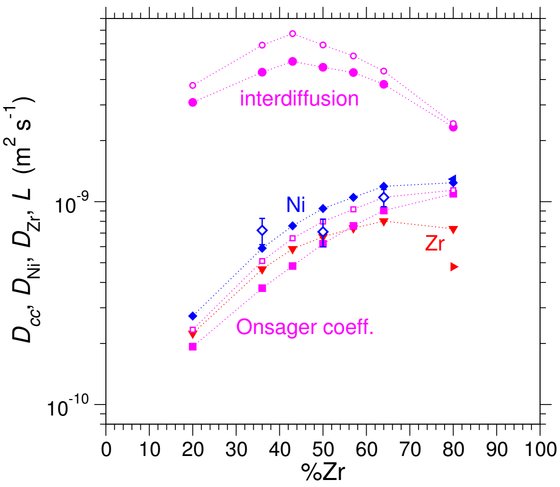

FIG. 2: Interdiffusion coefficient D_{cc} (filled circles), related Onsager kinetic coefficient L (filled squares), and self-diffusion coefficients for Ni and Zr (filled diamonds and inverted triangles), for the Zr-Ni simulation model at fixed temperature $T = 1400\,$K, as a function of Zr concentration. Open squares and circles are the Onsager coefficient and D_{cc} estimated from the Darken equation.

Also shown in Fig. 1 are estimates of D_{cc} according to the Darken equation, Eq. (1) with $S = 1$ (open symbols). While the concentration dependence is captured qualitatively correctly, the Darken equation significantly overestimates D_{cc}. This effect is more pronounced at higher temperatures, while the quantitative error made by Eq. (1) is less at lower temperatures.

Figure 2 shows simulation results for our Zr-Ni model to demonstrate that similar effects prevail in this system.

Part of this work was supported by the Helmholtz-Gemeinschaft, Helmholtz-Hochschul-Nachwuchsgruppe VH-NG 406.

[1] P. Kuhn, J. Horbach, F. Kargl, A. Meyer, and Th. Voigtmann, Phys. Rev. B **90**, 024309 (2014).

In-situ interdiffusion measurements of liquid Zr-Ni alloys

P. Heintzmann,[1, *] F. Yang,[1] F. Kargl,[1] K. Binder,[1] B. Schillinger,[2] and A. Meyer[1]

[1] *Institut für Materialphysik im Weltraum, Deutsches Zentrum für Luft- und Raumfahrt (DLR), 51170 Köln, Germany*
[2] *Forschungsneutronenquelle Heinz Maier-Leibnitz (FRMII), Technische Universität München, 85747 Garching, Germany*

Mass transport coefficients play an important role for an understanding of processes like solidification or the glass transition and are used to calibrate interaction potentials for computer simulations of liquids. Therefore precisely determined transport coefficients are highly desired. Due to a lack of reliable experimental data for binary liquid metals interdiffusion coefficients frequently are determined via *Darken's equation* [1], relating interdiffusion coefficients D_{int} with self diffusion coefficients D_s and the thermodynamic factor Φ:

$$D_{int} = \Phi(c_{Ni}D_{Zr} + c_{Zr}D_{Ni}). \qquad (1)$$

A comparison with the diffusion equation [2]

$$D_{int} = \Phi(c_{Ni}D_{Zr} + c_{Zr}D_{Ni} + \Delta_d), \qquad (2)$$

with Δ_d accounting for contributions of cross correlations, shows that Darken's equation yields a good approximation for the interdiffusion coefficient in systems where $\Delta_d \ll c_{Ni}D_{Zr} + c_{Zr}D_{Ni}$.

Recent molecular dynamics simulations on metallic Zr-Ni liquids show that Darken's equation overestimates the interdiffusion coefficient from approximately 5 % to 50% depending on the composition and temperature [3]. From mode coupling theory (MCT) calculations on the binary system $Zr_{64}Ni_{36}$, which yield values for the inter- and self-diffusion coefficients using experimental structure factors, an even larger deviation from the predictions of Darken's equation results [4]. Therefore, it is of high interest to experimentally determine diffusion coefficients of the binary Zr-Ni system.

Here we present *in-situ* interdiffusion measurements of $Zr_{64}Ni_{36}$ and $Zr_{36}Ni_{64}$. For our measurements we have used a longcapillary setup in combination with neutron and x-ray radiography. With this technique we were able to detect and rule out possible disturbing effects like convection or segregation. As interdiffusion coefficients are measured in-situ, results are independent of melting and solidification processes. To compare our results with Darken's equation we use Ni self-diffusion coefficients from quasielastic neutron scattering measurements [5]. For the Zr self-diffusion we use the Ni values, as first results from Zr tracer diffusion measurements [6], which are not completed at present, show good agreement with the Ni self-diffusion within measurement error. Together with the thermodynamic factor [7] we can check on the predictions of Darken's equation from a full set of experimental data.

The experimental interdiffusion coefficient of $Zr_{64}Ni_{36}$, see FIG. 1, is approximately a factor two larger than the Ni self-diffusion coefficient. With decreasing Zr concentration the experimental data show an increasing interdiffusion coefficient and a decreasing Ni self-diffusion coefficient, so that D_{int} is approx. a factor four larger than D_{Ni}. For both compositions a high thermodynamic factor (see FIG. 1) raises the interdiffusion above the self-diffusion coefficient, whereas effects of cross correlations Δ_d lead to a decrease of the interdiffusion coefficient. The increase of the interdiffusion coefficient with decreasing Zr is due to the increase of Φ and a decrease of the absolute value of Δ_d.

Using the shown Ni self- and interdiffusion coefficients, the thermodynamic factor [7] and Zr self-diffusion coefficients from [6] (not shown) Darken's equation leads to an interdiffusion coefficient D_{Darken} which is approx. a factor three of the experimental value. The predicted D_{Darken} is slightly decreasing with decreasing Zr and thus leads to a factor two of the experimental value. Both values are far out of experimental error bars.

With these results it is shown from a full set of experimental data, that Darken's equation significantly overestimates the value of the interdiffusion coefficient in Zr-Ni alloys. Darken's equation is based on the assumption that cross correlations of particles of different species in a liquid can be neglected. For the Zr-Ni alloys presented here this assumption does not seem to be justified.

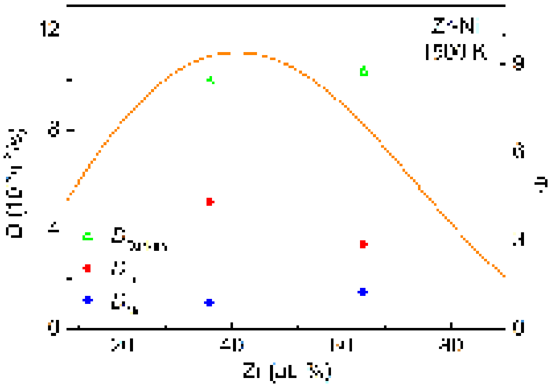

FIG. 1: Comparison of experimental Ni self-diffusion [5] and interdiffusion coefficients with predicitions from Darken's equation. As solid line the thermodynamic factor [7] is shown.

---

[*] Corresponding author: `pascal.heintzmann@dlr.de`

[1] L. S. Darken, Trans. AIME, **175**, 184, (1948)
[2] J. P. Hansen and I. R. McDonald, *Theory of Simple Fluids*, Elsevier Academic Press, (2005)
[3] P. Kuhn et al., Phys. Rev. B, **90**(2), 024309, (2014)
[4] T. Voigtmann et al., EPL **82** 66001 (2008).
[5] D. Holland-Moritz et al., J. Phys. Conf. Ser. **144**, 012119 (2009).
[6] S. W. Basuki, Universität Kiel, unpublished.
[7] G. Gosh, J. Mater. Res. **3108**, (1994).

Atomic dynamics in binary Zr-Cu liquids

F. Yang,[1,*] D. Holland-Moritz,[1] J. Gegner,[1] P. Heintzmann,[1] F. Kargl,[1] C. C. Yuan,[1] G. G. Simeoni,[2] and A. Meyer[1]

[1] *Institut für Materialphysik im Weltraum, Deutsches Zentrum für Luft- und Raumfahrt (DLR), 51170 Köln, Germany*
[2] *Heinz Maier-Leibnitz Zentrum (MLZ) and Physics Department, Technische Universität München, 85748 Garching, Germany*

The binary Zr-Cu alloys exhibit excellent glass forming ability (GFA) at several different compositions over a wide composition range. The GFA of the liquids exhibits a very strong composition dependence. For example, a composition variation of barley 3at% from $\mathrm{Zr}_{38.2}\mathrm{Cu}_{61.8}$ to $\mathrm{Zr}_{35.5}\mathrm{Cu}_{64.5}$ results in a increase of the critical casting thickness of fully amorphous samples from below 100 μm to of about 2 mm [1]. The origin of such drastic changes is poorly understood, although the liquid structure of these alloys has been studied extensively. On the other hand, liquid dynamics, which is another key parameter controlling GFA, has not been investigated experimentally yet, due to the high chemical reactivity of the Zr-based melts.

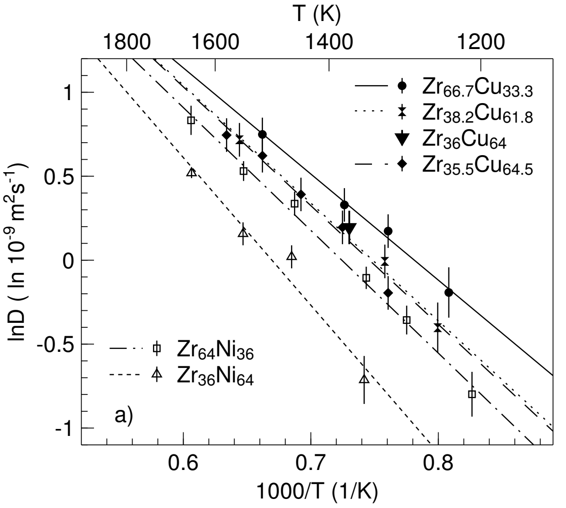

FIG. 1: Temperature dependent Cu self diffusion coefficients in Zr-Cu liquids (filled symbols). The straight lines represent Arrhenius fits. For comparison the Ni self diffusion coefficient in $\mathrm{Zr}_{36}\mathrm{Ni}_{64}$ and $\mathrm{Zr}_{64}\mathrm{Ni}_{36}$ liquids are also shown (open symbols).

We thus studied the liquid dynamics of $\mathrm{Zr}_{36}\mathrm{Cu}_{64}$, $\mathrm{Zr}_{35.5}\mathrm{Cu}_{64.5}$, $\mathrm{Zr}_{38.2}\mathrm{Cu}_{61.8}$, and $\mathrm{Zr}_{66.7}\mathrm{Cu}_{33.3}$ with QNS, in combination with both electrostatic and electromagnetic levitation (ESL and EML) [2]. The containless processing of the samples ensures no chemical contamination. These alloy compositions are chosen to investigate the effect of composition variation on the liquid dynamics of Zr-Cu and its relation to GFA. Furthermore, data can be compared with those available for the corresponding Zr-Ni alloys. Replacing Cu by Ni results in a drastic change in both liquid SRO [3, 4] and the GFA. This allows us to address whether and how this is reflected in the liquid dynamics.

The scattering experiments were carried out on the chopper time-of-flight spectrometer TOFTOF at the research neutron source Heinz Meier-Leibnitz (FRM II) in Munich, Germany. Owing to the extremely low instrumental background and the combination with containerless processing techniques, it is possible to study samples like Zr-Cu alloys with a fairly small incoherent scattering cross section ($\sigma_{\mathrm{Cu}}^{\mathrm{inc}} = 0.5\,\mathrm{barn}$). For the compositions $\mathrm{Zr}_{66.7}\mathrm{Cu}_{33.3}$, $\mathrm{Zr}_{38.2}\mathrm{Cu}_{61.8}$, and $\mathrm{Zr}_{35.5}\mathrm{Cu}_{64.5}$, the Cu self diffusion coefficients in the equilibrium melt were measured in the temperature range of 1237−1511 K, 1251−1553 K, and 1315−1578 K, respectively. We also measured the liquid $\mathrm{Zr}_{36}\mathrm{Cu}_{64}$ at 1370 K.

Fig. 1 summarises the obtained Cu self diffusion coefficients as functions of temperature. For each composition, the temperature dependent Cu self diffusion coefficient can be well described by an Arrhenius law $D(T) = D_0 \exp(-E_a/k_B T)$, where E_a is the activation energy, k_B is the Boltzmann constant, and D_0 is the diffusion coefficient at infinite temperature. It can be easily recognised in Fig. 1 that among all the Zr-Cu liquids studied here, the Cu dynamics for $\mathrm{Zr}_{35.5}\mathrm{Cu}_{64.5}$ is the slowest. At about 1315 K, the Cu self diffusion coefficient is $0.82 \pm 0.08 \times 10^{-9}$ m^{2}s^{-1} for $\mathrm{Zr}_{35.5}\mathrm{Cu}_{64.5}$ and $1.19 \pm 0.11 \times 10^{-9}$ m^{2}s^{-1} for $\mathrm{Zr}_{66.7}\mathrm{Cu}_{33.3}$. In contrast to GFA, a variation of the Cu content from $\mathrm{Zr}_{38.2}\mathrm{Cu}_{61.8}$ to $\mathrm{Zr}_{36.5}\mathrm{Cu}_{63.5}$ or $\mathrm{Zr}_{36}\mathrm{Cu}_{64}$ does not result in a measurable change of the liquid dynamics. Apparently, the strong composition dependence of the GFA is not reflected in the Cu self dynamics of the equilibrium liquid. we also compared the Cu self dynamics in Zr-Cu melts with the corresponding Ni dynamics in liquid $\mathrm{Zr}_{64}\mathrm{Ni}_{36}$ and $\mathrm{Zr}_{36}\mathrm{Ni}_{64}$. Although Zr-Ni alloys exhibit generally a worse GFA, it can be seen that the Ni self diffusion is considerably lower for the corresponding composition by substituting Cu with Ni.

By further studying the densities of these melts it can be shown that the composition dependence of the atomic dynamics in Zr-Cu is governed by variation in the average atomic volume in the liquid. Also for Zr-Ni liquids, slower liquid dynamics compared to Zr-Cu is a result of a more densely packed melt. In both cases the liquid dynamics is hence not sensitive to small composition changes. Therefore, in the case of Zr-Cu alloys, the GFA is not directly correlated with the liquid dynamics and the packing density. Since, GFA is determined by both thermodynamics and kinetics, this indicate that thermodynamic aspects may play a more important role here in determining the glass formation behaviour.

[*] Corresponding author: `fan.yang@dlr.de`

[1] X. D. Wang et al., Appl. Phys. Lett., **92** 011902 (2008).
[2] F. Yang et al,, EPL **107**, 46001 (2014).
[3] D. Holland-Moritz et al., EPL **100**, 56002 (2012).
[4] I. Kaban et al., Acta Mater., **61** 2509 (2013).

Al alloying effect on dynamics of metallic glass forming liquids

C.C. Yuan,* F. Yang, F. Kargl, D. Holland-Moritz, and A. Meyer

Institut für Materialphysik im Weltraum, Deutsches Zentrum für Luft- und Raumfahrt (DLR), 51170 Köln, Germany

As a typical microalloying element, Al strongly influences the macroscopic-properties of metallic glass-forming system. For example, the glass forming ability (GFA) of $\mathrm{Zr_{50}Cu_{50}}$ melt is improved significantlly by adding only 4% Al [1]. Moreover, the strong chemical interaction of Al with transition melts (TMs) in Zr-(Cu, Co, or Ni)-Al metallic glasses (MGs) drastically decreases the compression plasticity [2]. However, the underlying microscopic mechanism for the improved GFA by microalloying is still not clear up to now. Therefore, in the present work, the viscosity and its correlation with the packing fraction of ternary liquid Zr-(Co, Ni)-Al systems are systematically discussed.

The viscosities and densities of Zr-(Co, Ni)-Al melts were measured over a large temperature range from several hundred Kelvin above the liquidus temperature down to the deeply undercooled liquid state. Measurements were carried out using electrostatic levitation (ESL) in combination with high-speed video imaging of the levitated droplets.The measurement and analysis principles are outlined in Ref. [3].

Temperature dependent melt viscosities of the ternary $\mathrm{Zr_{56}Co_{28}Al_{16}}$, $\mathrm{Zr_{56}Ni_{28}Al_{16}}$, $\mathrm{Zr_{60}Ni_{25}Al_{15}}$, and the binary $\mathrm{Zr_{66.7}Co_{33.3}}$ systems are displayed in Fig. 1. They are compared with the viscosities of $\mathrm{Zr_{64}Ni_{36}}$ [4] and of the multi-component Zr-Ti-Cu-Ni-Be system Vitrelloy 4 (Vit4) [5]. Generally, viscosities decrease with increasing temperature. Replacing Co by Ni, results in only a minor change of the melt viscosity for both the binary and ternary alloys. However, the addition of Al, obviously leads to an increase of the viscosity by a factor of three at the respective liquidus temperatures. The difference increases with decreasing temperature.

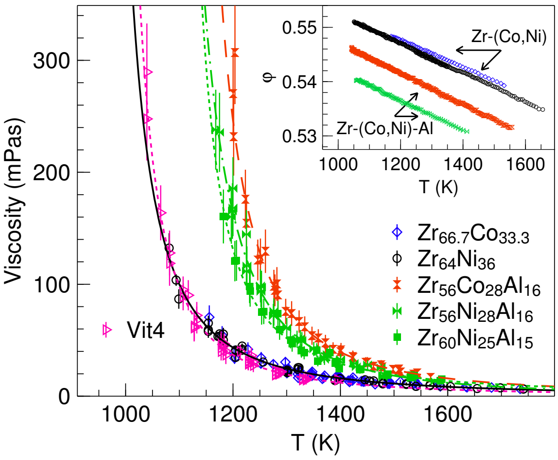

FIG. 1: Liquid viscosity of the binary alloy $\mathrm{Zr_{66.7}Co_{33.3}}$ and the ternary alloys $\mathrm{Zr_{56}Co_{28}Al_{16}}$, $\mathrm{Zr_{56}Ni_{28}Al_{16}}$, and $\mathrm{Zr_{60}Ni_{25}Al_{15}}$ as a function of temperature. The dashed lines and the solid line represent MCT fits of the data for different compositions. The inset shows the temperature dependent corresponding effective volume packing fractions.

Interestingly, compared with the Al-containing ternary alloys, the liquid viscosity of one of best glass forming systems, Vit4, is as low as the one for the Zr-(Co, Ni) binary systems at similar temperatures. It seems that the effects of other alloying elements like Ti, Cu and Be are different compared to that of Al on the dynamic behavior of Zr-based liquids.

Mode coupling theory (MCT) predictes that a small increase in the packing fraction results in rather large changes in the atomic dynamics, especially when the packing fraction is close to the the critical value [6]. Hence, effective packing fractions are further derived: $\varphi = \pi n d^3/6$, where d is an average covalent radius[7], and n is the number density per unit volume, which can be calculated from the density of a liquid, as $n = \rho N_A/\overline{M}$, N_A is the Avogadro constant, $\overline{M}$ is the average molar mass. The inset in Fig. 1 shows the resulting φ. It can be seen that φ decreases upon alloying of Al to the binary Zr-(Co, Ni) systems, and an addition of 16 at% of Al leads to a reduction of the liquid packing fraction by about 1.5%. Hence a decrease of packing density cannot explain the stiffening of the dynamics observed in our study system.

Recent simulation of binary hard-sphere liquids found that the mixing effect also has strong influence on the structual relaxation. It depends both on the size ratio (or size disparity δ) and mixing ratio of particles [8]. The addtion of intermediate size atom [the covalent radius of Al atom is 1.248 Å, which is between that of Zr (1.454 Å) and Co (1.157 Å) or Ni (1.149 Å), $\delta_{Al-Zr} = 0.86$ and $\delta_{Co-Al} = 0.93$] in binary Zr-(Co, Ni) systems will lead to much more complex effects on the dynamic behavior, therefore it can not be explained simply by the change of packing fraction based on hard-sphere (HS) model.

* Corresponding author: `chenchen.yuan@dlr.de`

[1] P. Yu, H. Bai, W. Wang, J. Mater. Res. **21**, 1674 (2006).
[2] X. K. Xi, M. T. Sandor, H. J. Wang, J. Q. Wang, W. H. Wang and Y. Wu, J. Phys.: Conden. Matter **23**, 115501 (2011).
[3] J. Brillo and I. Egry, Int. J. Thermophys. **24**, 1155 (2003).
[4] J. Brillo, A. I. Pommrich and A. Meyer, Phys. Rev. Lett. **107**, 165902 (2011).
[5] F. Yang, T. Unruh, and A. Meyer, Europhys. Lett. **107**, 26001 (2014).
[6] W. Götze, in Liquids freezing and glass transition Les Houches 1989, Sesssion L I, edited by J. Hansen, D. Levesque, and J. Zinn-Justin (North-Holland, Ams-terdam, 1991).
[7] L. Pauling, J. Am. Chem. Soc. **69**, 542 (1947).
[8] G. Foffi, W. Götze, F. Sciortino, P. Tartaglia, and T. Voigtmann, Phys. Rev. Lett. **91**, 085701 (2003).

Viscosity measurements on Vitreloy 106a bulk metallic glass

S. Zimmermann,* I. Jonas, and A. Meyer

Institut für Materialphysik im Weltraum, Deutsches Zentrum für Luft- und Raumfahrt (DLR), 51170 Köln, Germany

$Zr_{58.5}Cu_{15.6}Ni_{12.8}Al_{10.3}Nb_{2.8}$ (Vitreloy 106a) [1] is a Zr-based bulk metallic glass (BMG) with very good glass forming properties. It forms an amorphous alloy under less rapid cooling than other BMGs and has a large supercooled liquid region. Vitreloy 106a is also the first sample that will be processed in the electromagnetic levitator, which was integrated in summer 2014 on the international space station (ISS).

Electrostatic levitation was used to levitate, melt and undercool the samples. In an electrostatic levitator (ESL), the measured sample is electrically charged and floats in a vertical static electric field between two superposed electrodes. The UV radiation of a deuterium arc lamp enables the receipt of charge of the measured sample by using the photoelectric effect. Lateral avoiding of the sample is prevented by two laterally arranged electrodes, which generate two orthogonal horizontal fields. To control the sample position, two expanded laser beams are pointed at the sample and thus the emerging shadow is detected by a position sensitive detector (PSD). The great benefit of electrostatic levitation is the containerless processing, so that BMGs can be measured contactless.

The viscosity of Vitreloy 106a was investigated via ESL and oscillating drop technique at temperatures above the liguidus temperature on samples weighing less than 100 mg. In oscillating drop technique, the contactless levitating liquid sample is deformed from its spherical shape by an external pulse (see inset, FIG. 1). That effects an oscillation of the sample shape, which is damped by interior friction until the original sample shape is restored (see FIG. 1).

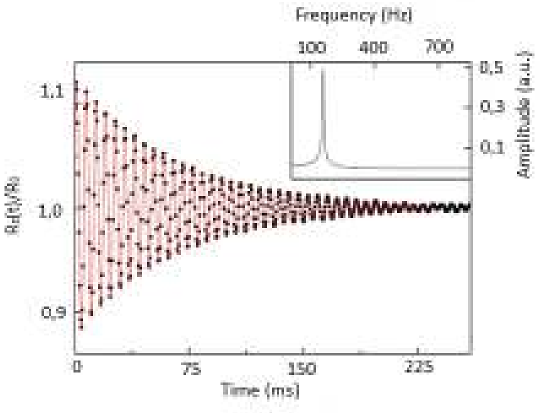

FIG. 1: The experimental data describe a product of a decaying exponential and a sine wave. The external pulse excites the sample to oscillate near its eigenfrequency (inset).

Hence, the damping constant τ is given by the decay curve, which is described by the measured data. When τ is known, the viscosity of the sample is given by

$$\eta = \frac{\rho r_0^2}{5\tau}, \qquad (1)$$

where r_0 is the radius and ρ the density of the drop [2].

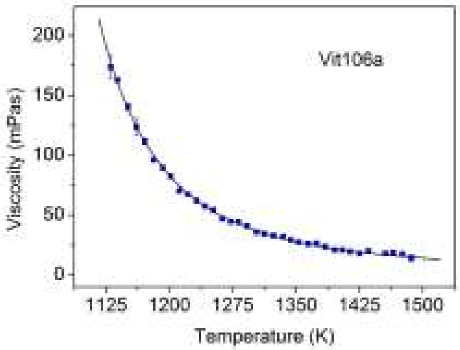

FIG. 2: Viscosity of molten Vitreloy 106a as a function of temperature, measured in an electrostatic levitator by using oscillating drop method.

The surface temperature of the sample was measured by using a single-colour-pyrometer, which assumes a constant and exact known emissivity ϵ. However, ϵ is dependent of e.g. the sample temperature and subsequently changing its value during a measurement. This leads to an offset in temperature data. A correction of the measured temperature data is given by

$$\frac{1}{T_{real}} = \frac{1}{T_{Pyro}} + \frac{1}{T_{DSC}} - \frac{1}{T_{Pyro,L}}, \qquad (2)$$

where T_{real} is the corrected temperature, T_{Pyro} the measured pyrometer temperature and $T_{Pyro,L}$ a reference temperature determined from pyrometer scan. T_{DSC} is the according reference temperature determined by differential scanning calorimetry (DSC).

Consequently, one obtains the viscosity of $Zr_{58.5}Cu_{15.6}Ni_{12.8}Al_{10.3}Nb_{2.8}$ measured in the ESL by using oscillating drop method (see FIG. 2). As expected, the viscosity is decreasing with increasing temperature.

---

* Corresponding author: `sarah.zimmermann@dlr.de`

[1] Z. Evenson, T. Schmitt, M. Nicola, I. Gallino and R. Busch, Acta Materialia 60 (2012) 4712-4719.
[2] W.-K. Rhim, K. Ohasaka, P.-F. Paradis and R. Spjut, Rev. Sci. Instrum. 70, 2796 (1999)

A handy model for the prediction of liquid-liquid interfacial energies

J. Brillo[1] and R. Schmid-Fetzer[2]

[1] *Institut für Materialphysik im Weltraum, Deutsches Zentrum für Luft- und Raumfahrt (DLR), 51170 Köln, Germany**
[2] *Institut für Metallurgie, TU-Clausthal, Robert-Koch-Strasse 42, 38678 Clausthal-Zellerfeld*

Liquid-liquid interfaces and the corresponding interfacial energies play important roles for nucleation processes. Not only that droplet nucleation is limited due to the energy costs of creating liquid-liquid interfaces, also crystal growth processes are directly affected as liquid-liquid phase separation can also act as a kinetic barrier.

The concept of the Butler equation [1], used in order to predict the surface tension of liquid alloys, provides a recipe for the derivation of an equivalent model for the prediction of liquid-liquid interfacial energies, if instead of a single bulk phase, two bulk phases (BI and BII) are considered and the interface is interpreted as a third thermodynamic phase with individual composition:

$$\sigma^{\mathrm{LL}} = (2u^{\mathrm{LL}}{}_i - \mu^{\mathrm{BI}}{}_i - \mu^{\mathrm{BII}}{}_i)A_i^{-1} \tag{1}$$

Here, A_i is the interfacial area, σ^{LL} is the liquid-liquid interfacial energy, and $\mu^{\mathrm{BI}}{}_i$ and $\mu^{\mathrm{BII}}{}_i$ are the chemical potentials of element i in bulk phase I and bulk phase II, respectively. The chemical potential in the interfacial layer is denoted by $\mu^{\mathrm{LL}}{}_i$ whereas the interfacial energy is not included, i.e. $\mu^{\mathrm{LL}}{}_i = u^{\mathrm{LL}}{}_i - 0.5\sigma^{\mathrm{LL}}A_i$.

Eq. (1) can be transformed into the following expression, whereas a_i denotes the activity of each phase:

$$\sigma^{\mathrm{LL}} = \frac{RT}{A_i} \ln\left(\frac{a_i^{\mathrm{LL},2}}{a_i^{\mathrm{BI}} a_i^{\mathrm{BII}}}\right) \tag{2}$$

In order to solve this expression, the activities need to be expressed by the partial excess free energies known from the thermodynamic assessment. It is further assumed that, like for the Butler equation, the partial excess free energies of the interface have the same functional form as for the bulk phases. One then arrives at two equations with two unkowns that can be solved numerically.

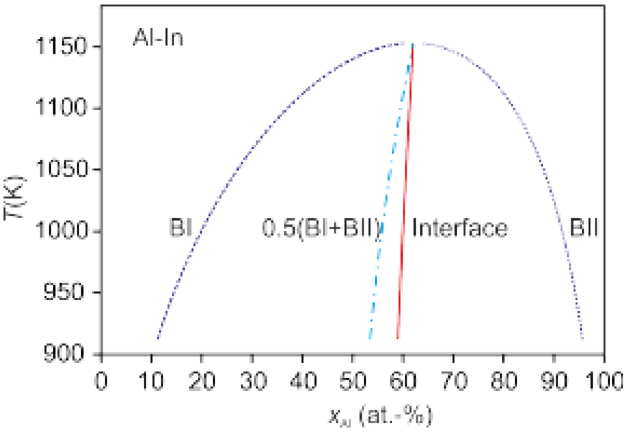

FIG. 1: Al- mole fractions of the two bulk phases, BI (dashed) and BII (dotted), as well as of the interface (solid) in demixed Al-In. The arithmetic average of the compositions of the two bulk phases is also shown (dash-dotted).

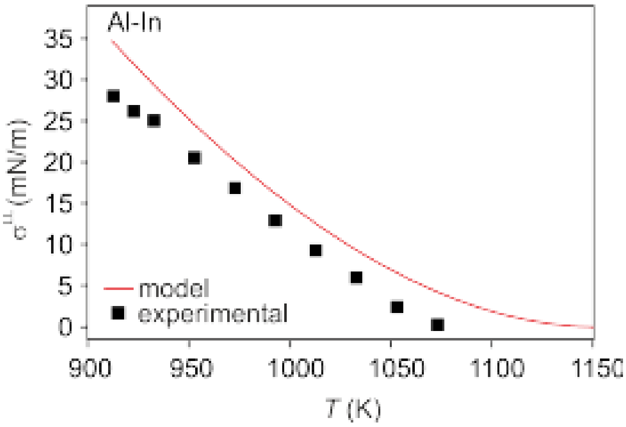

FIG. 2: Liquid-liquid interfacial energy σ^{LL} of demixed Al-In versus temperature. The symbols represent the experimental data [2] and the solid line the model.

The model is tested on the example of the binary system Al-In for which experimental liquid-liquid interfacial energies have been published by Kaban [2].

Redlich-Kister parameters of Al-In, needed in order to solve Eq. (2) are taken from [3]. Using this thermodynamic assessment, the binodal line, i.e. the temperature dependent aluminium mole fractions $x_{\mathrm{Al}}^{\mathrm{BI}}$ and $x_{\mathrm{Al}}^{\mathrm{BII}}$ of the two bulk phases, were calculated using the software package Pandat as they were needed as input parameters to the model.

FIG. 1 shows a plot of the temperature versus the mole fraction of Al in the two bulk phases, $x_{\mathrm{Al}}^{\mathrm{BI}}$ and $x_{\mathrm{Al}}^{\mathrm{BII}}$ and in the interface, $x_{\mathrm{Al}}^{\mathrm{LL}}$. $x_{\mathrm{Al}}^{\mathrm{LL}}$ hereby depends only weakly on temperature. It changes steadily from 62 to 59 at.-% with a decrease of T from 1150 K to 900 K. $x_{\mathrm{Al}}^{\mathrm{LL}}$ is, hereby, very close to the arithmetic average of the mole fractions in the bulk phases.

The calculated liquid-liquid interfacial energy of Al-In as function of temperature, is shown Fig. 2 together with the experimental data.

Although the model, Eq. (2), overestimates the experimental data slightly by ≈5 $\mathrm{mN/m}$, it correctly reproduces the temperature dependence (slope) and that, with increasing temperature, the interfacial energies asymptotically approach zero. The agreement between model and experimental data is very good for this particular system.

* Corresponding author: `juergen.brillo@dlr.de`

[1] J. Butler, Proc. Roy. Soc. **A135**, 348 (1935).
[2] I. Kaban, M. Köhler, L. Ratke, W. Hoyer, N. Mattern, J. Eckert, A. L. Greer, Acta Mat. **59**, 6880 (2011).
[3] S. S. Kim, T. H. Sanders, Modelling Simul. Mater. Sci. Eng. **14**, 1181 (2006).

Effect of Minor Additions on the Thermophysical Properties of binary Zr-Cu Melts

Z. Evenson,* F. Yang, and A. Meyer

Institut für Materialphysik im Weltraum, Deutsches Zentrum für Luft- und Raumfahrt (DLR), 51170 Köln, Germany

Bulk metallic glasses (BMGs) and are receiving much attention throughout the scientific community [1]. Binary alloys based on Zr-Cu are especially ideal for detailed studies of the glass transition in metallic systems, due to their simplicity and ability to readily vitrify under rapid quenching. Moreover, the formation of BMGs can be greatly enhanced through the minor addition of another element. For example, the addition of only 4 at.% Al or Ti to binary $Zr_{50}Cu_{50}$ increases its critical casting thickness from 2 mm to at least 5 mm [2]. Despite extensive review on this subject [3], the underlying physical mechanisms for this remain largely unknown and often speculative.

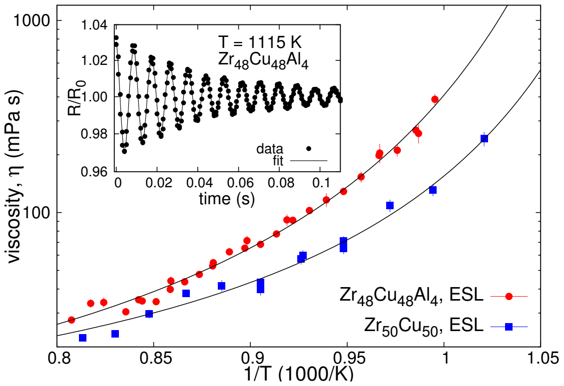

FIG. 1: Melt viscosities of the $Zr_{50}Cu_{50}$ and $Zr_{48}Cu_{48}Al_4$ liquids, determined through the oscillating drop method in ESL. The inset shows the damped oscillation of the vertical sample radius, taken at a temperature of 1115 K.

In order to gain insight into the nature of the minor alloying effect in glass-forming metallic liquids, we investigated the viscosity and specific volume of $Zr_{50}Cu_{50}$, $Zr_{48}Cu_{48}Al_4$ and $Zr_{48}Cu_{48}Ti_4$ melts using an electrostatic levitator (ESL). Since molten samples are processed contact-free in ESL, we simultaneously avoid melt contamination from the container and eliminate it as a potent instigator of heterogeneous nucleation. This is necessary to access the deeply undercooled liquid and investigate the melt properties over a wide temperature range.

Figure 1 shows the melt viscosities of $Zr_{50}Cu_{50}$ and $Zr_{48}Cu_{48}Al_4$, measured in ESL using the oscillating drop method. The viscosity was determined at each temperature by measuring the decay of surface oscillations induced by a sinusoidal electric field (inset, Fig. 1). We observe that the addition of only 4 at.% Al causes a significant increase in the viscosity towards lower temperatures compared to that of binary $Zr_{50}Cu_{50}$. This reflects a slowing down of the melt dynamics as a result of the minor addition of Al and might play an essential role in enhancing glass formation.

In Fig. 2, a comparison of the melt viscosity η, average atomic volume V_m and liquid packing fraction ϕ of $Zr_{50}Cu_{50}$, $Zr_{48}Cu_{48}Al_4$ and $Zr_{48}Cu_{48}Ti_4$ is shown at a reference temperature of 1004 K. Values of the covalent radii were taken from Ref. [4] and used to calculate ϕ. While the viscosity of the Al-bearing composition is almost 4 times greater than that of binary $Zr_{50}Cu_{50}$ at this temperature, the addition of the same amount of Ti has no significant effect on the melt viscosity. However, the Ti-bearing composition is clearly more densely packed with an average atomic volume smaller than that of the other two melts.

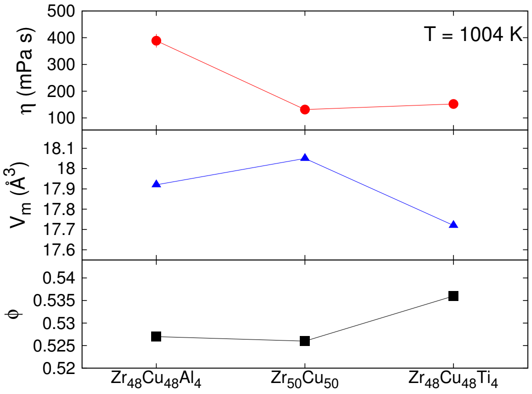

FIG. 2: Comparison of the viscosity, average atomic volume and packing fraction of the $Zr_{50}Cu_{50}$, $Zr_{48}Cu_{48}Al_4$ and $Zr_{48}Cu_{48}Ti_4$ liquids at T =1004 K.

Obviously, the effect of minor additions on the viscosity of $Zr_{50}Cu_{50}$ is more complex than simple considerations based on atomic packing. Instead, contributions from chemical interactions are expected to play a much more important role in the liquid dynamics via chemical short-range order. It is therefore necessary to examine how the minor addition affects the liquid properties on the atomic level in order to gain valuable clues to its role in enhancing glass formation.

Z. E. would like to recognize the German Academic Exchange Service (DAAD) for their financial support.

* Corresponding author: `zachary.evenson@dlr.de`

[1] A. L. Greer, Mater. Today **12**, 14 (2009).
[2] P. Yu, H. Bai, M. Tang, and W. H. Wang, J. Non-Cryst. Solids. **351**, 1328 (2005).
[3] W. H. Wang, Prog. Mater. Sci. **52**, 540 (2007).
[4] L. Pauling, J. Am. Chem. Soc. **69**, 542 (1937).

Dynamics in bulk metallic glasses

I. Jonas,* F. Yang, and A. Meyer

Institut für Materialphysik im Weltraum, Deutsches Zentrum für Luft- und Raumfahrt (DLR), 51170 Köln, Germany

Zr-based bulk metallic glass (BMG) forming alloys show a broad range of glass forming abilities and compositional complexities. They all show a moderately strong liquid behaviour near T_g and a fragile behaviour above their respective liquidus temperature. [1] The composition of a BMG determines its glass forming ability. Single elements, like Aluminium can have an impact on the glass forming ability and influence the dynamics of a system. The origin is unknown here and not jet understood [2]. Therefore it is currently under investigation, as shown in Fig 1.

The ternary alloy Inoue 3 consisting of $Zr_{60}Cu_{25}Al_{15}$ is a good glass former. Inoue 4 with the quarter composition of $Zr_{65}Cu_{17.5}Ni_{10}Al_{7.5}$ however is known to be an excellent glass former. Their cooling curves do not vary much from each other. The only slight difference is Inoue 4 undercools approximately 50 K more, down to $\sim 890K$. The corresponding melt viscosities of Inoue 3 and 4 were measured in an electrostatic levitator (ESL) using the oscillating drop technique.

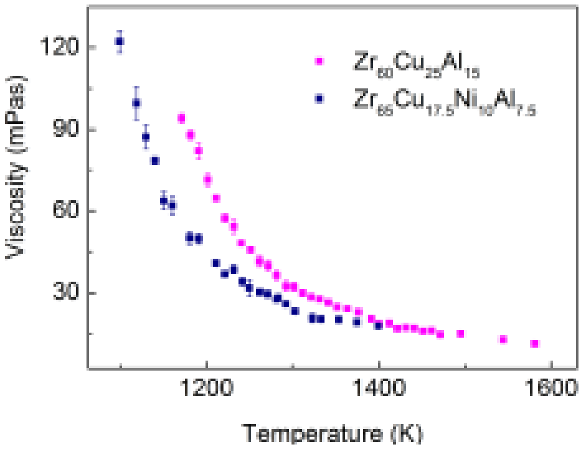

FIG. 1: Melt viscosities of $Zr_{60}Cu_{25}Al_{15}$ and $Zr_{65}Cu_{17.5}Ni_{10}Al_{7.5}$ as a function of temperature, measured with oscillating drop technique in an electrostatic levitation.

Fig.1 shows the obtained melt viscosities. A doubling of the Aluminium content (Inoue 3) leads to an increase in viscosity towards lower temperatures, by a approximate factor of 2. This indicates slow dynamics of Al-rich systems in the proximity of their melting temperature. Thus, the system with better glass forming abilities shows higher viscosities.

From the kinetic point of view it was first assumed that good glass formers would require slow dynamics, meaning they possess a low or diminishing atomic mobility upon undercooling. For the formation of crystals upon cooling, nucleation sites need to form and structures need to be reordered. If this is would be prevented by a low atomic mobility, there is no time for reordering and the system solidifies in a amorphous structure instead.

Now, this is in contrast the melt viscosities Inoue 3 and 4 display.

But from the thermodynamic point of view there are still other influencing factors, like the driving force for crystallization. Also dynamics at the respective melting point should be considered. Therefore the data was standardize to their respective liquidus temperature. This reduced the difference in melt viscosities slightly, but did not explain the phenomenon.

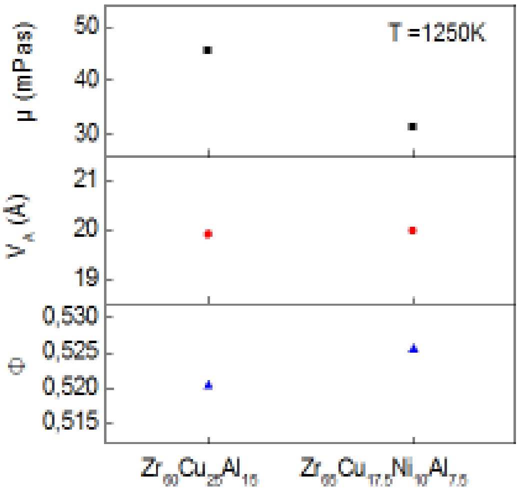

FIG. 2: Comparison of viscosity, atomic volume, and packing fraction of $Zr_{60}Cu_{25}Al_{15}$ and $Zr_{65}Cu_{17.5}Ni_{10}Al_{7.5}$ at T = 1250K.

Fig.2 shows a comparison of the melt viscosity μ, atomic volume V_A, and packing fraction ϕ of $Zr_{60}Cu_{25}Al_{15}$ and $Zr_{65}Cu_{17.5}Ni_{10}Al_{7.5}$ at 1250 K. While $Zr_{65}Cu_{17.5}Ni_{10}Al_{7.5}$ is more densely packed then $Zr_{60}Cu_{25}Al_{15}$, both compositions have the same atomic volume. Therefore the difference in viscosity can not be explained by packing effects. Ordering in the liquid or chemical interactions may give reason to this effect. It might prevent or delay the formation of rather complex crystal structures.

Further investigations are necessary to examine the effect described above in liquid BMGs and also why especially Aluminium favour this effect.

* Corresponding author: `isabell.jonas@dlr.de`

[1] Z. Evenson et al., Acta Materialia , **60**, 4712-4719 (2012).
[2] W.H. Wang, Prog. Mater.Sci.**52**, 540-596 (2007).

Experimental determination of Temperature-Time-Transformation diagrams of Zr-based glass forming alloys

S. Koch,[1,*] M. Rettenmayr,[2] P. Galenko,[2] and D. M. Herlach[1]

[1] *Institut für Materialphysik im Weltraum, Deutsches Zentrum für Luft- und Raumfahrt (DLR), 51170 Köln, Germany*
[2] *Otto-Schott-Institut für Materialforschung, Friedrich-Schiller-Universität Jena, 07743 Jena, Germany*

Crystallization kinetics of $Zr_{57}Cu_{15.4}Ni_{12.6}Al_{10}Nb_5$ (Vit 106) and $Zr_{58.5}Cu_{15.6}Ni_{12.8}Al_{10.3}Nb_{2.8}$ (Vit 106a) were studied in the electrostatic levitation apparatus. The sluggish crystallization kinetics of these bulk glass forming alloys enable the determination of the temperature-time-transformation (TTT) diagram between glass transition and liquidus temperature. Zr-based glass forming alloys of different compositions are chosen for the experiments to study the influence of composition on the TTT behavior.
To prevent heterogeneous nucleation on container walls, levitation techniques are practical. Electrostatic levitation (ESL) enables containerless melting and high undercooling of metallic samples. Specimens in a diameter of 3mm and with a weight of 30-100 mg are processed ultra-high vacuum. The experiments offer the benefit to process the sample under ultra-clean environment and to determine parameters like cooling rate, ratio of specific heat and emissivity from the cooling curves measured contactless by a pyrometer.
Temperature-time-transformation curves show the kinetics of phase formation of various phases individually involved in solidification of undercooled melts in multicomponent multiphase alloys. The ideal TTT curve is supposed to be measured by cooling the sample to a certain temperature at an infinite cooling rate and holding the temperature while measuring the fraction of crystallization at different times. The recalescence of a liquid sample marks the beginning of crystallization. In practice it is difficult to measure the TTT curve of molton metallic materials because it requires a containerless process and longtime of measurement. The upper branch of the TTT curve can be measured by free cooling in ESL with different sample mass to obtain various cooling rates. By heating an amorphous sample from room temperature to a certain crystallization temperature the under part of the TTT curve can be received.

The Fig. 1 shows a TTT diagram of Vitreloy 106. With increasing undercooling the thermodynamic driving force for crystallization increases and the atomic transport decreases. Therefore the TTT curve is typical C-shaped. The critical cooling rate to bypass crystallization was found to be 10 K/s. Although small differences in composition effect a quite similar TTT diagram for Vitreloy 106a, see Fig.2. The critical cooling rate required to vitrify is about 2 K/s. This composition can be vitrified by purely radiative Stefan-Boltzmann cooling in the electrostatic levitator.

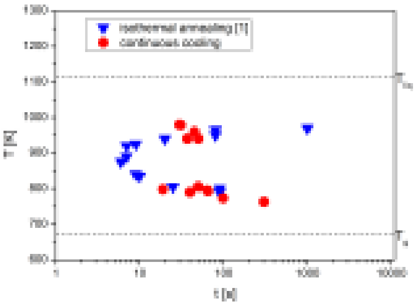

FIG. 1: Experimental TTT curve of Vitreloy 106 with T_g= 682 K, T_{liq}=1115 K, T_{nose}=880 K, t_{nose}=6 s

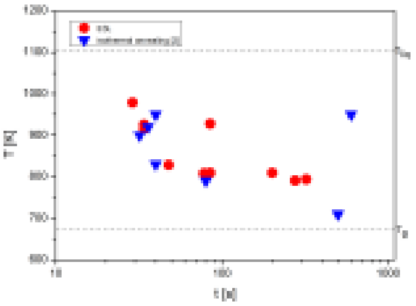

FIG. 2: Experimental TTT curve of Vitreloy 106a with T_g= 673 K, T_{liq}=1103 K, T_{nose}=900 K, t_{nose}=32 s

The next step will be to investigate the role of interfacial tension on crystallization time scales. Especially classical nucleation theory (CNT) helps to analyze the received TTT diagrams. According to CNT, the time for crystallization t_x, is given by [3]:

$$t_x = \left(\frac{3x}{\pi I_{SS} u^3}\right)^{\frac{1}{4}} \tag{1}$$

where x is the detectable volume fraction during the starting of the crystallization process (typical a value of 10^{-3} is used), I_{ss} is the steady state nucleation rate and u is the growth rate. Assuming the validity of CNT and current models of crystal growth in undercooled melts, the measured TTT diagrams can be reproduced.

The financial support by DLR Space Management within contract 50WM1140 is gratefully acknowledged.

[*] Corresponding author: `stefanie.koch@dlr.de`

[1] S. Mukherjee et al., Phys. Rev.Lett. **94**, 245501 (2005).
[2] C.C. Hays et al., Appl.Phys.Lett. **79**, 11 (2001).
[3] K.F.Kelton, Solid State Physics **45**, 75 (1991).

Density and molar volume of liquid Al-Ti alloys

J. Wessing* and J. Brillo

Institut für Materialphysik im Weltraum, Deutsches Zentrum für Luft- und Raumfahrt (DLR), 51170 Köln, Germany

Al-Ti based alloys have an enormous technical relevance. Due to their light weight, high-temperature resistance, and biocompatibility they are potential candidates for various applications in the aeronautic, automobile, and medical engineering sectors. For industrial processing the knowledge of the thermophysical properties is crucial [1]. Despite that, published thermophysical property data are sparse. One reason is the increased chemical reactivity of Ti-based materials at high temperatures. Therefore containerless processing, using levitation techniques, is the only option.

As a starting point, we chose to systematically measure the density of the system Al-Ti using the optical dilatometry method in combination with electromagnetic levitation [2].

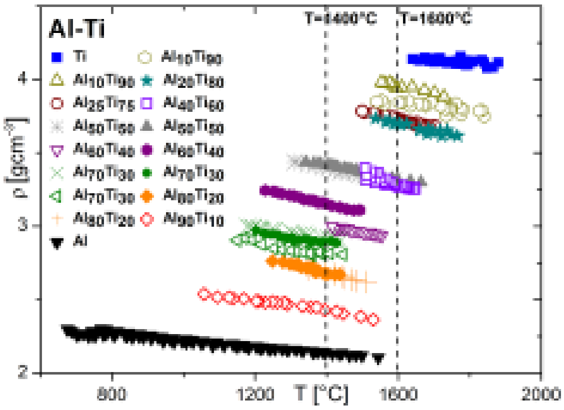

FIG. 1: Temperature dependence of the density in the $\mathrm{Al}_x\mathrm{Ti}_{1-x}$ system.

FIG. 1 shows the density ρ as function of temperature T of different $\mathrm{Al}_X\mathrm{Ti}_{1-X}$ compositions over a wide temperature range from $670\,^\circ\mathrm{C}$ to $1880\,^\circ\mathrm{C}$. For all compositions the density linearly increases with decreasing temperature. The volume expansion coefficient $\beta = -\rho_T/\rho_L$ (derived from the slopes) scatters around a constant mean value of $1.1(\pm 0.5)10^{-4}\mathrm{K}^{-1}$. The dashed lines show the corresponding linear fits according to $\rho(T) = \rho_L + \rho_T(T - T_L)$, whereas the fit parameters ρ_L and ρ_T denote the density at the liquidus temperature T_L and the temperature coefficient, respectively.

FIG. 2 shows the molar volumes derived from the molar masses and the densities at $T = 1600\,^\circ\mathrm{C}$. The dashed line represents the molar volumes of the ideal solution. The deviation between the measured and the ideal molar volume corresponds to the excess molar volume which is fitted by a Redlich-Kister polynomial of third order (solid line):

$$V_E(X_{Al}) = X_{Al}(1 - X_{Al})\left(\sum_{i=0}^{2}\right)V_i^E(2X_{Al} - 1) \qquad (1)$$

At $1600\,^\circ\mathrm{C}$ a minor positive excess molar volume occurs for $X_{Al} < 0.2$. For larger Aluminum concentrations the excess molar volume takes a negative value with a minimum around $\mathrm{Al}_{50}\mathrm{Ti}_{50}$. The inset shows the fitted excess molar volume $V_E(X_{\mathrm{Al}})$ for different temperatures. With increasing temperature the maximum negative excess molar volume increases while the maximum positive excess molar volume decreases until it becomes zero at temperatures below $1400\,^\circ\mathrm{C}$. However, it should be considered that all V_E values are calculated from Eq. 1 and lay partially outside of the actual measured temperature range (solid symbols for measured T-range). As for $1600\,^\circ\mathrm{C}$ and $X_{Al} < 0.5$ $V_E(X_{\mathrm{Al}})$ is calculated for T below (semi open symbols in Fig. 2) and for $1400\,^\circ\mathrm{C}$ and $X_{Al} > 0.5$ above the measured temperature range due to evaporation of the sample material (open symbols).

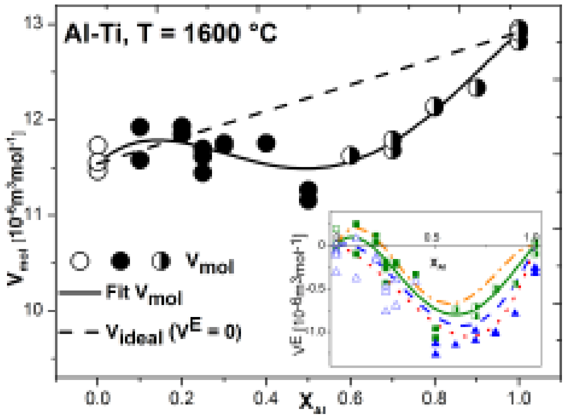

FIG. 2: Molar volumes (circles) and fitted molar volumes (dashed line) in dependence of X_{Al} at $1600\,^\circ\mathrm{C}$. Inset: Excess molar volumes (squares) and Fits (solid and dashed lines) at $1200\,^\circ\mathrm{C}$ (dotted line), $1400\,^\circ\mathrm{C}$ (dashed line), $1600\,^\circ\mathrm{C}$ (solid line) and $1800\,^\circ\mathrm{C}$ (dashed and dotted line).

Previous works on Al alloys, e.g. in the system Al-Au have shown similar results for the mixing molar volume showing significant negative values. Density measurements and MD simulations suggest that the nonideal mixing behavior occurs due to decreasing atomic radii of the Al atoms [3–5]. Future investigations will show if a similar mechanism takes place in the Al-Ti system, too.

---

* Corresponding author: `johanna.wessing@dlr.de`

[1] I. Egry et al., Int. J. Thermophys. **28**, 1026-1036 (2007).
[2] J. Brillo and G. Lohöfer, F. Schmidt-Hohagen, S. Schneider and I. Egry, Int. J. Mat. and Prod. Techn. **26**, 247-273 (2006).
[3] Y. Plevachuk et at., Int. J. Mat. Res. **98**, 107-111 (2007).
[4] J. Brillo, I. Egry and J. Westphal, Int. J. Mat. Res. **99**, 162-167 (2008).
[5] H.L. Peng, Th. Voigtmann,G. Kolland and J. Brillo (In preparation).

Structural aspects of glass-formation in Ni-Nb melts

D. Holland-Moritz,[1], * F. Yang,[1] J. Gegner,[1] T. Hansen,[2] and M.D. Ruiz-Martín[3]

[1] *Institut für Materialphysik im Weltraum, Deutsches Zentrum für Luft- und Raumfahrt (DLR), 51170 Köln, Germany*
[2] *Institut Laue-Langevin (ILL), 38042 Grenoble, France*
[3] *Departament de Física i Enginyeria Nuclear, Universitat Politècnica de Catalunya, Barcelona, Spain*

Metallic glasses have attracted considerable attention in both scientific and technological fields. While in preceding investigations the short-range order of melts of binary Zr-based glass-forming alloy systems such as Zr-Cu [1], Zr-Ni [2] or Zr-Pd [3] has been studied, here we present neutron scattering studies on the short-range order of glass-forming Ni-Nb alloy melts, for which the Zr-component is replaced by its neighbor in the periodic table of the elements, Nb.

In order to avoid possible reactions of the melts with crucible materials and in order to reduce background scattering at materials in the vicinity of the sample, the liquids are containerlessly processed under high vacuum (pressure $< 10^{-6}$ mbar) by employing a compact electrostatic levitator specially developed for performing scattering experiments [4]. The neutron scattering experiments were performed on the diffractometer D20 at the Institut Laue-Langevin (ILL) using a wavelength of the incident neutrons of $\lambda = 0.94$ Å. Total structure factors, $S(Q)$, of three $\mathrm{Ni}_{59.5}\mathrm{Nb}_{40.5}$ melts prepared with natural Ni, ^{58}Ni, and ^{60}Ni were measured [5]. Partial static structure factors were been calculated from the three total structure factors within the Faber-Ziman and the Bhatia-Thornton formalism.

The static Faber-Ziman structure factors $S_{NbNb}(Q)$, $S_{NiNb}(Q)$, and $S_{NiNi}(Q)$ describe the contributions to $S(Q)$, which result from the three different types of atomic pairs (Nb-Nb, Ni-Nb and Ni-Ni). Within the Bhatia-Thornton formalism the static partial structure factor $S_{NN}(Q)$ describes solely the topological SRO of the system, $S_{CC}(Q)$ the chemical SRO, and $S_{NC}(Q)$ the correlation of number density and chemical composition. Fig.1 shows the Faber-Ziman structure factors for liquid $\mathrm{Ni}_{59.5}\mathrm{Nb}_{40.5}$ at $T = 1495\,K$.

From the partial structure factors partial pair correlation functions have been calculated by Fourier transformation. These provide information on the nearest neighbor distances and on the partial coordination numbers. The nearest neighbor coordination number $Z_{NN} = 14.3$ determined for liquid $\mathrm{Ni}_{59.5}\mathrm{Nb}_{40.5}$ is considerably higher than the typical values of $Z_{NN} = 12$ reported for melts of metallic elements [6]. From the partial coordinationnumbers $Z_{NbNb} = 6.4$, $Z_{NiNb} = 9.6$ and $Z_{NiNi} = 6.8$ the average coordination numbers of the different types of atoms, Ni and Nb, can be calculated. While the smaller Ni atoms are characterized by a nearest neighbor coordination number of $Z_{Ni} = Z_{NiNi} + Z_{NbNi} = 13.3$, the larger Nb atoms exhibit an even larger coordination number of $Z_{Nb} = Z_{NbNb} + Z_{NiNb} = 16.0$. This directly implies that not only the chemical but also the topological short-range order around the Ni atoms differs from that around the Nb atoms.

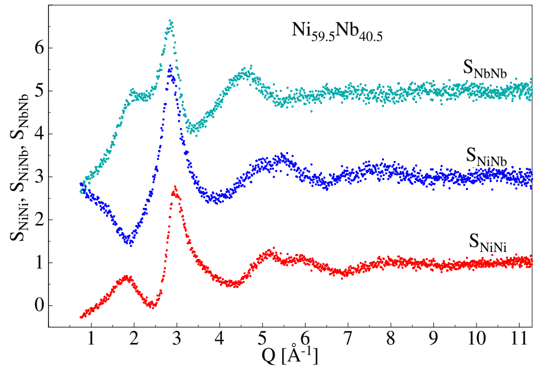

FIG. 1: Partial Faber-Ziman structure factors of liquid $\mathrm{Ni}_{59.5}\mathrm{Nb}_{40.5}$ at $T = 1495$ K [5].

Similar as $\mathrm{Ni}_{59.5}\mathrm{Nb}_{40.5}$, liquid $\mathrm{Ni}_{36}\mathrm{Zr}_{64}$ is characterized by a large nearest neighbor coordination number of $Z_{NN} = 13.9$ [2]. The same holds for other Zr-based binary glass-forming melts like $\mathrm{Zr}_2\mathrm{Cu}$, $\mathrm{Zr}_{50}\mathrm{Cu}_{50}$, $\mathrm{Zr}_7\mathrm{Cu}_{10}$ or $\mathrm{Zr}_2\mathrm{Pd}$ for which large coordination numbers in the range of $13.6 \leq Z_{NN} \leq 13.8$ are reported [1, 3]. These large coordination numbers indicate a large local density of packing that may give rise to large activation energies for atomic diffusion, hence facilitating glass-formation. When calculating the coordination numbers of the Ni and Zr atoms in liquid $\mathrm{Ni}_{36}\mathrm{Zr}_{64}$ from the partial coordination numbers one again finds that for the larger species of atoms, Zr, the coordination number is significantly higher with $Z_{Zr} = 15.4$ as compared to that of the Ni atoms $Z_{Ni} = 11.3$.

The different coordination numbers found for $\mathrm{Ni}_{59.5}\mathrm{Nb}_{40.5}$ and $\mathrm{Ni}_{36}\mathrm{Zr}_{64}$ melts for the smaller and the larger atoms show that such liquids cannot be characterized by one single type of short-range order. Indeed molecular dynamics simulations for Zr-based binary glass-forming liquids [7, 8] suggest a large variety of different types of aggregates prevailing in such liquids. The structural frustration associated with different types of short-range structures may hinder crystallization of the melt and thus favor glass-formation.

* Corresponding author: `dirk.holland-moritz@dlr.de`

[1] D. Holland-Moritz et al., EPL **100**, 56002 (2012).
[2] D. Holland-Moritz et al., Phys. Rev. B **79**, 064204 (2009).
[3] S. Klein et al., EPL **102**, 36001 (2013).
[4] T. Kordel et al., Phys. Rev. B **83**, 104205 (2011).
[5] D. Holland-Moritz et al., JAP **115**, 203509 (2014).
[6] T. Schenk et al., Phys. Rev. Lett. **89**, 075507 (2002)
[7] L. Huang et al., Phys. Rev. B **83**, 184103 (2011).
[8] S.G. Hao et al., JAP **107**, 053511 (2010).

Possible biological effectiveness of water adsorbed on surfaces pretreated with water

Dietmar Neuhaus*

Institut für Materialphysik im Weltraum, Deutsches Zentrum für Luft- und Raumfahrt (DLR), 51170 Köln, Germany

It was recently reported that the adsorption rate and the amount of adsorbed water on surfaces can be increased by previous cycles of adsorption and desorption of water on this surfaces [1]. Such a pretreatment of a surface creates a small amount of special arranged water molecules on the surface, which are probably responsible for the observed effect. This was the interpretation of infrared spectra of water molecules on surfaces measured with an ATR Fourier infrared spectrometer (ATR: attenuated total reflection) during the adsorption and desorption of water. The radiation absorption by the O-H stretching vibration band of water molecules around $3300\,cm^{-1}$ was the basis for the interpretation, because the absorption of radiation in this wavenumber range is sensitive for the arrangement of water molecules. In addition it was observed, that with an increasing amount of adsorbed water molecules, measured by the integrated absorbance in the wavenumber range $3000\,cm^{-1}$ to $3600\,cm^{-1}$, the wavenumber, where the maximum in the O-H stretching vibration band is observed, is strongly shifted to smaller wave numbers, which is interpreted as an increase of the degree of order of the water molecules inside the adsorbed water layer (figure 1). The observed effect caused by the pretreatment of surfaces can be used to moisten surfaces efficiently from the gas phase [2], with the special application to moisten plants [3] in greenhouses.

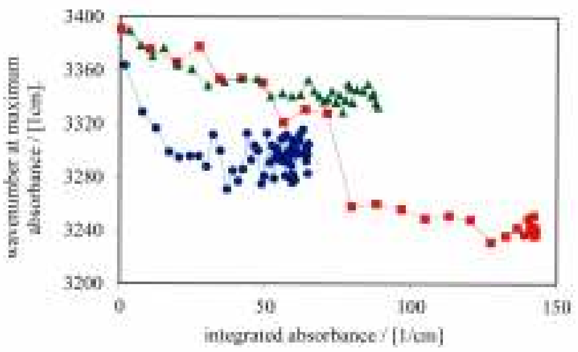

FIG. 1: Wavenumber at the maximum of the absorbance in the wavenumber range of the O-H stretching vibration as function of the integrated absorbance (wavenumber range: $3000\,cm^{-1}$ to $3600\,cm^{-1}$), for the samples diamond (blue dots), titanium dioxide powder on diamond (red squares) and quartz flour on diamond (green triangles).

There is now an indication that water, adsorbed after the mentioned pretreatment, may be biologically active. Colleques from the university of Bonn and a company have developed a so called " activated water" for plant protection applications. This water is a special treated pure water. Details of the treatment are confidential. Samples of "activated water" and pure water, both delivered by the company, and a sample of ultrapure water (Merck) were analyzed with ATR infrared spectroscopy. The results are shown in figure 2. Differences between the spectra of the three samples are very small, but it was possible to distinguish between the "activated water" infrared spectrum and the two spectra of the pure water samples (pure and ultrapure). Compared to the pure water spectra the ATR spectra of "activated water" shows a clear decrease of the absorbance in the lower frequency part of the O-H stretching vibration band. The decrease was not sufficient to shift the maximum of the O-H vibration band noticeably, but the tendency of a shift of the maximum to higher wave numbers is obvious. The decrease can be interpreted as a slight increase of the disorder in the "activated water" if compared with the pure water samples [1].

A big shift of the wavenumber at the maximum of absorbance as function of the amount of adsorbed water, which indicate a change of the degree of order inside the adsorbed water layer, is observed, when surfaces were pretreated by adsorption and desorption cycles, as shown in figure 1. If the degree of order in the water is important for its biological activity, then adsorbed water on a surface, pretreated by adsorption desorption cycles of water, is a good candidate for a biological active water layer. In case of the surface of a leave of a plant, this could enable plant protection with water.

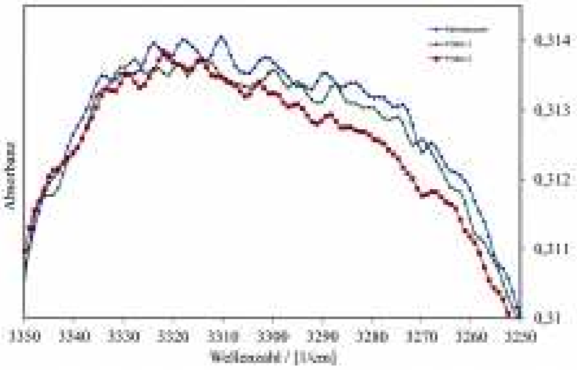

FIG. 2: ATR infrared spectra of ultrapure water (blue line), pure water (green line) and "activated water" (red line) in the wavenumber range of the O-H stretching vibration band of water. The infrared spectrum of the activated water sample can be distinguished from the pure water spectra due to a decrease of the absorbance in the low wavenumber range of the absorption band.

* author: `Dietmar.Neuhaus@dlr.de`

[1] D. Neuhaus, Adsorption, 19, (2013), p. 1127-1135
[2] D. Neuhaus, Patent DE 10 2010 026 591.8
[3] D. Neuhaus, Patent DE 10 2012 220 111.4

Surface tension of liquid Al and Si

H. Kobatake,* P. Pichon, and J. Brillo

Institut für Materialphysik im Weltraum, Deutsches Zentrum für Luft- und Raumfahrt (DLR), 51170 Köln, Germany

Due to their low densities, Al-based alloys are widely used as lightweight materials in automotive and aeronautical industry. The surface tensions of the liquid metals are important factors for controlling mass transport in a fluid during casting or welding processes. Although, up to now, several studies on the surface tension of liquid Si and Al have been reported, the values of surface tensions have discrepancies depending on each researcher [1, 2]. In the present study, surface tensions of liquid Al and Si were measured using oscillating drop method [3] in combination with an electromagnetic levitator (EML). The chamber was evacuated using a turbo molecular pump coupling with a rotary pump down to the order of 10^{-4} Pa and then filled with Ar or He gas with the purity of 99.9999%. The oxygen partial pressure in the EML chamber was lower than 10^{-1} Pa.

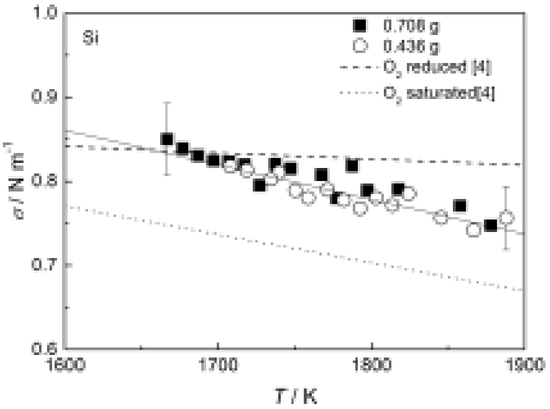

FIG. 1: Surface tension of liquid Si as a function of temperature. The solid line indicates a linear fit to all experimental results. The dashed and dots lines indicate the surface tension of liquid Si with oxygen reduced and oxygen saturated surface, respectively.

Figure 1 shows surface tension of pure Si as a function of temperature. The surface tensions of liquid Si with different masses are consistent with each other within the experimental uncertainty of 5% showing the experimental validity. The dashed and dots lines indicate the the surface tensions of liquid Si in literature [4] with the oxygen reduced and oxygen saturated surfaces, respectively. The surface tension of liquid Si shows a good agreement with the data from the oxygen reduced surface obtained in the oxygen partial pressure of 10^{-20} Pa [4].

Figure 2 shows the temperature dependence of surface tension of pure Al with the data in literature obtained from oxygen reduced (dashed) and oxygen saturated (dots) surface [5]. Similar to the case of liquid Si, our data show a good agreement with the data obtained under oxygen reduced surface. Although the oxygen partial pressure in the chamber was higher than the equilibrium oxygen partial pressure to form Al_2O_3 or SiO_2 on the liquid surface, both surface tensions of pure Al and Si indicate that the surface of the liquid Al and Si are maintained as oxygen reduced surface. Further, no oxide was found on the liquid Si and Al surfaces during the surface tension measurements.

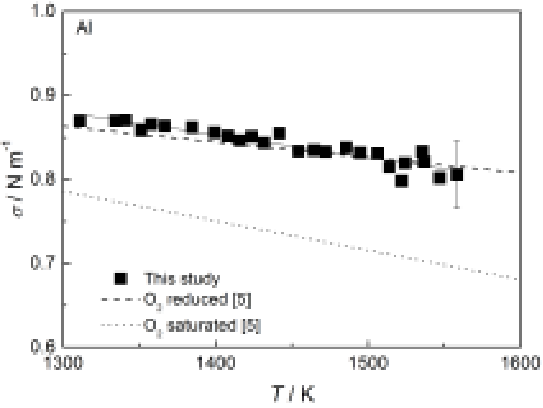

FIG. 2: Surface tension of liquid Al as a function of temperature. The solid line indicates a linear fit to all experimental results. The dashed and dots lines indicate the surface tension of liquid Al with oxygen reduced and oxygen saturated surface, respectively.

This inconsistency could be explained by taking into account of the difference of the oxygen partial pressure between the background of chamber and at the vicinity of surface. The oxygen partial pressure on surface can be reduced due to the evaporation of the oxide [1]. In the case of the Al and Si, the oxygen at surface was removed as Al_2O and SiO, respectively. Thermodynamic calculation considering the evaporation kinetics indicate that the oxygen partial pressure at the vicinity of the liquid Al and Si surface could be reduced to 10^{-24} Pa and 10^{-26} Pa, respectively. These oxygen partial pressures are low enough to maintain the oxygen reduced surface of the liquid samples.

Within the framework of the bundled project PAK 461, this study was financially supported by the Deutsche Forschungsgemeinschaft DFG, grant BR 3665/3-2.

---

* Corresponding author: `hidekazu.kobatake@dlr.de`

[1] N. Eustathopoulos and B Drevet, J. Crys. Growth **371**, 77 (2013).

[2] BJ. Keene, Int. Mat. Rev. **38**, 157 (1993).

[3] J. Brillo, G. Lohöfer, HF. Schmidt, S. Schneider, I. Egry, Int. Mat. Prod. Tech **26**, 247 (2006).

[4] K. Mukai, Z. Yuan, K. Nogi, T. Hibiya, ISIJ. International **40**, S148 (2000).

[5] J M. Molina, R. Voytovych, E. Louis, N. Eustathopoulos, Int. J. Adh. Adhesives **27**, 394 (2007).

Surface tension of liquid Al-Si alloys

H. Kobatake,* P. Pichon, J. Schmitz, and J. Brillo
Institut für Materialphysik im Weltraum, Deutsches Zentrum für Luft- und Raumfahrt (DLR), 51170 Köln, Germany

Due to their low densities, Al-based alloys are widely used as lightweight materials in automotive and aeronautical industry. The surface tensions of the liquid alloys are important factors for controlling mass transport phenomena in a fluid during casting or welding processes. In this study report on measurement of the surface tension of liquid Al, Si, and Al-Si alloys at selected chemical compositions.

According to Butler [1], the surface tension of binary liquid alloy, σ, can be expressed from the surface tensions of the pure components as follows:

$$\sigma = \sigma_{Al} + \frac{RT}{S_{Al}} ln(\frac{a^B_{Al}}{a^S_{Al}}) = \sigma_{Si} + \frac{RT}{S_{Si}} ln(\frac{a^B_{Si}}{a^S_{Si}}) \qquad (1)$$

Here R is the gas constant, T is absolute temperature, S indicates the surface area, and a the activity. The subscripts Al and Si denote the components in the alloy. The superscripts B and S indicate the bulk and surface phase, respectively. By solving the above system of equations, we can calculate the compositional dependence of the surface tension of liquid alloys.

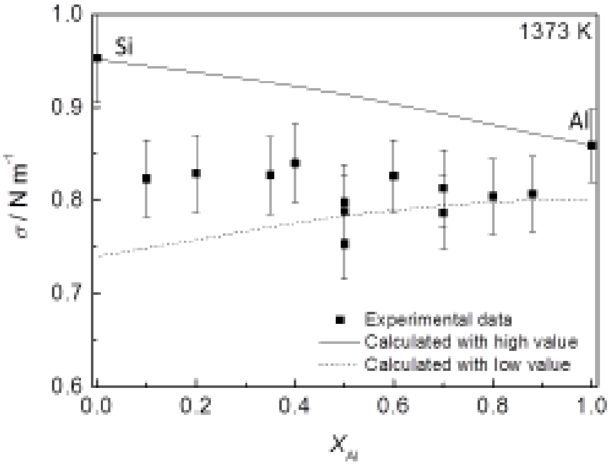

FIG. 1: Surface tension of liquid Al-Si binary alloys at 1375 K with calculated values from the surface tensions of the pure components, Al and Si, using the values of the oxygen reduced (solid) and the oxygen saturated (dashed) surfaces.

Figure 1 shows the compositional dependence of the surface tensions of pure liquid Al, Si and liquid Al-Si alloys measured in this study. The solid and dashed lines indicate the calculated values based on the Butler model using the surface tensions of the oxygen reduced and oxygen saturated surfaces [2] [3], respectively. Surface tensions of liquid Al-Si alloys show a good agreement with the calculated values assuming that the surface is saturated with oxygen at Al (X_{Al} >0.6),rich concentrations. However, at $X_{\mathrm{Al}} \leq 0.5$, surface tension of the liquid alloys approach the surface tension of the oxygen reduced surface, upon decreasing the Al concentration.

The effect of oxygen on the surface tension can be interpreted considering metastable phase formation at the surface. Figure 2 shows the oxygen partial pressure-composition phase diagram for the binary Al-Si system at 1400 K. The dotted line in the figure shows the region, in which the metastable Mullite ($Al_6Si_2O_{13}$) can exist. while the dashed line indicates the compositional dependence of the oxygen partial pressure on the surface controlled by SiO evaporation.

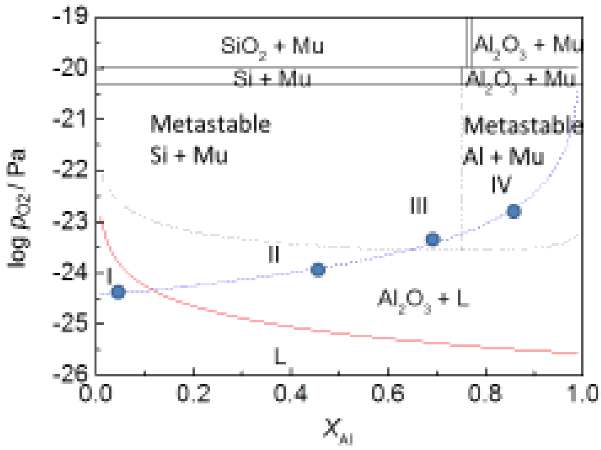

FIG. 2: Binary surface P_{O2}-composition diagram in Al-Si system.

The surface is separated to 4 conditions depending on composition: (I) $X_{Al} \leq 0.1$: the liquid is free from the oxide formation, (II) $0.1 < X_{Al} \leq 0.6$: the liquid is equilibrated with Al_2O_3 on surface, (III) $0.6 < X_{Al} < 0.75$: Si starts to absorb the oxygen with forming metastable Mullite, and (IV) $X_{Al} > 0.75$: the surface of the liquid was completely covered with oxygen as Al_2O_3 and Mullite. This surface phase relation consistent with the compositional dependence of the surface tension of liquid Al-Si alloys observed in this study. This surface transition could control the oxygen adsorption on liquid Al-Si surface.

Within the framework of the bundled project PAK 461, this study was financially supported by the Deutsche Forschungsgemeinschaft DFG under grand number BR 3665/3-2.

---

[*] Corresponding author: `hidekazu.kobatake@dlr.de`

[1] J A V. MButler, Proc. R. Sco. London **135**, 348 (1932).
[2] J M. Molina, R. Voytovych, E. Louis, N. Eustathopoulos, Int. J. Adh. Adhesives **27**, 394 (2007).
[3] N. Eustathopoulos and B Drevet, J. Crys. Growth **371**, 77 (2018).

1.3 Solidification, Nucleation and Growth

Microstructure formation in an undercooled melt of NiZr

R. Kobold,* W. Hornfeck, M. Kolbe, and D.M. Herlach
Institut für Materialphysik im Weltraum, Deutsches Zentrum für Luft- und Raumfahrt (DLR), 51170 Köln, Germany

Metallic melts in general can be essentially undercooled below their liquidus temperatures T_L given that heterogeneous crystal nucleation on container walls is avoided. In our present work we apply containerless electrostatic levitation [1], which is an established method to undercool metallic melts and to avoid heterogeneous nucleation. The experiments are conducted in ultra high vacuum conditions, which is beneficial in terms of the purity of the specimen. In an ESL-processed liquid sample convection can be neglected and therefore leads to a mostly undisturbed microstructure formation during crystallization.

Samples of the intermetallic, congruently melting system $Ni_{50}Zr_{50}$ are levitated and melted with an infrared laser, while the solidification process is observed with a high speed camera. The microstructures of as-solidified samples were analyzed by using optical polarization and scanning electron microscopy (SEM), including energy dispersive X-ray spectrometry (EDS) for chemical analysis and electron backscatter diffraction (EBSD) for texture analysis.

Only for high undercoolings $(280\,K - 300\,K)$ the microstructure of $Ni_{50}Zr_{50}$ shows the presence of 10 major grains separated by coherent boundaries traversing the sample with an angular inclination of about 36 degrees (Fig. 1). This correlates with high speed camera observations of the solidification process, where a 10-fold front propagates over the samples surface.

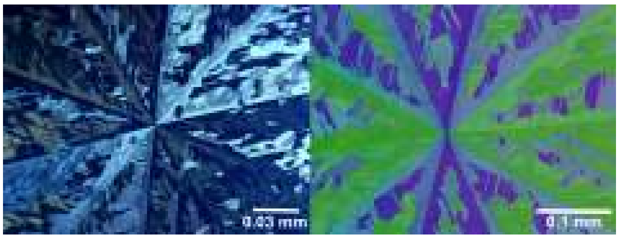

FIG. 1: Tenfold twinned dendritic microstructure apparent in the cross-sections of high undercooled NiZr samples. Left: optical polarization micrograph of an embedded sample (6 mm in diameter); Right: false-colour EBSD-map

In 1985, Kuo $et\,al.$ conducted high resolution transmission electron microscope experiments on rapidly quenched NiZr samples[2], finding a similar structure at a nm scale, but lacking any detailed explanation for its emergence.

Further EBSD measurements on as-solidified NiZr samples lead us to the conclusion that the observed structure in Fig. 1 was spanned by cooperative dendrite growth, where as the grain boundaries form the stem of the dendrites (twinned dendrites).

With the information gained from the crystal growth (crystal orientations, angles, planes, growth directions) via EBSD measurements, we are able to reconstruct the center of solidification at an atomic scale. This is achieved through an idealization of the NiZr unit cell i.e. the adaptation of the interatomic distances in order to build a tenfold structure of atoms with the observed microstructure taken into consideration. As a result, we obtain a distortion-free, energetically advantageous twinning structure which explains the dominant occurrence of twin boundaries up to macroscopic scales. In addition, the twin model exhibits a "quasicrystalline"-like core and icosahedral short-range order. The latter will be further investigated with neutron scattering experiments. In order to proof the proposed twin model TEM measurements will be performed.

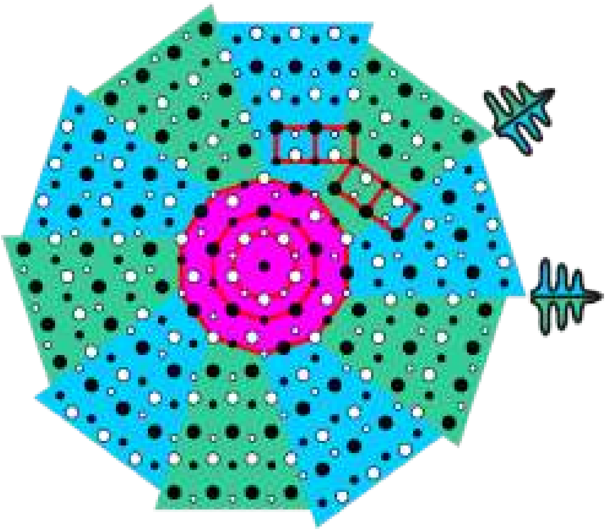

FIG. 2: Ideal tenfold twin. Ni-atom: white; Zr-atom: black; small/large dots denote different heights.

For high undercoolings only, ESL processed NiZr forms a tenfold twinned microstructure. We propose an atomistic model build by general geometric deliberations, which, in a most comprehensive view, bridges the scales from a homogeneously nucleated quasicrystalline–like seed via twinned dendrite growth to a macroscopic solid. In conclusion, a first real concept for the formation of a nucleus under non-equilibrium conditions is gained.

Financial support by Deutsche Forschungsgemeinschaft within contract HE1601/18 is gratefully acknowledged.

* Corresponding author: `raphael.kobold@dlr.de`

[1] T. Kordel, D. Holland-Moritz, F. Yang, J. Peters, T. Unruh, T. Hansen, A. Meyer, Phys. Rev. **B 83**, 104205 (2011).
[2] W. J. Jiang, Z. K. Hei, Y. X. Guo and K.H. Kuo, Phil. Mag. **A 52**, L53 (1985).

Thermal performance tests of a modified isothermal furnace for in-situ X-ray solidification experiments

Maike Becker,* Stefan Klein, and Florian Kargl

Institut für Materialphysik im Weltraum, Deutsches Zentrum für Luft- und Raumfahrt (DLR), 51170 Köln, Germany

For the in-situ observation of solidification processes, we use a compact laboratory facility [1] that consists of a micro-focus x-ray tube, an isothermal furnace, and a detector system. The previously-described [2] near-isothermal furnace, was modified to introduce a better thermal symmetry to the temperature profile of the sample. The formerly used molybdenum heating wire was replaced by a meander-shaped graphite heater. This new heater arrangement provides a uniform heat transport towards the sample. As dendrite growth is very sensitive to thermal changes, a symmetric and well-defined temperature field in the sample is essential [3, 4].

To validate the homogeneity of the temperature field in the sample, Al-Cu samples of near-eutectic compositions were processed. The 200 μm thin samples of 12 mm diameter were processed in horizontal alignment to suppress fluid-flow. The compositions deviated slightly to the hypo-eutectic side resulting in nucleation of primary fcc-Al dendrites followed quickly by the eutectic. At the eutectic point the liquid solidifies in a two-phased microstructure at a well-defined (eutectic) temperature. In Al-Cu this reaction (L$\rightarrow \alpha + \theta$), with α being the Al and θ being the intermetallic Al_2Cu phase, is visible in the radiographs because of the change in density between the liquid and the solid phase. The eutectic solidification starts when the temperature falls below the eutectic temperature. Hence, the temperature distribution in the sample can be deduced from the solidification starting point. Assuming a homogenous composition throughout the sample, the propagation of the eutectic front together with the cooling rate can provide information on the maximal temperature gradient across the field of view.

We performed multiple solidification experiments with cooling rates of 1 and 2 K min^{-1} to estimate the temperature gradient imposed onto the sample by the furnace. The experiments showed that eutectic solidification starts at different places, even in the same repeatedly processed samples. The random starting point indicates already a rather uniform temperature field within the sample. A sequence of radiographs is shown in figure 1. Derived from the propagation of the eutectic front (dark area image 4 to 6), maximal temperature gradients for cooling rates of 1 and 2 K min^{-1} are 0.11 K mm^{-1} and 0.23 K mm^{-1}, respectively. These values represent maximum temperature gradients, as we assume that the sample temperature does not immediately adapt to the measured temperature; or in other words, the sample temperature may not exactly follow the applied cooling rate. For the same reason, calculated temperature gradients may be higher for increased cooling rates.

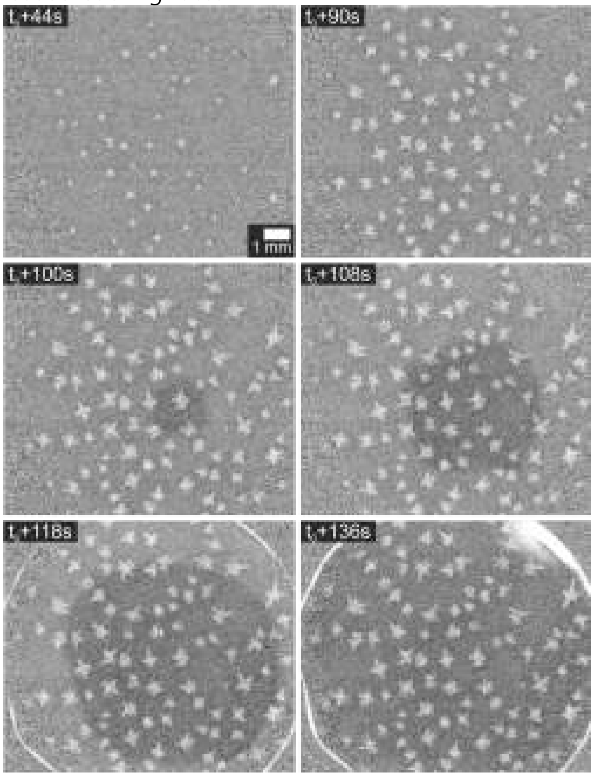

FIG. 1: Sequence of six X-ray radiographs showing the time evolution of an Al-33wt.%Cu alloy solidifying in nearly isothermal conditions. The cooling rate is 2 K min^{-1}. Already the initial Al-dendrite nucleation (light spots), which is homogeneous throughout the sample, indicates a negligible temperature gradient. Eutectic solidification starts near the center of the sample. The maximum temperature gradient across the field of view can be calculated by considering distance, time and temperature of the eutectic front.

The temperature gradients analyzed in this study are ideal for in-situ x-ray radiography measurements of equiaxed dendritic solidification. This can already be deduced from the fcc-Al dendrites growing nicely equaxially (cf. figure 1). Therefore the isothermal furnace is optimally suited for its purpose and will be operated aboard the sounding rocket MAPHEUS-5 to carry out solidification experiments under microgravity conditions free of buoyancy-driven convective flow.

[*] Corresponding author: `maike.becker@dlr.de`

[1] A. Knipstein, Bachelor Thesis (2012).
[2] P. Barmsen, Bachelor Thesis (2013).
[3] A. Murphy, PhD Thesis, University College Dublin (2013).
[4] M. Becker, S. Klein, F.Kargl, DLR-MP Annual Report (2013).

How to compare experimental and simulated microstructures of eutectic Al-Ag-Cu

A. Dennstedt,[1],* L. Ratke,[2] A.Choudhury,[3] and B. Nestler[4]

[1] *Institut für Materialphysik im Weltraum, Deutsches Zentrum für Luft- und Raumfahrt (DLR), 51170 Köln, Germany*
[2] *Institut für Werkstoffforschung, Deutsches Zentrum für Luft- und Raumfahrt (DLR), 51170 Köln, Germany*
[3] *Indian Institute of Science, Department of Materials Engineering, 560012 Bangalore, India*
[4] *Institut für Angewandte Materialien, Karlsruhe Institut für Technologie, 76131 Karlsruhe, Germany*

During solidification of a ternary eutectic melt three solid phases appear at the same time while no melt will be left. Because of these three solid phases providing more possibilities of arrangement the resulting patterns are much more complex compared to binary eutectics [1].

In our paper [2] we have investigated microstructural patterns in both experimental and simulated solidification in order to develop necessary characterization tools for the comparison of the patterns. Al-Ag-Cu alloys of near eutectic composition were directionally solidified with velocities of 0.08 to 3.8 μm/s and gradients of 1.5 to 6.2 K/mm. Phase field simulations were performed with liquidus and solidus slopes as derived from the thermodynamic database. However, the phase fractions were adopted to the experimental observations to understand what parameters and conditions give rise to similar microstructures in experiment and simulations. Cross sections of both experimental and simulated microstructure were analyzed using the same source code written in Octave to determine interface lengths, triple points and number of neighbors.

Six different microstructures were experimentally distinguished (cf. fig.1). Parameters like the number of particles per image area and the particle size showed the expected growth velocity dependence. As a parameter independent on solidification velocity the number of neighbors showed clear differences in the distribution of intermetallic neighbors around the intermetallic particles (fig.2): the more ordered the microstructure appeared the higher is the fraction of intermetallic particles showing two neighbors of the other intermetallic phase. However, the neighborhood around the aluminum particles has to be considered, too. In contrast to the irregular structure the misaligned structure shows Al particles with many intermetallic neighbors whereas the neighbor distribution around the intermetallic particles is similar in both microstructures.

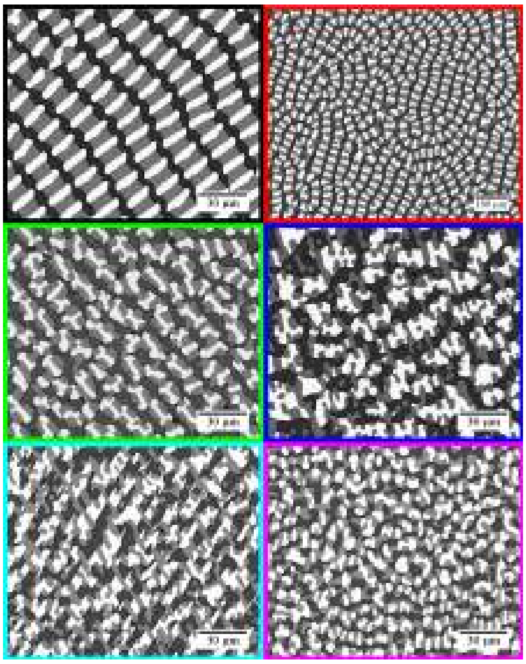

FIG. 1: Different microstructures in Al-Ag-Cu ternary eutectic: ladder structure, cobblestone structure, misaligned structure, paw structure, crossed structure, and irregular structure (white = Ag_2Al, gray = Al_2Cu, black = Al).

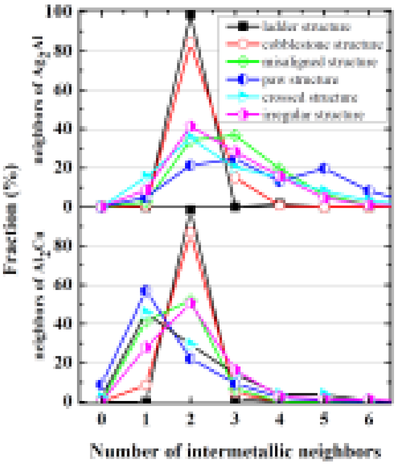

FIG. 2: Neighbor relationships of intermetallic particles in the different microstructures.

Analysis of tiled simulated images resulted in increasing fraction of intermetallic particles with 2 intermetallic neighbors. This shows the increasing order during the various stages of the early stage of solidification until a uniform microstructure is achieved. Due to the comparison between simulations and experiments we were able to identify that the asymmetry in the Gibbs-Thomson coefficients and the volume fractions are two key parameters influencing the pattern formation in multi-phase solidification.

This work was supported by DFG (RA537/14-2 and NE822/14-2).

* Corresponding author: `anne.dennstedt@dlr.de`

[1] D. Lewis, S. Allen, M. Notis and A. Scotch, J. Electron. Mater. **31**, 161 (2002).
[2] A. Dennstedt, A. Choudhury, L. Ratke and B. Nesler, submitted to IOP Conf. Series - Materials Science and Engineering (2014).

Bent Dendrite Growth in Undercooled Fe-B Alloy Melts

C. Karrasch,[1,2,*] T. Volkmann,[1] J. Valloton,[1,3] M. Kolbe,[1] and D. M. Herlach[1,2]

[1]*Institut für Materialphysik im Weltraum, Deutsches Zentrum für Luft- und Raumfahrt (DLR), 51170 Köln, Germany*
[2]*Institut für Experimentalphysik IV, Ruhr-Universität Bochum, 44780 Bochum, Germany*
[3]*Advanced Materials and Processing Laboratory, University of Alberta, Edmonton, Canada*

Dendritic growth is the main solidification mode in alloy casting. In order to control dendrite growth for materials design from the melt it is important to understand the influence of process conditions.

This study [1] stands as an experimental note observing bent dendrite growth in Fe-B alloys and suggesting possible explanations as induced by fluid flow [2], thermal, and concentrational diffusion or impurities [3]. Electromagnetic levitation technique (EML) is used for containerless processing of undercooled melts under terrestrial ($1g$) [4] and reduced gravity (μg) conditions in parabolic flight using the TEMPUS [5] facility.

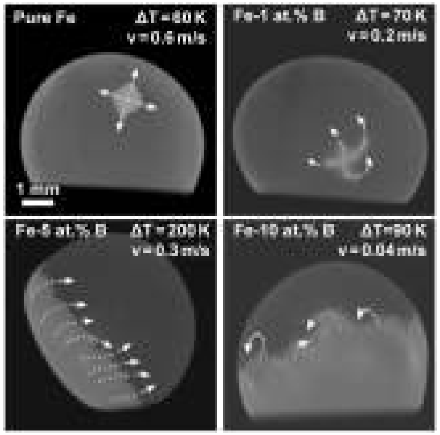

FIG. 1: High-speed video images of electromagnetic levitated samples. The dark grey area is the undercooled liquid. The light grey region corresponds to the growing solid, which appears brighter due to the release of latent heat during rapid solidification. Arrows indicate the directions and trajectories of the growing dendrites showing straight (pure Fe), spiral like (Fe-1 at.% B), zigzagging (Fe-5 at.% B), and U-turn (Fe-10 at.% B) patterns in 1g-EML.

Fig. 1 shows typical results for the trajectories of the growing dendrites. The highest undercoolings ΔT where bent dendrite growth has been observed so far are given in Table I. Mainly the dendrite growth velocities are in the order of 10^{-1} m/s, therefore in the same order of magnitude as the fluid flow velocities in $1g-$EML (0.3 m/s) according to R.W. Hyers [6]. In $\mu g-$EML the fluid flow is about 0.05 m/s, one order of magnitude lower than in $1g-$EML but still in the order of the slowest observed growth velocities. Fig. 2 shows a bent growing dendrite under microgravity conditions. The cause of the observed bent dendrite growth is unclear. Impurities cannot be neglected and should be considered as a possible explanation to the growth behaviour. However, the primary cause seems to be the influence of fluid flow on the thermal and/or concentration gradients at the growing dendrite tip. Further investigations with defined fluid flow conditions are needed to give a final conclusion.

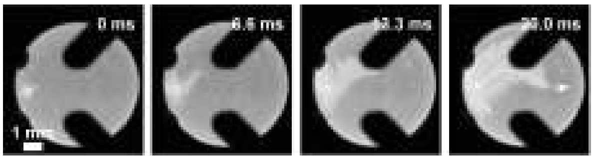

FIG. 2: Snapshots of a undercooled solidifying Fe-1 at.% B liquid sample (dark grey) in $\mu g-$EML during parabolic flight showing bent dendrite growth (light grey).

In future applications the effect of bent growing dendrites may be used to manipulate the microstructure development during solidification. For example, dendrites could be bent during growth to follow the curving of a turbine blade or guided growing dendrites of semiconductor on substrates could lead to new technologies.

TABLE I: Highest undercoolings ΔT and corresponding dendrite growth velocities v for Fe-1, 5 and 10 at.% B where bent dendrite growth has been observed so far. Data for pure Fe is added for comparison.

		ΔT (K)	v (m/s)	Observed pattern
$1g-$EML	Pure Fe	60	0.6	Straight
	Fe-1 at% B	70	0.2	Spiral growth
	Fe-5 at% B	200	0.3	Zigzagging
	Fe-10 at% B	110	0.05	U-turn
TEMPUS	Fe-1 at% B	100	0.14	Zigzagging

The authors are grateful to DLR Space Administration Bonn for the parabolic flight opportunity and to the TEMPUS-Crew performing the experiment. Special thanks are extended to G.J. Ehlen, J. Gegner, R. Kobold, S. Burggraf, and S. Klein for support and fruitful discussions. This research work was financially supported by the German Research Foundation DFG within contract HE1601/18, the European Space Agency ESA under contract numbers 4200020277 and 4200014980, and the Canadian Space Agency CSA FAST program.

[*] Corresponding author: `christian.karrasch@dlr.de`

[1] C. Karrasch, T. Volkmann, J. Valloton, M. Kolbe, D.M. Herlach, ICASP4, IOP Conf. Series: Materials Science and Engineering (under review)
[2] A. M. Mullis, Acta Materialia **47**, 1783-1789 (1999).
[3] L. Gránásy, T. Pusztai, J. A. Warren, J. F. Douglas, T. Börzsönyi and V. Ferreiro, Nature Materials **3**, 92-96 (February 2003).
[4] D.M. Herlach, Annu. Rev. Mater. Sci. **21**, 23-44 (1991)
[5] G. Lohöfer, J. Piller, Proceedings 40th AIAA, 2002-0764 (2002).
[6] R. W. Hyers, Meas. Sci. Technol. **16**, 394-401 (2005).

Undercooling and solidification of eutectic CoSi-$CoSi_2$ in low gravity and in ESL

M. Kolbe,[1] J.R. Gao,[2] C. Karrasch,[1,3] and S. Klein[1]

*[1] Institut für Materialphysik im Weltraum, Deutsches Zentrum für Luft- und Raumfahrt (DLR), 51170 Köln, Germany**
[2] Key Laboratory of Electromagnetic Processing of Materials (Ministry of Education), Northeastern University, Shenyang 110004, P.R. China
[3] Institut für Experimentalphysik IV, Ruhr-Universität Bochum, 44780 Bochum, Germany

Eutectic alloys are important industrial materials, thus, near-equilibrium solidification microstructures have been widely investigated. In binary eutectics, both of the involved phases solidify co-operatively, often leading to a lamellar composite microstructure. The important parameter for the mechanical proper-ties of the alloy is the width of the lamella, which depends on cooling rate and nucleation conditions.

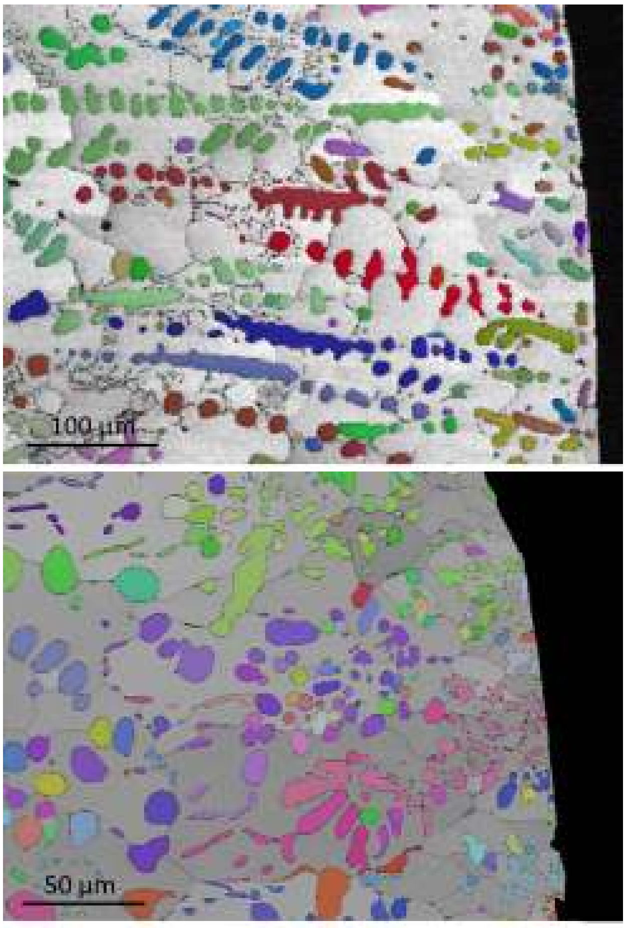

FIG. 1: Cross section of eutectic CoSi samples solidified in low gravity at medium undercooling. Colors of the CoSi phase refer to crystallographic orientations, determined by electron back scatter diffraction (EBSD). Top: The $CoSi_2$ phase (grey) shows a thin surface layer indicating primary solidification of $CoSi_2$. Bottom: For this sample CoSi and $CoSi_2$ started growing at the surface co-operatively.

In contrary, there is limited understanding of non-equilibrium solidification of eutectic alloys. An undercooled melt of eutectic composition has a strong driving force for solidification. The evolution of microstructure is influenced by nucleation and growth of the respective phases. Nuclei of the phases may have different probabilities to form due to different surface energies of the compounds. Furthermore a certain influence of melt flow on the resulting micro-structure has been reported [1]. In low gravity, melt convection is suppressed to a low level and therefore we extended our study of the CoSi-$CoSi_2$ eutectic [2] by the use of the TEMPUS facility on parabolic flights (Sept. 2013 / Oct. 2014). The plan of the experiments was to melt, undercool and solidify the eutectic alloy within the 20 s of low gravity. A high speed camera has been used to record the nucleation events of the two phases in order to determine the respective velocities of solidification. In previous experiments on ground we have found that at a critical undercooling temperature of 88 K there exists an abrupt change in velocity of solidification of the primary phase. At lower under-cooling the velocity of the primary phase is one order of magnitude higher than above the critical temperature. For the secondary phase holds the opposite. Microstructure analysis showed that at lower temperature CoSi is the primary phase and at higher temperature $CoSi_2$. The decision whether CoSi or $CoSi_2$ solidifies first is quite complicated when the sample is solidified with high convection in the melt. Dendrites might be broken or deflected from their initial growth direction. Fig. 1 gives typical microstructures of samples solidified with low convection. Fig. 1 (Top) shows long dendrites of the CoSi phase grown from the surface of the sample towards the center. Remarkable is a thin surface layer of $CoSi_2$ showing that this was the first phase to solidifiy. The concentration in the melt is consequently changed leading to an enhanced driving force for solidification of CoSi resulting in the growth of large CoSi dendrites. Once they are nucle-ated they grow faster than the $CoSi_2$ phase towards the center of the sample. Fig. 1 (Bottom) shows a case where both phases solidified co-operatively leading to a different microstructure. It should be emphasized that the combination of low convection conditions, observation of solidification by a high speed camera and EBSD microstructure analysis is a very powerful tool for unveiling mechanisms of non-equilibrium solidification.

Provision of the parabolic flight opportunity by DLR-Bonn is gratefully acknowledged.

* Corresponding author: `matthias.kolbe@dlr.de`

[1] M. Li, K. Nagashio, T. Ishikawa, A. Mizuno, M. Adachi, M. Watanabe, S. Yoda, K. Kuribayashi, Y. Katayama, Acta Materialia **56**, 2514-2525 (2008).
[2] Y.K. Zhang, J. Gao, M. Kolbe, S. Klein, C. Yang, H. Yasuda, D.M. Herlach, Ch.-A. Gandin, Acta Materialia **61**, 4861-4873 (2013).

Non-isothermal wetting experiments relevant to mold-product interface formation in the RGS (Ribbon Growth on Substrate) casting process

P.-Y. Pichon,[1, 2, *] D. Simons,[1] M. Kolbe,[1] D. Herlach,[1] and A. Schönecker[2]

[1] *Institut für Materialphysik im Weltraum, Deutsches Zentrum für Luft- und Raumfahrt (DLR), 51170 Köln, Germany*
[2] *RGS Development B.V., Bijlestaal 54 A 1721 PW, Broek op Langedijk, Netherlands*

The processes controlling the formation of the thermal-mechanical contact between a mold and a solidifying product are little understood despite the importance of controlling heat transfer and thermal stresses in metal casting. In the crystallization of net shape silicon wafers by the ribbon-growth-on-substrate (RGS) casting process, isothermal wetting models fail to describe the results: good wetting mold materials (Young wetting angle <90°) can still lead to a poor thermal-mechanical contact.This raises the question of the influence of solidification on wetting.

The interactions between spreading kinetics and solidification kinetics were studied using a new technique. Silicon droplets were melted in an electromagnetic levitation tool and released so as to impact, wet and solidifiy on polished silicon mold surfaces. The initial mold temperature was varied and a critical temperature of about 1000°C was identified. Substrate temperature below 1000°C lead to polycrystalline character of the deposited material, interfacial gaps and incomplete mold/deposited material interface relaxation (see Fig. 2). Above 1000°C the solidified material was grown epitaxially on the substrate, slip-stick occured, and the apparent angle was lower, reflecting the higher rates of solid-vapor to solid-liquid interface transformation (see Fig. 1).

The interfacial gaps and the slip-stick motion were interpreted at the consequence of solidification 'at' the contact line. The isothermal wetting models do not account for the interfacial force component acting at the contact line in the direction normal to the mold. This provides a driving force for growth of a solid silicon ridge and pinning (stick event) [1]. The kinetics of ridge growth was interpreted in term of a competition between solidification kinetics and spreading kinetics, both processes being thermaly activated. The solidification kinetics is limited by the transport and ordering of atomic species in the direction normal to the growth interface. Wetting is an interface transformation process limited by the transport kinetics in the direction parallel to the growth interface and requires disordering. Under conditions of sufficiently low mold temperature, this leads to significant undercooling at the contact line, resulting in nucleation in the bulk liquid and incomplete interface relaxation.

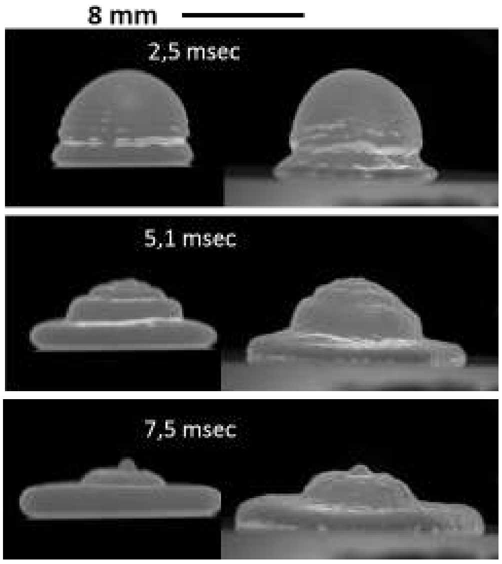

FIG. 1: Spreading behavior for liquid silicon deposited on polished, solid silicon substrate at room temperature (left) and 1140 °C (right). The time is measured from the impact. Note the difference in apparent angles at the contact line.

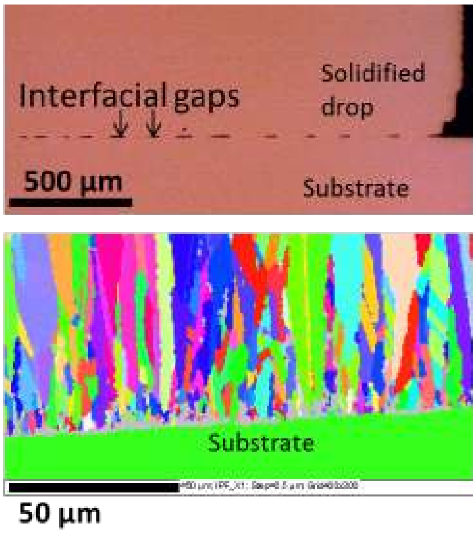

FIG. 2: Characterisation of the interface for silicon deposited on low temperature substrates. (top) Optical microscopy analysis of the substrate-deposited silicon interface, showing imperfect contact as evidenced by the presence of gaps. (bottom) EBSD (Electron BackScatter Diffraction) analysis of the interface, showing the polycrystalline character of the sample (different colours correspond to different crystalline orientations).

---

* Corresponding author: `Pierre-Yves.Pichon@dlr.de`

[1] E. Saiz, A Tomsia and R. Cannon, Acta. Mater. **46**, 2349-2361 (1998).
[2] T. Evans, *Mechanisms of interfacial heat transfer and nucleation of liquid steel in metallic substrates* (phD thesis, 1999).

High-Speed Infrared Observation of Solidification

M. Reinartz,[1,*] C. Karrasch,[1,2] T. Volkmann,[1] and D. M. Herlach[1,2]

[1] *Institut für Materialphysik im Weltraum, Deutsches Zentrum für Luft- und Raumfahrt (DLR), 51170 Köln, Germany*
[2] *Institut für Experimentalphysik IV, Ruhr-Universität Bochum, 44780 Bochum, Germany*

In levitation experiments the observation of the solidification process in undercooled melts is mostly done by using high-speed cameras (HSC) working in the spectrum of visible light. In the past, infrared cameras (IRC) were operating with to low framerates for observing solidification processes in metals. Recent developments make fast IRC available as a powerfull tool for new findings. Main focus lies on low melting materials which have no contrast in visible light. Furthermore the infrared spectrum contains information about the heat distribution in the melt and the solid as for example predicted by the LKT-Model [1].

Electromagnetic levitation (EML) is used for undercooling experiments [2]. This technique has the advantage of processing samples containerless and directly observe the solidification process. Positioning and heating of the sample are achieved by a high frequency alternating electromagnetic field. The transformation of the undercooled liquid phase into the solid phase leads to a visible contrast due to the release of latent heat during rapid solidification which can be recorded by a HSC. The temperature is measured contactless by an infrared-pyrometer.

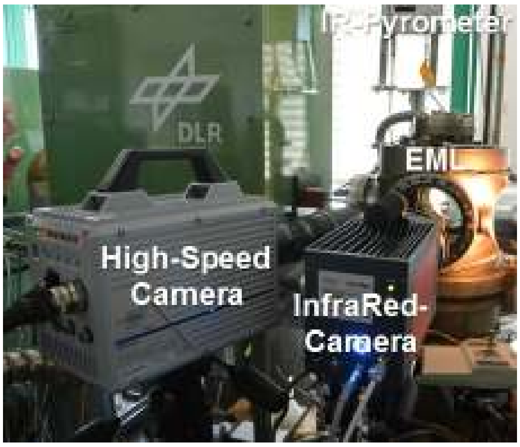

FIG. 1: Experimental setup to observe the solidification process simultaneously with a HSC and an IRC in front of an EML.

Fig. 1 shows the experimental setup. The IRC *ImageIR 8380, InfraTec Thermografiesystem* was placed directly in front of the recipient. This position was chosen to minimize the distortion of the infrared light by the window. The distortion of the visible light was not as strong as in the infrared domain thus the HSC *Photron FASTCAM SA5* was placed on the left. Observing infrared light through a glass window needs special filtering because glass absorbs the most part of the infrared spectrum. The IRC was operated with a filter called $25mm\ DGF(900-2500)°C\ 25\mu m$. Due to the working distance of *0.5 m* it was neccessary to adjust the image section to a smaller size. This leads to a lower resolution which could be improved by using a telephotolens. Therefore the maximum frame rate was *800 fps*. The HSC was operated with *1000 fps*. Thus the observation is not synchronised.

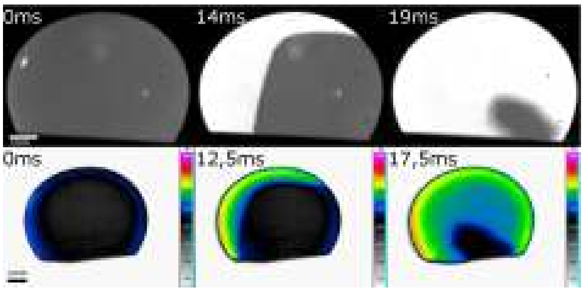

FIG. 2: Snapshots of a solidifying Fe_2B sample. Upper row: High-speed camera at *1000 fps*; Lower row: Infrared camera at *800 fps*.

Fig. 2 shows snapshots of a solidifying Fe_2B sample recorded by the HSC and IRC. In the upper row (HSC) the solid phase is light and the liquid phase is dark grey. By using the IRC it is possible to observe the propagating solidification front and temperature information (lower row). The emissivity ϵ of the solid and liquid phase differs and is unknown. The calculation of the temperature by the computer software is done according to the Stefan-Boltzmann-law. A calibration of the IRC was performed to the liquidus temperature of the sample material. However the spherical shape of the sample leads to a misinterpretation of the temperature. This results in a higher temperature gradient at the outer part of the spherical sample.

In conclusion this study demonstrated the possibility of observing solidification processes with an IRC. Low melting materials like AlCu cannot be investigated with common HSC in visible light but show remarkable contrast in the infrared. Furthermore detailed information about the heat distribution in the melt and during the solidification could be observed and is of great interest for future experiments. Nevertheless using IRC's is still limited to growth velocities up to $1m/s$ due to the maximum framerate of *850 fps*.

The authors want to thank Dr. Felix Göhring (Institute of Solar Research) for borrowing us the infrared camera and giving useful instructions.

---

[*] Corresponding author: `marcus.reinartz@dlr.de`

[1] J. Lipton, W. Kurz, R. Trivedi, Acta Mater **35**, 957 (1987)
[2] D.M. Herlach, Annu. Rev. Mater. Sci. **21**, 23-44 (1991)

Solidification of silicon-germanium alloys from the undercooled melt

D. Simons,[1,*] P.-Y. Pichon,[1,2] and D. Herlach[1]

[1]*Institut für Materialphysik im Weltraum, Deutsches Zentrum für Luft- und Raumfahrt (DLR), 51170 Köln, Germany*
[2]*RGS development B.V., Bijlestaal 54 A 1721 PW, Broek op Langedijk, Netherlands*

Samples with the following composition were undercooled and solidified: $Si_{75}Ge_{25}$, $Si_{50}Ge_{50}$ and $Si_{25}Ge_{75}$. We used a containerless electromagnetic levitation method with a graphite pre-heater to levitate the samples. The temperature of the sample was recorded by a infrared pyrometer. A high-speed camera with a maximum acquisition speed of 50.000 frames/s was used to record the morphology of the solid-liquid interface at the surface of the sample and to determine the growth velocity of the undercooled samples.

A maximum undercooling of 310 K, 305 K and 226 K was observed for $Si_{75}Ge_{25}$, $Si_{50}Ge_{50}$ and $Si_{25}Ge_{75}$, respectively. The measured velocities could be modeled with the LKT-Model [1]. FIG. 1 showes our results. The growth velocities of silicon-germanium alloys were compared with growth velocities of pure silicon and pure germanium measured in previous experiments.

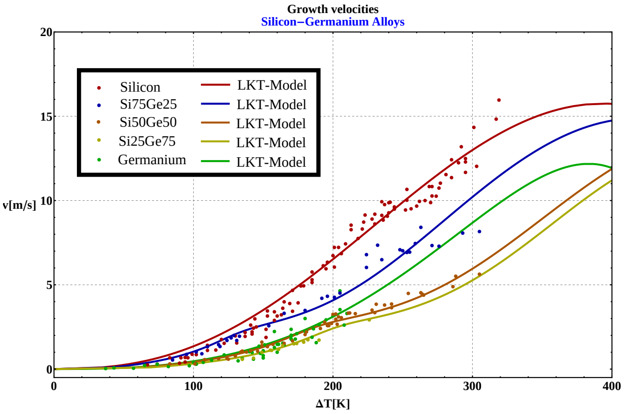

FIG. 1: Growth velocity v measured as a function of undercooling ΔT and modeled with LKT-Model.

The high speed video pictures also give information on the morphology of the growth front. As shown in FIG. 2, two changes of crystal growth morphology were identified. Plate-like crystals, isolated dendrites with 4-fold symmetry, and smaller dendrites at low, moderate and high undercooling temperatures are observed. Same solidification behaviours were reported for pure silicon [2] and pure germanium [3]. At low undercooling silicon, germanium and silicon-germanium alloys tend to form facets on the $\{111\}$ crystal planes. Growth is limited by 2D nucleation on these facets and spreading of the atomic steps parallel to the faceted planes [4]. A further increase of the undercooling leads to a roughening of the solid-liquid interface at the atomic scale. This effect is identified as kinetic roughening of a smooth solid-liquid interface as also simulated by molecular dynamic [5].

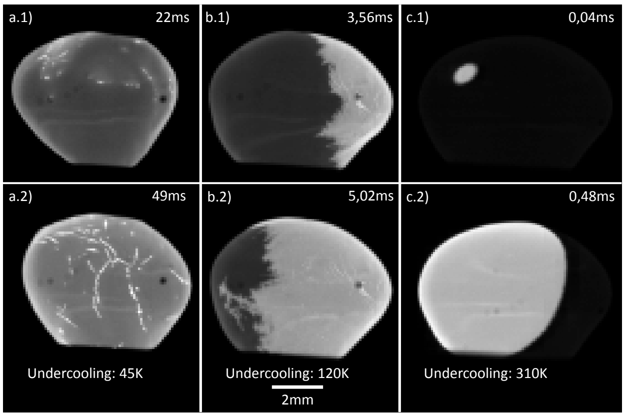

FIG. 2: The solid/liquid interface on the surface of $Si_{75}Ge_{25}$ solidified from the undercooled melt at ΔT of (a) 45 K, (b) 120 K, and (c) 310 K. The undercooled melt is grey while the solid phase is brighter. In the upper right corner is the time after recalescence.

We observed the transition from plate-like crystals to isolated dendrites with 4-fold symmetry at undercoolings of approx 100 K, 70 K, 80 K, 85 K and 140 K for pure silicon, $Si_{75}Ge_{25}$, $Si_{50}Ge_{50}$, $Si_{25}Ge_{75}$ and pure germanium, respectively. A higher transition undercooling correlate with a lower interfacial energy anisotropy, a critical parameter used for the modelling in FIG. 1.

We suspect that the difference in anisotropy affects the transition from plate-like crystals to isolated dendrites with 4-fold symmetry or rather is responsible for kinetic roughening of a solid-liquid interface. It can explain the lower dendrite growth velocity of Ge compared to Si as well.

Financial support by RGS Development is gratefully acknowledged.

[*] Corresponding author: `daniel.simons@dlr.de`

[1] J. Lipton, W. Kurz and R. Trivedi, Acta Metallurgica **35**, 957 (1987).
[2] T. Aoyama and K. Kuribayashi, Acta materialia **48**, 3739 (2000).
[3] D. Li and D. M. Herlach, Physical Review Letters **77**, 1801 (1996).
[4] K. Fujiwara, International Journal of Photoenergy **2012**, 16 (2012).
[5] K. A. Jackson, Journal of Crystal Growth **198-199**, 1 (1999).

The influence of intermetallic phases on the permeability in AlSi7Fe1 alloy

S. Steinbach,[1,*] L. Ratke,[2] G. Zimmermann,[3] and O. Budenkova[4]

[1] *Institut für Materialphysik im Weltraum, Deutsches Zentrum für Luft- und Raumfahrt (DLR), 51170 Köln, Germany*
[2] *Institut für Werkstoff-Forschung, Deutsches Zentrum für Luft- und Raumfahrt (DLR), 51170 Köln, Germany*
[3] *ACCESS e.V., 52072 Aachen, Germany*
[4] *Science et Ingenierie des MAteriaux et Procedes (SIMAP), 38402 St. Martin D'Heres, France*

Iron is a common impurity element in cast aluminum alloys. During casting Fe−containing intermetallics like the β-Al$_5$SiFe phase are formed between the aluminum dendrites, causing porosity and shrinkage defects. To understand the effect of convective flow on the microstructure of an alloy with intermetallic phases precipitated in the mush and to understand the effect of intermetallic phase formation on permeability, solidification experiments with a hypoeutectic Al-6.5wt.%Si-0.9wt.%Fe alloy were performed. The samples were directionally solidified on-board of the International Space Station ISS in the ESA payload Materials Science Laboratory (MSL) equipped with the Low Gradient Furnace (LGF) under both purely diffusive and forced convective conditions [rotating magnetic field (RMF)].

One parameter used to characterize fluid flow in a mushy zone is permeability, i.e. a tensor measuring the ease of fluid flow through the solid network. In order to determine the influence of the intermetallic phases on the permeability of the dendritic network, the flow problem based on the Stokes equations was simulated using reconstructed cubes from 3D CT analysis (Phoenix nanotom, pixel size $1 \mu m$) of outer part of samples solidified with RMF. Fig. 1 shows the large and plate-like intermetallic β-Al$_5$SiFe phase. They form a complex and interconnected network.

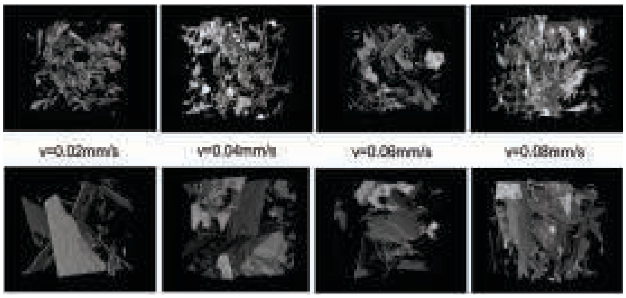

FIG. 1: Segmented reconstruction cubes of 650 x 650 x 650 μm^3 of samples processed with controlled melt flow and different furnace movement velocities. Top images were taken from the outer parts of the sample and bottom images were taken from the sample center.

The commercial computational flow dynamics software Avizo XLab Hydro (VSG, France), which utilizes a finite volume method, was applied directly to the tomographic datasets for flow predictions [1]. The permeability values calculated and extracted from the flow simulations have been fitted to an empirical relationship based on the Blake-Kozeny equation following the procedure of Poirier [2] and Puncreobutr [3] considering the liquid volume faction and the fraction of the β-phase, obtained from thermodynamic calculations with a linearized phase diagram.

It can be seen in Fig. 2 that in the first solidification phase the permeability decreases monotonically with temperature as expected because of the thickening of the primary dendrites as solidification progresses. The permeability is significantly lower for the case with fluid flow as compared to the one without, because of the primary dendrite spacing reduced by fluid flow [4].

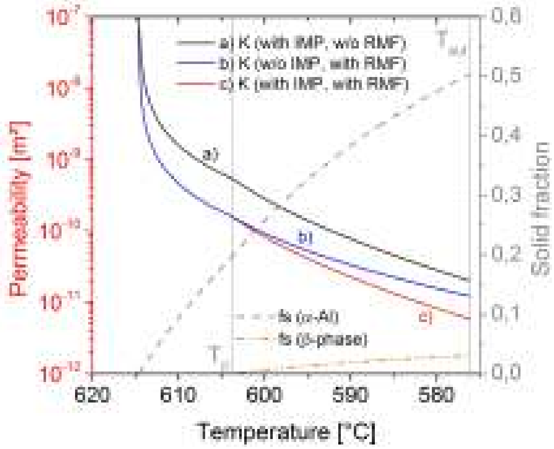

FIG. 2: The evolution of permeability with temperature for flow parallel to the primary columnar dendrites a) without fluid flow but with IMP, b) with fluid flow but without IMP and c) with IMP and fluid flow. For comparison the evolution of the fraction solid of the $\alpha - Al$ dendrites and the β-Al$_5$SiFe phase with temperature is also provided. The dotted lines indicate the temperature where the nucleation of the intermetallic phases (T$_{beta}$) and the ternary eutectic (T$_{eut}$) started.

During the solidification phase after beginning of intermetallic phase precipitation, the loss of permeability that occurs due to the intermetallic phases can be directly attributed to the barrier effect of the β-Al$_5$SiFe. They are able to block flow through the interdendritic network of channels. This can explain the decrease in the feeding abilities in castings and could therefore explain the increased susceptibility of such alloys for casting defects as hot tearing and microporosity.

This research was funded by ESA under contract number 4200014347/00/NL/SH AO-99-031 (MICAST).

[*] Corresponding author: `sonja.steinbach@dlr.de`

[1] S. Steinbach, L. Ratke, G. Zimmermann and O. Budenkova, Journal of Physics, accepted
[2] D. R. Poirier, Metall. Trans. **18**, 245 (1987).
[3] C. Puncreobutr, A. B. Philion, J. L. Fife and P. D. Lee, Acta Mat. **64**, 316 (2014).
[4] S. Steinbach and L. Ratke, Intl. J. Cast Met. Res. **22**, 1 (2009).

Nucleation transitions in undercooled $\mathrm{Cu}_{70}\mathrm{Co}_{30}$ immiscible alloy

Y. Zhang,[1,2,3] C. Simon,[2] T. Volkmann,[3,*] M. Kolbe,[3] D.M. Herlach,[3] and G. Wilde[2]

[1] Key Laboratory of Electromagnetic Processing of Materials, Northeastern University, Shenyang 110004, China
[2] Institute of Materials Physics, University of Münster, 48149 Münster, Germany
[3] Institut für Materialphysik im Weltraum, Deutsches Zentrum für Luft- und Raumfahrt (DLR), 51170 Köln, Germany

Crystal nucleation in undercooled melts is a fundamental process during solidification [1]. According to the classical nucleation theory (CNT) homogeneous nucleation of the crystalline phase is based on statistical fluctuation of the density in the melt. In practice, heterogeneous nucleation is the major process, where the formation of crystal nuclei is initiated by extrinsic solid phases such as metal oxides. A direct observation of nucleation events in metallic systems is difficult to perform. A suitable method for determination of the nucleation rate J and the distinction between homogeneous and heterogeneous nucleation is the statistical analysis of the maximum undercooling of a sample that is repeatedly melted and solidified under identical conditions as reported for pure Al by Uttormark et al. [2].

In the present study [3] nucleation phenomena have been analyzed on $\mathrm{Cu}_{70}\mathrm{Co}_{30}$ alloy melts, which reveal a metastable miscibility gap. Below the metastable binodal line the undercooled liquid separates in a way that Co-rich droplets are dispersed in a Cu-rich liquid matrix. During further cooling the Co-rich droplets crystallize first while the Cu-rich matrix remains liquid. Such a separated sample provides ideal conditions for nucleation studies since the Co-rich droplets are completely embedded and protected against the formation of surface oxides.

The $\mathrm{Cu}_{70}\mathrm{Co}_{30}$ master alloy was inductively melted, homogenized and then atomized into small droplets, which solidified during free fall in a drop tube. By using this method samples with identical composition were obtained, which were then subjected to nucleation studies by Differential Scanninning Calorimetry (DSC). Samples with different masses (23.58 mg, 9.45 mg and 4.35 mg) were processed during 120 melting and cooling cycles. The undercooling $\Delta T_{Co-rich} = T_L(Co-rich) - T_N$ is defined as the difference of the liquidus temperature at the composition of the Co-rich phase, $T_L(Co-rich)$, and the onset temperature of nucleation T_N. The average undercooling increases with decreasing sample mass and was found to be 328, 330, and 332 K for 23.58, 9.45 and 4.35 mg, respectively. Due to the stochastic nature of nucleation, the events occur over a temperature interval of the order of 10 K. The survivorship function

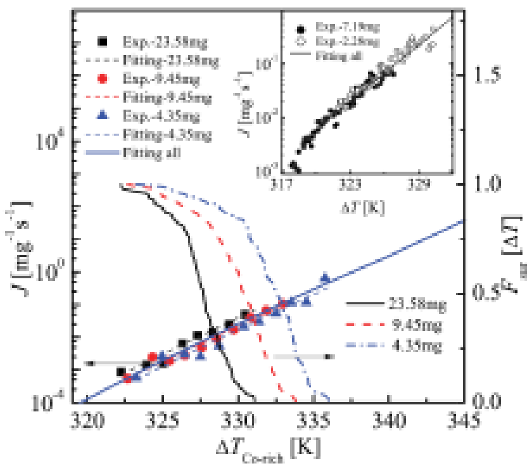

FIG. 1: Survivorship function $\mathrm{F}_{sur}(\Delta T)$ and the nucleation rate per unit mass J as a function of $\Delta T_{Co-rich}$ obtained for different sample masses. The insert shows the nucleation rate for pure Co.

$$F_{sur}(\Delta T) = 1 - exp\left(-\int J(\Delta T)dt\right) \quad (1)$$

derived from Poisson statistics describes the probability that at a given undercooling ΔT no nucleation event occurs. From the DSC scans $F_{sur}(\Delta T)$ is derived from the fraction of cooling cycles in which crystallization did not yet set in at ΔT. Fitting the experimental data to Eq. 1 yields the nucleation rate as a function of undercooling ΔT as displayed in Figure 1. According to CNT the nucleation rate

$$J = \Gamma \cdot exp\left(-\frac{\Delta G^*}{k_B T}\right) \quad (2)$$

is dominated by the nucleation barrier ΔG^* which is the activation energy for the formation of a nucleus of critical size, and the kinetic prefactor Γ which depends on the growth rate of the critical nucleus and the number of potential nucleation sites. The kinetic prefactor is found to be $\Gamma = 2.64 \cdot 10^{37}$ m^{-3} s^{-1} which is close to 10^{39} m^{-3} s^{-1} expected for homogeneous nucleation, where each atom can act as a nucleation site [4]. The value of Γ for pure Co is much smaller and was determined to $\Gamma = 1.77 \cdot 10^{33}$ m^{-3} s^{-1}. These results indicate the occurance of homogeneous nucleation in the Co-rich droplets. Apparently, the Cu-rich liquid matrix has a retarding effect on heterogeneous nucleation in the separated Cu-Co melts.

The work was supported by the Alexander von Humbold Foundation and the Deutsche Forschungsgemeinschaft.

[*] Corresponding author: `thomas.volkmann@dlr.de`

[1] K.F. Kelton and A.L. Greer, *Nucleation in Condensed Matter*, Elsevier, Amsterdam, 2010.
[2] M.J. Uttormark, J.W. Zander, and J.H. Perepezko, J. Cryst. Growth **177**, 258 (1997).
[3] Y. Zhang, C. Simon, T. Volkmann, M. Kolbe, D.M. Herlach, and G. Wilde, Appl. Phys. Lett. **105**, 041908 (2014).
[4] D. Turnbull, Contemp. Phys. **10**, 473 (1969).

1.4 Granular Matter

Microrheology in a driven two-dimensional granular system

B. Eberhardt,* P. Yu, S. Frank-Richter, S. Pitikaris, and M. Sperl

Institut für Materialphysik im Weltraum, Deutsches Zentrum für Luft- und Raumfahrt (DLR), 51170 Köln, Germany

Microrheology is a technique used in disordered systems to probe the dynamic behavior on a local scale. A tracer particle is embedded into the system and its trajectory is measured to learn about the local structure and dynamics of the medium.

In this work a two-dimensional granular fluid is driven vertically by a vibrating table to agitate the disk-shaped particles. The particles are made from ABS filament and are printed by an experimental 3D printer. A unique barcode is placed on top of every particle. A high speed camera records the motion of the particles so that an image processing algorithm can track the trajectory of every individual particle [2].

The tracer particle is pulled through the system in constant force or constant velocity mode (cf. Fig. 1).

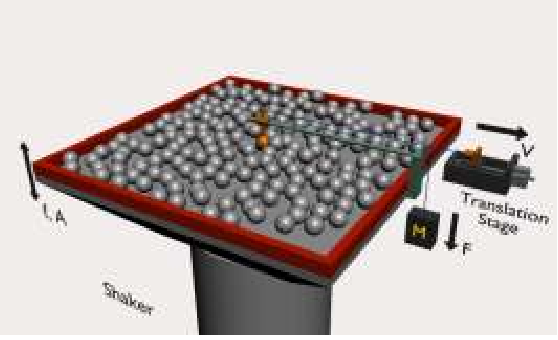

FIG. 1: Illustration of the experimental setup with the two pulling modes: constant force via a weight and constant velocity via a translation stage.

The mean free path of the tracer particle in the granular medium is negligible compared to its own diameter at packing fractions higher than $\varphi \sim 0.65$. Hence, the tracer frequently collides with the surrounding particles and consequently does not follow a straight path.

We can calculate the kinetic energy of every particle since the image processing algorithm tracks the trajectories of all particles by their barcode. The host particles show average kinetic energies in the low μJ-range. The pulling velocities used for the tracer particle lead to kinetic energies comparable to the average energy of the system's host particles.

In this energy range, theory predicts a shear thinning behavior [1]. In order to check this prediction, we measure the average force experienced by the tracer particle and compute the corresponding friction of the system by dividing the force by the pulling velocity $\zeta = F/v$. In constant velocity mode, a clear trend is observable (cf. Fig. 2): The average friction decreases with increasing pulling velocities which is consistent with the theoretical work. At the same time, lower packing fractions show lower average force.

In addition, [1] predicts a plateau in the friction-velocity curve for smaller velocities and forces than the ones investigated here. For higher velocities shear thickening is expected.

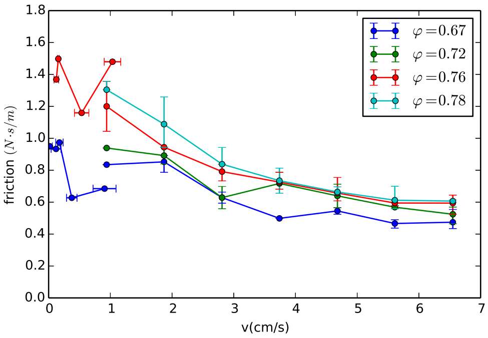

FIG. 2: Friction of the granular system at the applied constant velocities. Shear thinning behavior can be observed as the friction decreases at higher velocities [3].

Compared to the friction obtained from constant force mode the results are in the same order of magnitude and appear to be consistent with each other. However, the measurements with constant force show a much stronger variation in the friction (see Fig. 2 for $v \leq 1$ cm/s).

[*] Corresponding author: `boris.eberhardt@dlr.de`

[1] T. Wang, M. Grob, A. Zippelius and M. Sperl, Phys Rev E **89**, 042209 (2014)
[2] E. Stärk, PhD thesis (2012)
[3] B. Eberhardt, Diploma thesis (2014)

Nonlinear Sound Propagation in Granular Packings under Low Gravity

P. Yu,* S. Subatzus, and M. Sperl

Institut für Materialphysik im Weltraum, Deutsches Zentrum für Luft- und Raumfahrt (DLR), 51170 Köln, Germany

Sound propagation in granular packings is known to exhibit nonlinear behavior [1], due to disordered particle positions, nonlinear contact forces between particles, and inhomogeneous elastic properties of the packings. This nonlinear behavior becomes even more prominent when a tight packing approaches the jamming point. Simulations [2] and experiments on ground [3, 4] have been performed in this regime, the most important result of which is a changing speed of sound (V_s) with a changing sound magnitude (P_m) ([3], Fig. 3), a clear signal of shock-wave-like nonlinear sound propgations.

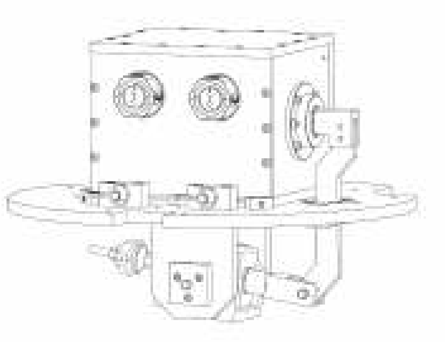

FIG. 1: Setup for a droptower experiment. Glass beads are placed inside a cubic sample cell on top of a base plate. A solenoid beneath the base plate drives a hammer (to the right of the sample cell) to excite sound waves in the packing. Two force sensors buried inside the packing measure the signals and send them out via the two feedthroughs on the front side of the sample cell.

However, an ideal state, where all particles in the packing only barely touch each other, can not be reached in labs, due to the pressure gradient introduced by the weight of the particles themselves. To explore this region where nonlinear behavior is expected to be richest, we designed a sound generation and measurement device (Fig. 1) for a drop tower experiment. This device has a compact size and is fully automated compared to previous lab setups.

A drop tower campaign using this device was performed in April, 2014. Fig. 2 shows two sound signals recorded by the two sensors during a 9.5-second long low gravity (ca. $10^{-6}g$) period. In between the two very large peak pairs at the beginning and the end, which were induced by the hyper-g phases, there are 25 pairs of sound measurement. The inset shows one such typical pair. The time of flight t_f in between two peaks and the speed of sound V_s can be directly measured.

In total we have 8 drops with roughly the same P_0 (0.51 kPa$\pm 5\%$, the lowest pressure from previous lab measurement is 0.9 kPa) but different P_m. We see a clear change of V_s from different drops (Fig. 3) for all of different P_m, indicating that we are always in the nonlinear regime. On this log-log plot, the data points are roughly on a straight line with a slope about 0.213, close to that observed in previous lab measurement ($1/6$, [3]). The fact that a trend to have a constant V_s for small P_m values has not been seen proves that one can keep within nonlinear regime when even less P_m is applied. Compared with Fig. 3 of [3], we conclude that low gravity does expand the nonlinear regime of sound propagation.

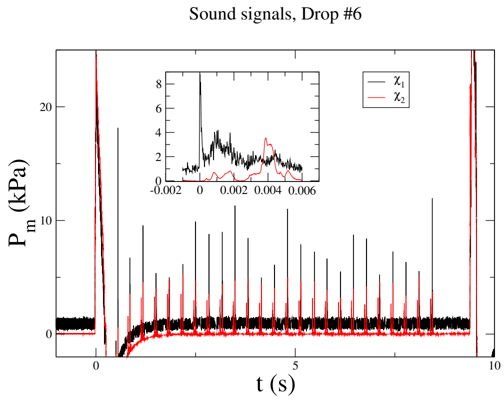

FIG. 2: Complete signal from one drop; Inset: typical example of a peak pair. The black/red curve is the signal measured from a sensor closer to/further from the sound source.

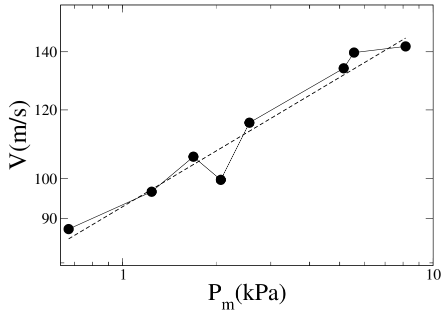

FIG. 3: Speed of sound versus sound magnitude.

Another low-gravity campaign is scheduled to obtain more statistics of data with a wider range of P_m.

* Corresponding author: `peidong.yu@dlr.de`

[1] C. Liu and S. R. Nagel, Phys. Rev. Lett. **68**, 2301 (1992).

[2] L. R. Gomez, A. M. Turner, M. van Hecke, and V. Vitelli, Phys. Rev. Lett. **108**, 058001 (2012).

[3] S. van den Wildenburg, R. van Loo, and M. van Hecke, Phys. Rev. Lett. **111**, 218003 (2013).

[4] S. van den Wildenburg, M. van Hecke, and X. Jia, Euro. Phys. Lett. **101**, 14004 (2014).

Diffusing wave spectroscopy on granular media

P. Born,* M. Bußmann, J. Schmitz, L. Redmond, and M. Sperl
Institut für Materialphysik im Weltraum, Deutsches Zentrum für Luft- und Raumfahrt (DLR), 51170 Köln, Germany

Diffusing wave spectroscopy (DWS) measurements on driven granular media presently yields results in disagreement to complementary techniques. It is not clear whether the higher spatial and temporal resolution of DWS or an incomplete adaption of the DWS methodology to granular media is the reason. One aspect that complicates evaluation of DWS measurements is the driving mechanism to agitate the particles in the medium. The driving is inhomogeneous in ground-based experiments, as the agitation has a prevailing direction to counter sedimentation. The situation improves by performing experiments in microgravity.

We realized a setup for microgravity DWS measurements in drop tower or sounding rockets flights (Fig. 1) [1]. The granular particles are driven by mass-flow controlled turbulent air streams. This provides agitation without any moving components in the sample cell. The particle motions consequently become the unambiguous origin of measured intensity fluctuations, in contrast to driving by vibration of piezo crystals or sample walls [2].

Here we study the influence of particle interactions on the DWS signal measured in drop tower flights. Strong interactions emerge from triboelectric charging of the particles. We integrated a control of charging by controlling ambient humidity [3]. The change in charging behavior is also visible in the intensity autocorrelation functions g2 (Fig. 2, upper panel). At constant gas flow packing fraction, dry and charging particles cause a slower decay of intensity correlations than uncharged particles.

Adhesion among the particles was Further reduced by coating the particles in the granular medium with hydrophobic nanoparticles to roughen the surface, lower the real contact area and minimize surface forces. In Fig. 2, lower panel, measurements on samples with different packing fractions are shown. No particle dynamics are detectable in samples without a roughened surface until substantially lowering the packing fraction away from the jamming condition. In samples with roughened surface, even at a packing fraction close to jamming particle motions are detectable. At the same packing fractions, decay of intensity correlation is faster in the sample with roughened surface. A second decay in the intensity autocorrelation becomes apparent at the lowest packing fraction in both cases. This is similar to results obtained in laboratory measurements on ground, where at strong driving bubbles form and a second decay occurs [4].

FIG. 1: CAD-drawing of the experimental module. The laser and detectors are mounted on the top panel, the gas agitation system and the sample cell on the middle panel. Below the middle panel a collimator feeds the light into fiber waveguides attached to the detectors on the top panel.

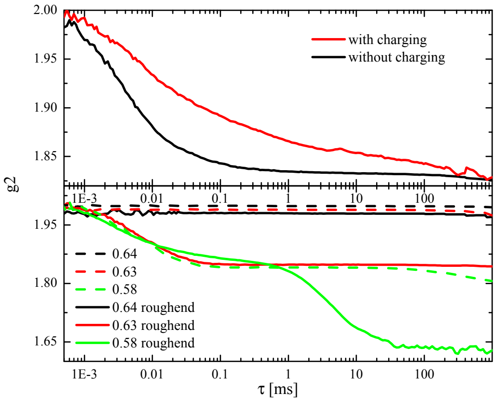

FIG. 2: Effect of triboelectric charging (top) and adhesion (bottom). Intensity correlation $g2$ decays faster without charging. Intensity correlation indicates dynamics even close to the jamming in samples with lowered adhesion (roughened surface). A plateau emerges only at low packing fraction. Top three curves in the lower panel are offest for clarity.

In conclusion, particle dynamics in granular media as measured with DWS cannot be described by hard sphere kinetics only. The influence of long range electrostatic and short ranged adhesive interactions has to be taken into account. A second decay in the intensity autocorrelation is most likely an effect of particle number fluctuations, not an aspect of particular granular dynamics.

---

[*] Corresponding author: `philip.born@dlr.de`

[1] L. G. Redmond, *Auslegung und Design eines Moduls für Lichtstreuung an granularen Medien auf einer Forschungsrakete*, Bachelorarbeit, FH Aachen, 2014.

[2] M. Bußmann, *Entwicklung und Konstruktion einer Probenzelle zur Messung gas-getriebener Partikeldynamik mittels Lichtstreuung*, Bachelorarbeit, FH Aachen, 2013.

[3] J. Schmitz, *Optimierung und Test eines Fallturmexperiments zu dynamischer Vielfachstreuung an Granulaten*, Bachelorarbeit, FH Aachen, 2014.

[4] S. Reinhold, *Lichtstreuung an getriebenen granularen Medien*, Diplomarbeit, Bonn, 2012.

Particle characterization using THz spectroscopy

P. Born,[1,*] K. Holldack,[2] and M. Sperl[1]

[1] *Institut für Materialphysik im Weltraum, Deutsches Zentrum für Luft- und Raumfahrt (DLR), 51170 Köln, Germany*
[2] *Helmholtz-Zentrum Berlin für Materialien und Energie GmbH, Albert- Einstein-Str. 15, 12489 Berlin, Germany*

Currently emerging THz technologies offer new ways for investigations of granular particle ensembles. The wavelength of THz radiation in the range of 30 μm to 3 mm matches particle sizes in many typical granular media. Consequently, situations known from measurements in the colloidal regime using visible light or from x-ray based measurements on atomic and molecular structures can be reproduced. Angle-resolved static light scattering measurements in the THz regime from granular media have been shown to deliver particle sizes and packing characteristics of optically thin samples [1].

Here we show the possibility to characterize particles in granular media using broad-band THz spectroscopy [2], a method that offers the advantage of measurements on multiple-scattering samples where only little information is gained from angle-resolved scattering. The measurements were carried out in transmission geometry under vacuum using the high-resolution FTIR spectrometer available at the BESSY II storage ring. The spectral range of the measurements covered wavenumbers ν = 20...370 cm^{-1}. The extinction E of the samples was obtained from the measured intensity with sample I_1 and the reference intensity I_0 by $E = -ln(I_1/I_0)$. Lambert-Beer's law suggests that E is proportional to the extinction efficiency Q_e of the particles up to a proportionality factor.

Figure 1 depicts the sensitivity of the measured extinction of polystyrene and polyethylene particles to the particle size. The extinction curves all collapse onto a single master curve when plotted against the phase shift $\rho = 2 \cdot x \cdot |m-1|$ created by the particles, where $x = 2\pi a \cdot \nu/10000$ is the size parameter of a particle with radius a at a wavenumber ν and m is the refractive index of the particles. In particular, the first extinction maximum occurs at a fixed phase shift created by the particles of $\rho \approx 4.2$. Picking the wavenumber ν_{max} at the first extinction maximum gives a quick estimate of the mean particle size, $a_{\text{spec}} \approx \frac{4.2\cdot 10000}{4\pi|m-1|\cdot\nu_{max}}$. The differences among the measured extinction and the theoretical prediction (see inset in Fig. 1) can be attributed to the size distribution of the particles used in the experiments, which tends to average the oscillations present in the result for monodisperse spheres. We derive an empirical formula to relate the polydispersity index PDI to the average slope using a Gaussian size distribution in the Mie theory calculations, PDI $= 47.9 - 68.7 \cdot \nabla_{Q_e}$. The obtained relations allow a fast particle characterization in granular media using THz extinction measurements. The applicability of this approach is illustrated in Figure 2. The results from spectroscopy match very well with results using light microscopy. Still spectroscopy has the potential to measures thousands of particles in three-dimensional samples simultaneously, even in-situ and up to packing densities with multiple scattering.

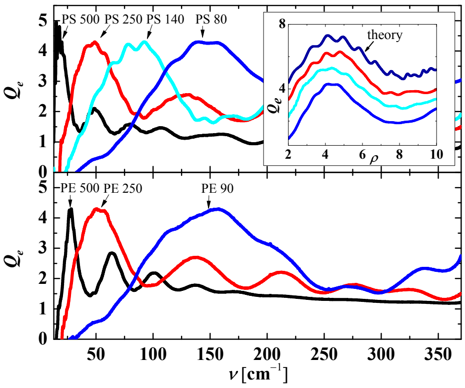

FIG. 1: Measured extinction efficiencies Q_e of PS (upper panel) and PE (lower panel) particles. The labels indicate nominal particle diameters in μm. The inset in the upper panel shows a close-up of the first extinction peak plotted as a function of the phase shift ρ created by the PS particles. The offset curves are sorted by the polydispersity of the particles (color-coding as in the main diagram). The top curve is the calculated extinction efficiency of monodisperse particles.

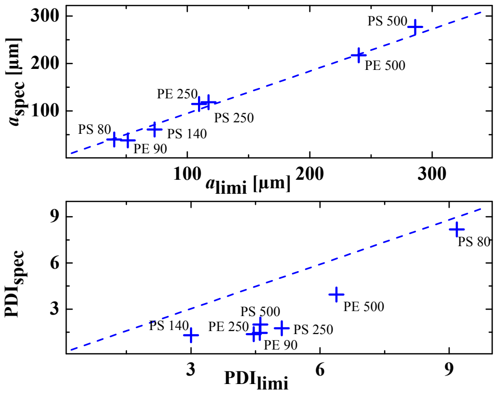

FIG. 2: Results of the particle characterization using THz spectroscopy. The upper diagram shows the particle radii measured using THz spectroscopy (a_{spec}) plotted versus the radii measured using light microscopy (a_{limi}). The lower diagram shows the polydisersity index measured using THz spectroscopy (PDI$_{\text{spec}}$) plotted versus the polydispersity measured using light microscopy (PDI$_{\text{limi}}$). The dashed lines give the diagonals, $a_{\text{spec}} = a_{\text{limi}}$ and PDI$_{\text{spec}}$ = PDI$_{\text{limi}}$.

The authors acknowledge the help of B. Eberhard, P. Yu, and Z. Evenson with the measurements at Bessy II.

---

* Corresponding author: `philip.born@dlr.de`

[1] P. Born, N. Rothbart, M. Sperl, and H.-W. Hübers, Europhysics Lett. **106**, 48006 (2014).
[2] P. Born, K. Holldack, and M. Sperl, Granular Matter, under review, arXiv preprint arXiv:1407.6592.

Granular Stress-Birefringence in 3D Binary Mixtures

S. Frank-Richter,* M. Sperl, and P. Yu
Institut für Materialphysik im Weltraum, Deutsches Zentrum für Luft- und Raumfahrt (DLR), 51170 Köln, Germany

Stress-birefringence has been widely used in two and three dimensional granular studies to visualize the contacts and forces among granular particles made of suitable material. We show results from binary mixtures of particles with respectively two sizes and varying concentrations. For asymmetric mixtures exceeding size ratios 1:3 we find strong variations in the transition densities as well as in mechanical properties at the transition.

The following packing properties characterise a granular system:
1. When a granular system is compressed it becomes mechanically stable at a critical packing fraction φ_c. This state is called random-close packing and appears for 3D monodisperse systems at $\varphi_c \approx 0.64$ [1].
2. Bidisperse granular systems consisting of n_A big spherical particles A with radius r_A and n_B small particles B with radius r_B. Such systems are characterized by the parameters size ratio $\delta = \frac{r_B}{r_A}$, volume mixing ratio $\hat{x}_B = \frac{n_B V_B}{n_A V_A + n_B V_B}$ with $V_A = \frac{4}{3}\pi r_A^3$ and $V_B = \frac{4}{3}\pi r_B^3$. and packing fraction $\varphi = \frac{n_A V_A + n_B V_B}{V_C}$ with V_C for the container volume.
To visualize the stresses in a granular system, one can use an optical setup with stress-birefringent particles between a polarized lightsource and a polarizer (see Fig. 1).

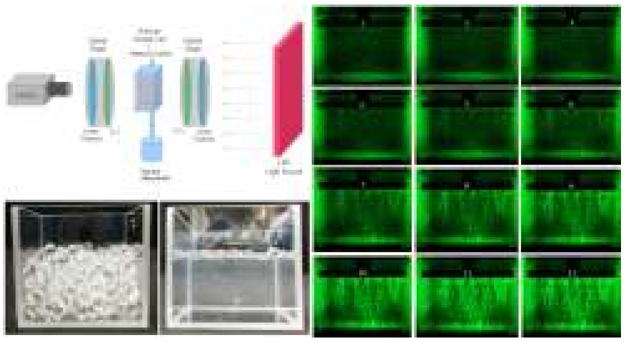

FIG. 1: Setup for the 3D stress-birefringence experiment. PDMS spheres [2] are placed in a glass container (5x5x5cm^3) between two circular polarizers (upper left) to visualize the stresses inside the packing. To avoid multiple scattering the spheres are contained in an index matched environment of 44% pure water and 56% glycerol (lower left). The picture series show the stress development inside the packing during compaction. The random-close packing transition happens between picture (5) and (6) at a packing fraction of $\varphi_c \approx 0.676$. The packing has the parameters $\delta = 0.4$ and $\hat{x}_B = 0.38$ with around 3000 individual particles.

For data analysis we use the mean intensity I_{mean} from each individual picture (see Fig. 2) . The transition density φ_c is then determined by the intersection between the baseline and the linear fit to the increasing mean intensity. The slope η of the linear fit to I_{mean} indicates the inner stress development of the packing during compaction. With an additional dataset, provided by a pressure measurement, we also determined the bulk modulus $\kappa = -V\frac{dP}{dV}$ for each packing.

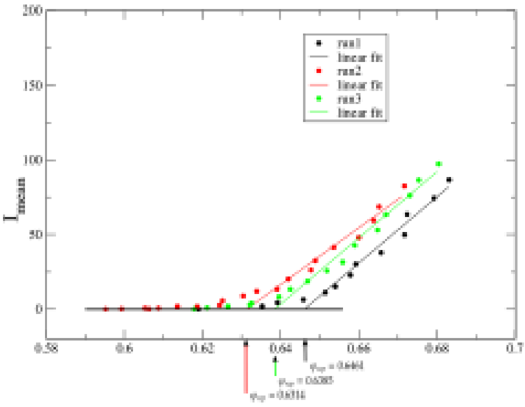

FIG. 2: I_{mean} for three different experimental runs for packings with $\delta = 0.4$ and $\hat{x}_B = 0.38$.

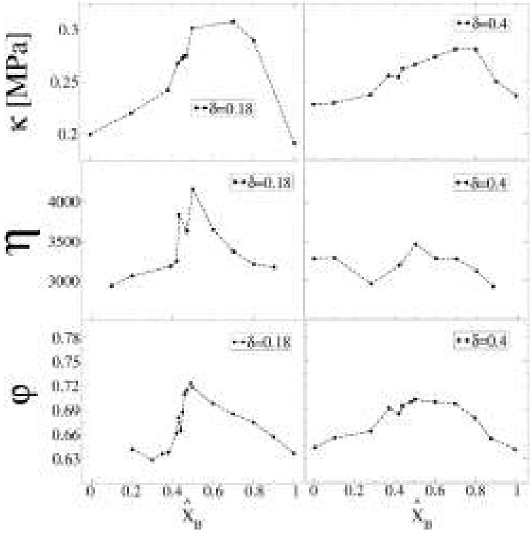

FIG. 3: Resulting diagrams for packings with $\delta = 0.18$ and $\delta = 0.4$ and different mixing ratios $\hat{x}_B$. The diagrams show the transition densities φ_c, the inner stress development η and the bulk modulus κ.

In Fig. 3 it can be seen, that mixtures with strongly asymmetric size ratios exhibit a jump in all measured quantities. This jump vanishes for packings with larger size ratios[3].

---

* Corresponding author: `stefan.frank-richter@dlr.de`

[1] Scott, G.D., Kilgour, D.M.: The density of random close packing of spheres. Brit. J. Appl. Phys. **2**, 863 (1969).
[2] S. Frank-Richter, M. Sperl, P. Yu, application number DE 102011014084A1
[3] S. Frank-Richter PhD thesis: Disordered Binary Granular Packings in Three Dimensions. Düsseldorf (2014)

1.5 Theory and Simulation

Length scale for transport coefficients in glass-forming liquid

H. L. Peng,[1,*] Th. Voigtmann,[1] and H. R. Schober[2]

[1] *Institut für Materialphysik im Weltraum, Deutsches Zentrum für Luft- und Raumfahrt (DLR), 51170 Köln, Germany*
[2] *Institut für Festkörperforschung, Forschungszentrum Jülich, D-52425 Jülich, Germany*

Approaching to glass transition temperature, the dynamic of supercooled liquids drastically slows down and eventually diverges, i.e. the relaxation time of system goes to infinite. Usually this time scale divergence is accompanied by the divergence of length scale. Numerous simulation works also show drastic increase of correlation length, extracted from four-point correlation function in under-cooling liquids. However, how the length scale underlying for transport coefficients grows with under-cooling temperature is still unclear.

We conduct molecular dynamic (MD) simulations for a glass-forming Lennard-Jones mixture using Kob-Anderson parameters at the composition $\mathrm{A}_{80}\mathrm{B}_{20}$ with fixed pressure (=5.0 in L-J units). Length scale for diffusivity and viscosity are investigated via finite size effect and wave-vector dependent behaviour. Finite size effect for viscosity shows saturated box length at low temperature, while an unsaturated correlation length from wave-vector behaviour. This indicates a finite length scale for Cooperative Rearrangement Region (CRR) of slow relaxation region, but a diverging length scale for clustering of CRR at low temperature. Length scale from size effect of diffusivity shows similar behaviour with the length scale from wave-vector behaviour of viscosity.

Finite size effect is a powerful tool to detect any process involving cooperative movement or long-range interaction. For any thermally activated process:

$$A = A_0 \exp[E(T)/k_B T] \tag{1}$$

where A can be η or $1/D$, and $E(T)$ is corresponding thermal activation energy. For strong liquid, $E(T)$ is a constant, independent of temperature, while for fragile liquid, $E(T)$ increases with cooling degree increase, indicating growth of activation volume. Thus, in fragile liquid, if the simulated box size is smaller than activation volume, the system would became constraint then derivates from bulk system. From this we would define a critical box length L_c required as the smallest box length to reach its bulk value. The value of L_c acts as the up limit of correlation length for corresponding activation process.

Left picture in FIG. 1 shows the calculated L_c value for diffusivity and viscosity. There is only slight difference for L_c between diffusivity and viscosity at small supercooled regime (the onset for breakdown Stokes-Einstein relation is around 0.6), but large difference at highly supercooled regime. The viscosity, which is mainly determined by slow particle's movement, indicates frustrated unit of CRR has a up-limited length size at low temperature.

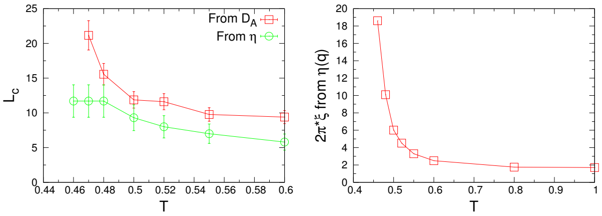

FIG. 1: Left: critical box length extracted from finite size result for diffusivity of particle A and viscosity; Right: Correlation length value obtained from q-dependent viscosity.

On the other hand, the length scale for transport coefficients can be investigated by wave-vector dependent behaviour. The q-dependent viscosity is calculated from the transverse current autocorrelation function [1, 2]. Transverse current is defined as: $C_t(q,t) = q^2/N\langle \mathbf{j}_{\vec{q}}^{\perp}(t)\mathbf{j}_{\vec{q}}^{\perp}(0)\rangle$, with $\mathbf{j}_\mathbf{q} = \sum_i^N \mathbf{u}_i(t)\exp[-i\mathbf{q}\cdot\mathbf{r}(t)]$. Here, $\perp$ presents wave vector $\vec{q}$ is perpendicular to the velocity $\mathbf{u}$. Then the generalized viscosity is defined by:

$$\eta(q) = \rho_m k_B T/\tilde{C}_t(q, z = 0) \tag{2}$$

where $\tilde{C}_t(q, z = 0)$ is the Laplace transform of $C_t(q,t)$. In zero-q limit, eq. 2 will give the hydrodynamic value, i.e. $\eta(q \to 0) = \eta_H$, with $\eta_H = V/k_B T\int_0^\infty \langle P_{xy}(t)P_{xy}(0)\rangle dt$. By empirical fitting: $\eta(q) = \eta_H/[1 + (\xi q)^2 + (\zeta q)^4]$, we can get correlation length for viscosity as $2\pi\xi$. As this length scale is calculated from transverse current, it should coincide with the length scale of transverse wave propagation. In zero-q limit, transverse current decays exponentially as hydrodynamic theory predict. At finite wave vector number, the transverse mode shows negative correlation and damping oscillation as viscous model predict. Thus, there exits a longest wave length which can propagate in the liquid, separating hydrodynamic regime and viscous regime. This longest wave length is a characteristic length scale for supercooled liquid.

Right picture in FiG. 1 shows this length. At high temperature, the value is in good agreement with finite size result of viscosity, but bifurcates at low temperature. This correlation length indicates a divergence-like behaviour as approaching glass transition temperature. Note the correlation length at lowest temperature is even larger than the box size used to do this calculation. As the argument of frustration [3], this length is not a measure of the size of CRRs, but the clustering of these regions. How these regions aggregate together and influence the diffusivity is still unclear.

---

[*] Corresponding author: `hailong.peng@dlr.de`

[1] J. P. Hansen and I. R. Macdonald, *Theory of Simple Liquids* (Academic Press, Oxford, 2005).
[2] A. Furukawa and H. Tanaka, Phys. Rev. Lett. **103**, 135703 (2009).
[3] R. D. Mountain, J. Chem. Phys. **102**, 5408 (1995).

Glass Transition of Charged Particles in Two-Dimensional Confinement

A. Yazdi,[1,*] M. Heinen,[2] Alexei Ivlev,[3] and M. Sperl[1]

[1] *Institut für Materialphysik im Weltraum, Deutsches Zentrum für Luft- und Raumfahrt (DLR), 51170 Köln, Germany*
[2] *Division of Chemistry and Chemical Engineering, California Institute of Technology, Pasadena, California 91125, USA*
[3] *Max-Planck-Institut für extraterrestrische Physik, 85741 Garching, Germany*

A two dimensional configuration of charged particles is observed in various kinds of experiments including colloidal suspensions confined between two layers or dust particles levitating in a weakly ionized plasma. In an equilibrium condition and Boltzmann distribution of surrounding ions, the interaction between a monolayer of charged particles has been modeled with the repulsive Yukawa interaction $U_Y(x)/k_{\rm B}T = \Gamma_Y \exp(-\kappa_Y x)/x$. $x = r\sqrt{n}$ is the dimensionless distance between particles, where n is the number density of N particles in a 2D area L^2. κ_Y is the screening parameter which is the inverse of the dimensionless screening length $\kappa_Y = 1/\lambda_Y\sqrt{n}$ and $\Gamma_Y = Q_Y^2 e^2\sqrt{n}/4\pi\epsilon_0 k_{\rm B}T$ is the interaction strength. Alternatively Kompaneets et al. [1] have presented an experimentally more relevant interaction potential, taking to account the collisions between surrounding ions and neutrals, and the external field $\mathbf{E}_0$ which is responsible for the force balance of the dust particles against gravity. The existence of $\mathbf{E}_0$ causes a downstream focusing and an anisotropic velocity distribution of ions. The in plane part of the Kompaneets potential interaction is fully described by three dimensionless parameters Γ_K, $\zeta = \lambda_K/l$ and $l\sqrt{n}$. λ_K is the field induced screening length and l is the mean free path between two collision of ions and neutrals.

We have used the mode coupling theory of the ideal glass transition (MCT) and the hypernetted chain approximation (HNC) of the structure factors to compare the glass transition properties of these two models of interactions in two dimensions. Fig. 1 shows the glass transition points of the Yukawa and the Kompaneets system. The more anisotropic the distribution of ions around the dust particles (larger l), the sharper the slope of the transition line. In Fig. 2, The red curve with squares is the glass transition curve for Kompaneets pair-potentials which have been optimally fitted to the corresponding Yukawa potential in the region $0.7 < x < 3$, by pointwise tuning of the Kompaneets κ_K and Γ_K. Our results imply that a 2D dusty plasma experiment can exhibit an apparently re-entrant liquid-glass-liquid phase sequence which is merely an artifact that arises when one attempts to describe the system with a Kompaneets-like potential in terms of the Yukawa potential parameters, and it disappears when the proper Kompaneets potential parameters are used. When screening of the interaction potential is weak, the long range behavior of both potentials suppresses the small wave vector part of the form factors at the transition shown in Fig. 3. For small κ_Y at the transition, the kernel $\mathcal{F}_q$ and the form factor f_q of the Yukawa potential, approach zero linearly in q,

$$\mathcal{F}_{q\to 0} \simeq \alpha S_{q\to 0} \simeq \alpha \frac{q}{2\pi\Gamma_Y} \tag{1}$$

which is different from the three-dimensional case [3].

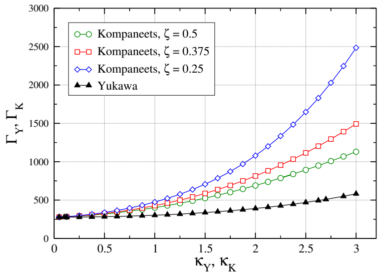

FIG. 1: Mode coupling glass transition curves in the (κ, Γ)-plane, for the Yukawa potential and three different Kompaneets potentials.

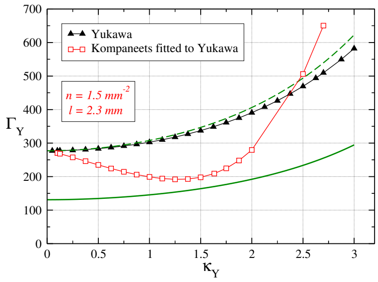

FIG. 2: Kompaneets transition fitted to the Yukawa parameters (see text). The solid green curve is the 2D Yukawa freezing line from Ref. [2].

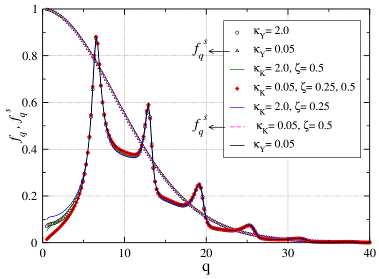

FIG. 3: The critical form factors f_q and the Lamb-Mössbauer factors f_q^s of the Kompaneets and Yukawa potentials.

---

[*] Corresponding author: `Anoosheh.Yazdi@dlr.de`

[1] R. Kompaneets, U. Konopka, A. V. Ivlev, V. Tsytovich, and G. Morfill, Phys. Plasmas **14** 052108 (2007).
[2] P. Hartmann, G. J. Kalman, Z. Donkó, and K. Kutasi, Phys. Rev. E. **72**, 026409 (2005).
[3] A. Yazdi, A. Ivlev, S. Khrapak, H. Thomas, G. E. Morfill, H. Löwen, A. Wysocki, and M. Sperl, Phys. Rev. E. **89**, 063105 (2014).

Multiple Glass-Transition Singularities in a Core-Softened Model for Glass-Forming Systems

M. Sperl,[1,*] Nicoletta Gnan,[2] Gayatri Das,[3] Francesco Sciortino,[3] and Emanuela Zaccarelli[2,3]

[1]*Institut für Materialphysik im Weltraum, Deutsches Zentrum für Luft- und Raumfahrt (DLR), 51170 Köln, Germany*
[2]*CNR-ISC Uos Sapienza, Piazzale A. Moro 2, I-00185 Roma, Italy*
[3]*Dipartimento di Fisica, Sapienza Università di Roma, Piazzale A. Moro 2, I-00185 Roma, Italy*

FIG. 1: Schematic representation of the glass-transition diagram for the square-shoulder system, adapted from [1]. For increasing shoulder width, a line of glass-glass transitions migrates from the glass regime towards the fluid, merges with the glass-transition line, and is absorbed into the glass-transition via two different higher-order glass-transitions.

Within the mode-coupling theory for ideal glass transitions (MCT), several nontrivial features have been predicted for the square-shoulder system [1]. The glass-transition diagram for such a core-softened potential, cf. Fig. 1, includes multiple reentry phenomena, a line of glass-glass transitions disconnected from the fluid regime, and two distinct scenarios with higher-order glass-transition singularities, A_3 and A_4.

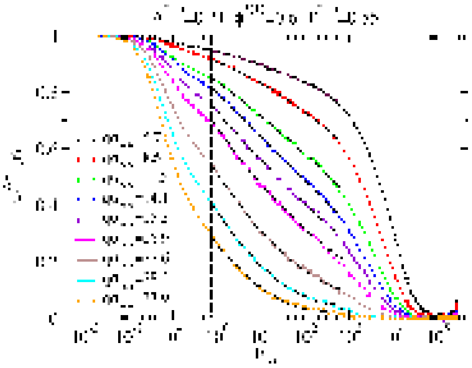

FIG. 2: Collective density correlators of the larger species in a numerical simulation of the square-shoulder system [2]. Relaxations are shown for different wave vectors.

The existence of such higher-order singularities can be detected by identifying logarithmic decay laws in the correlation functions. And indeed for the square-shoulder system logarithmic decay laws have been found in extensive numerical simualtions [2]. Figure 2 shows the coherent density correlation functions for packing fraction $\phi = 0.6$, temperature $T = 0.55$ at a shoulder width of $\Delta = 0.21$. For a variation in the wave vectors q, the relaxation exhibits the characteristic change from convex to concave behavior in the log-linear representation of the correlation functions. For an intermediate wave vector, $q\sigma_{AA} \approx 15$, the logarithmic relaxation is observed over three orders of magnitude in time.

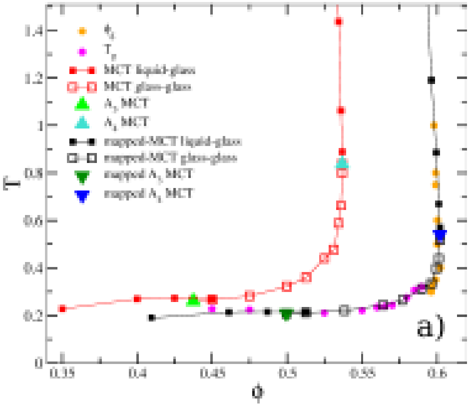

FIG. 3: Glass-transition diagram for the square-shoulder system derived from the results of the numerical simulation [2]. The theoretical predictions by MCT from [1] can be mapped into it by simple shifts along the control parameters.

By extrapolating the evolution of the dynamics, one can identify the glass transition points. Analyzing the dynamics of the correlators over a large parameter space allows for the construction of the numerical glass-transition diagram. Figure 3 shows that the glass-transition diagram obtained from numerical simulation can be mapped to the theoretical predicitions by a shift along the control parameters. The rich scenario of multiple glass-transition singularities for the square-shoulder system can hence be verified by data from the numerical simulation.

[*] Corresponding author: `matthias.sperl@dlr.de`

[1] M. Sperl, E. Zaccarelli, F. Sciortino, P. Kumar, and H. E. Stanley, Phys. Rev. Lett. **104,** 145701 (2010).
[2] N. Gnan, G. Das, M. Sperl, F. Sciortino, and E. Zaccarelli Phys. Rev. Lett. **113,** 258302 (2014).

Thinning and Thickening in Active Microrheology

Ting Wang* and Matthias Sperl

Institut für Materialphysik im Weltraum, Deutsches Zentrum für Luft- und Raumfahrt (DLR), 51170 Köln, Germany

Introduction – Active microrheology (AM) studies flow of matter under external control on the microscopic level. For instance, pulling a single particle, the probe, in a colloidal or driven granular N-particle system with constant velocity u, the external force applied to the probe F_{ex} balances the resistance from solvent drag and other particles' collision. With increasing of the pulling velocity u, the effective friction coefficient of the probe, $\gamma_{eff} := F_{ex}/u$, at first keeps constant (linear response), then starts to decrease (thinning) and finally may tend to increase (thickening). To understand the mechanism of thinning and thickening is one of the central issues of in AM.

Three Time Scales – In our previous paper [1], we found by a simple kinetic theory that inertia causes thickening. The thickening criterion is $t_{col}/t_{damp} = R\gamma_0/(um) \ll 1$, where $t_{col} = R/u$ is the time scale of probe-bath particle collision and $t_{damp} = m/\gamma_0$ is the damping time scale of a bath particle due to solvent friction γ_0. In other words, thickening happens when the frequent probe-bath collisions dominate over the solvent damping process. How about thinning? In the regime of small pulling velocity, the diffusion of bath particles may cause additional resistance. The diffusion time scale is $t_{dif} = R^2/D$ with the diffusion coefficient $D = k_BT/\gamma_0$.

An unified picture emerges that there are three time scales involved, diffusion, damping and collisions; the magnitude the pulling velocity determines which related time scale process dominates resulting in thinning and thickening behaviours. In detail, (i) when the pulling velocity of the probe is much smaller than the diffusive velocity of bath particles, the resistance of the probe mainly comes from the diffusion of bath particles, i.e. the diffusion dominated regime. (ii) As the pulling velocity is much larger than the bath particle diffusion, the diffusion is ignorable and the resistance mainly comes from the solvent, i.e. the damping dominated regime. (iii) As the pulling velocity is extremely large, resistance mainly comes from the ballistic collision with bath particles, i.e. the inertia dominated regime. Correspondingly, the crossover from diffusion to damping causes thinning, and the crossover from the damping to inertia causes thickening. The crossovers can be identified by the thinning/thickening turning points (TP) respectively, see Fig.1.

Stochastic Simulation – To demonstrate the three time scales picture, we perform a stochastic simulation. We focus on the thinning and thickening TPs. As predicted by the physics picture, the thinning TP is proportional to the diffusion coefficient $u_{t1} \propto k_BT/\gamma_0$ while the thickening TP is proportional to the solvent friction $u_{t2} \propto \gamma_0$. Let us check the temperature dependence of the TPs.

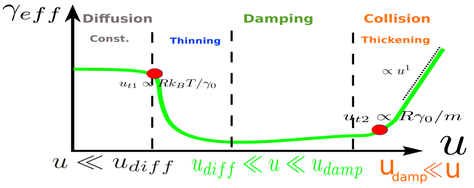

FIG. 1: Schematic Picture of Mechanism of Thinning and Thickening (three time scales and two turning points)

The simulation setup is as follows: a disk probe is pulled with a fixed velocity u, which is surrounded by bath particles in 2D. The motion of a bath particle obeys the Langevin dynamics $m\dot{\boldsymbol{v}} = -\gamma_0\boldsymbol{v} + \boldsymbol{\eta}_r$, where η_r is a Gaussian random force. Only the probe-bath particles elastic collision is considered (no interaction between bath particles). The overall collision force F_{col} to the probe is calculated and also the increasing effective friction $\Delta\gamma_{eff} := F_{col}/u$. For the particle number density $n = 0.01$, the solvent friction $\gamma_0 = 100$, and the temperatures $T = 1, 10, 100$, the results are shown in Fig.2

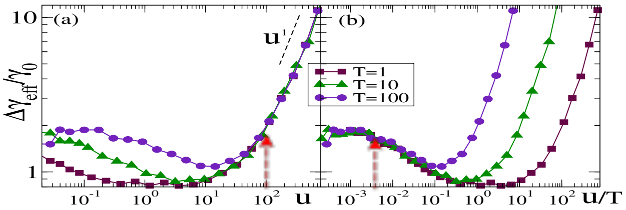

FIG. 2: (a) simulation results of the increasing friction vs. pulling velocity. The red arrow indicates the thickening TP. (b) the same data but with velocity rescaled by temperature. The red arrow indicates the thinning TP.

The results in Fig.2 show both thinning and thickening. The thickening TP is temperature independence as shown in Fig. 2 (a), and the thinning TP is temperature linear dependence as shown in (b). Both are consistent with the prediction of the three time scales picture. In addition, the scaling behaviour $\Delta\gamma_{eff} \propto u$ is also consistent with the picture.

Conclusion – We propose a three time scales picture of the mechanism of thinning and thickening, and check it by a stochastic simulation. The simulation results show both thinning and thickening, indicating that interaction between bath particles is not essential for thinning/thickening behaviours. Furthermore, the results of temperature dependence of thinning and the thickening TPs are consistent with the picture, supporting the point that mechanism of thinning/thickening is the competition of the three time scales.

---

* Corresponding author: `ting.wang@dlr.de`

[1] T. Wang, M. Grob, A. Zippelius and M. Sperl, Phys. Rev. E **89**, 042209 (2014).

Continuum Mechanics Simulations in Glass Forming Liquids

Heliana Cárdenas* and Thomas Voigtmann
Institut für Materialphysik im Weltraum, Deutsches Zentrum für Luft- und Raumfahrt (DLR), 51170 Köln, Germany

Dense liquids and glasses typically show complex non-linear non-Newtonian flow behavior [1]. Typical effects of this nonlinear glassy rheology are shear thinning and yield stresses.

A phenomenological model to discuss the non-stationary non-linear rheology by incorporating the interplay of slow structural relaxation and flow-induced rearrangements, is so-called fluidity model. It relies on a Maxwell-type constitutive equation for the stress $\boldsymbol{\sigma}(t)$,

$$\overset{\nabla}{\sigma}(t) = G_\infty D(t) - f(t)\sigma(t), \quad (1)$$

where $\boldsymbol{D}$ and G_∞ are the symmetric shear-rate tensor and the low-frequency Maxwell plateau modulus, respectively. $\overset{\nabla}{\boldsymbol{\sigma}}$ is the upper-convected derivative which takes into account the change of the tensorial stresses due to flow advection.

The fluidity $f(t)$ is a local inverse relaxation time [2, 3]. We propose a variant of existing models where the fluidity is governed by the differential equation

$$\tau_f \dot{f}(y,t) = -\left(f(y,t) - \frac{1}{\tau_M(t)}\right) + \xi^2 \nabla^2 f(y,t). \quad (2)$$

The steady-state relaxation time defined by $1/\tau_M = 1/\tau + |\dot{\gamma}|/\gamma_c$ includes shear thinning as the competition between the structural relaxation rate $1/\tau$ and the flow rate $\dot{\gamma}$ (γ_c is a dimensionless model parameter).

The effect on the dynamics of a heterogeneous fluidity value is included by using the diffusion term $\xi^2\nabla^2 f$ in Eq. (2) [2]. ξ is related to a cooperativity length that describes to what extend a fluidized region spreads along its neighbors during flow, accounting for spatial heterogeneities [3]. Moreover, we can define the fluidity diffusion coefficient as $D_f = \xi^2/\tau_f$.

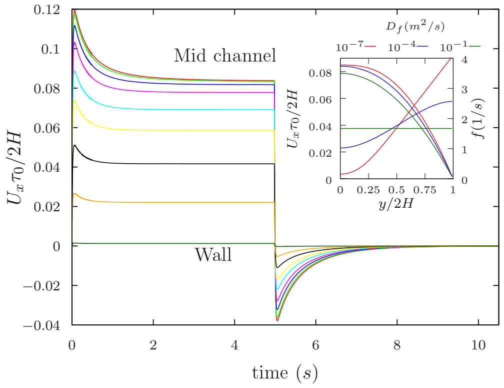

FIG. 1: Velocities centerlines at different positions of presure-driven flow in a channel. Inset: fluidity (right axis) and velocity (left axis) profiles for different D_f in steady state for half channel.

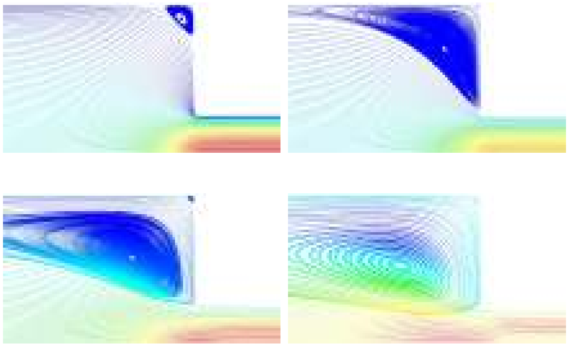

FIG. 2: Stream lines patterns and vortices found in contraction flow during cessation: top left: steady state flow; top right: immediately after the pressure is removed; bottom left: velocity starts dropping to zero and to negative values; bottom right: velocity starts increasing to zero.

A computational fluid dynamics (CFD) software based on finite volume method (FVM) is used to combine the resulting constitutive equation with the Navier-Stokes equations to describe and validate fluid behaviors described already by other methodologies. This tool allows us to study diverse geometries like pressure driven flow in planar channels, simple shear, and abrupt contractions.

For instance figure 1 shows the evolution of velocity in start-up and cessation flow at different positions in a planar channel. Fluidity and velocity profiles are in the inset for different diffusion coefficients D_f in steady state. For low diffusion coefficients ($D_f \simeq 0$) a typical non-Newtonian velocity profile is formed in the center of the channel. This effect decreases for higher D_f making the profile parabolic-like. In this case the fluidity spreads uniformly along the channel becoming almost constant.

Effects like vortex patterns found in pressure driven flows in abrupt contractions have been studied as well. Velocity stream lines in steady state and cessation for a 4:1 contraction flow develop according to Fig. 2. Higher velocities are colored with red and lower velocities with blue. The evolution of the vortex can be observed at different times during cessation showing how it moves and spreads to the center of the channel with time. Velocities in x and y-direction develop forward and backwards to form these patterns.

* Corresponding author: `heliana.cardenas@dlr.de`

[1] Th. Voigtmann, Curr. Opin. Colloid Inferf. Sci. (2014); DOI:10.1016/j.cocis.2014.11.001.
[2] G. Picard, L. Bocquet, and F. Lequeux, Phys. Rev. E **66**, 051501 (2002).
[3] J. Goyon, A. Colin, and L. Bocquet, Soft Matter **6**, 2668 (2010).

Lattice Boltzmann simulations for viscoelastic and glass-forming fluids

S. Papenkort* and Th. Voigtmann

Institut für Materialphysik im Weltraum, Deutsches Zentrum für Luft- und Raumfahrt (DLR), 51170 Köln, Germany

The rheology of complex fluids undergoing a glass transition, is highly nonlinear. The interplay between slow structural dynamics on the microscopic scale and a mesoscopic flow field gives rise to non-Newtonian flow effects. Prominent examples are shear thinning, dynamic yield and residual stresses. In confined flow geometry, the shear rates, and thereby the fluid properties, can vary considerably in space and over extremely long time spans. The modeling of such material properties thus requires a multi-scale approach combining macroscopic continuum mechanics with microscopic theory that allows to capture the pronounced temporal history effects (usually in terms of integral equations).

Starting from first principles, mode coupling theory of the glass transition (MCT) is able to provide constitutive equations that describe the history effects determining the flow of glass-forming fluids based on a microscopic description of structural-relaxation phenomena. The Lattice Boltzmann (LB) method is a modern simulation scheme to solve the Navier-Stokes equations even for complex flow geometries. We introduce a new LB model [1, 2] which is able to include memory-integral effects in fluid-mechanics simulations and provides a link between both regimes. We implement a combined LB-MCT algorithm that accounts for long-lasting temporal history (via MCT) on every lattice point in space (as treated by LB).

A simple test case is the pressure-driven channel flow. Its transient dynamics is very much affected by the non-Newtonian properties of the fluid. The dynamics of an upper-convected Maxwell (UCM) fluid can be computed analytically and can be reproduced very well by our simulation scheme, even for extreme choices of parameters. In a nonlinear extension of the UCM model, the Maxwell time depends on the local velocity gradient field to incorporate shear-thinning effects. Fig. 1 shows the stopping flow after removing the pressure gradient. To relax residual stresses, the fluid is forced to reverse flow direction and comes to an oscillatory stop, a characteristic sign of viscoelasticity. We find the transient dynamics to dependent sensitively on the channel diameter and even to undergo a qualitative change. We can trace this effect back to a competition between the time scales of structural relaxation and the ones of hydrodynamic momentum transport [2].

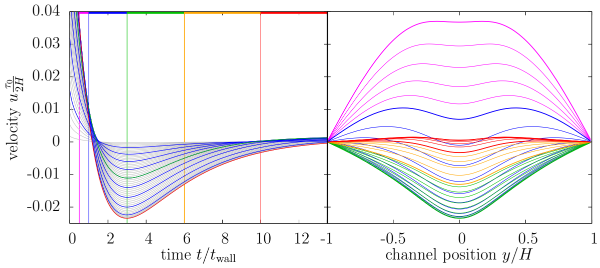

FIG. 1: Decay of the velocity profile of a nonlinear Maxwell fluid in a channel after switching off the driving pressure. Lines in the left panel correspond to various positions y across the channel (red: center, green: half-center). t_{wall} is a hydrodynamic time scale set by the channel diameter. Profiles (right panel) are shown for different times (vertical lines left).

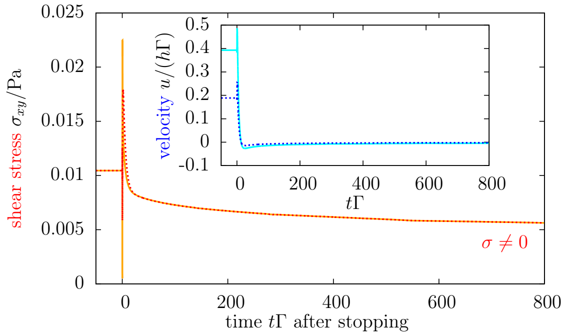

FIG. 2: Velocity (red; main panel) and shear stress (blue; inset) evolution after the cessation of simple shear flow at $t\Gamma = 0$, calculated using lattice-Boltzmann simulations combined with MCT.

A qualitative influence of the macroscopic flow geometry on the microscale properties is seen in the formation of residual stresses. The latter often arise in casting followed by quenches, and dramatically influence the material properties used in applications, i.e., for scratch-resistant smartphone covers (impressively demonstrated by exploding Prince Rupert drops [3]). As shown in Fig. 2, our combined LB-MCT algorithm is able to capture the emergence of finite residual stresses for an initially shear-molten glass, after the driving force is removed. The same algorithm demonstrates, that for the quench performed in pressure-driven channel flow, no residual stresses can remain due to the symmetry imposed by the Navier-Stokes equation and the boundary conditions. In general, the combination of a Navier-Stokes solver with a constitutive equation capturing the temporal-history dependence of a glass former allows us to study more complex flow scenarios.

---

* Corresponding author: `simon.papenkort@dlr.de`

[1] S. Papenkort and Th. Voigtmann, J. Chem. Phys. **140**, 164507 (2014).
[2] S. Papenkort and Th. Voigtmann, *in preparation*.
[3] S. Papenkort and Th. Voigtmann, student project weeks

A mode-coupling theory model to investigate the rheology of binary mixtures

M. Priya[1, *] and Th. Voigtmann[1, 2]

[1] *Institut für Materialphysik im Weltraum, Deutsches Zentrum für Luft- und Raumfahrt (DLR), 51170 Köln, Germany*
[2] *Institut für Theoretische Physik II: Weiche Materie, Heinrich Heine-Universität Düsseldorf, Universitätsstraße 1, 40225 Düsseldorf, Germany*

A theory based on mode coupling theory (MCT) of glass transition is developed to characterize the rheological properties of a colloidal suspension of particles of two kinds interacting via a hard-sphere potential. A binary colloidal glass exhibits a rich glass transition diagram as obtained by the MCT [1, 2]. MCT predicts that when particles of sufficiently different size are added at a constant volume fraction to an arrested monodisperse system, the system melts [1]. When particles with even larger size disparity are added, theory predicts multiple distinct glassy states [2]. Depending on the concentration, a "single glass" state is observed in which the smaller particles are mobile while the bigger particles are frozen. This is distinct from a "double glass" state where both kind of particles are frozen which is observed for higher volume fractions. This MCT picture is consistent with experiments where a faster relaxation is observed in systems with large size disparity at intermediate mixing.

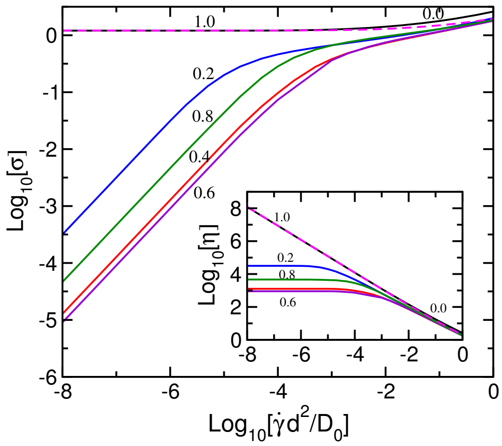

FIG. 1: Steady-state shear stress σ in response to shear rate $\dot\gamma$ (flow curves), for a binary mixture at packing fraction $\varphi = 0.518$ and size-ratio $\delta = 0.6$ for different values of relative packing fraction of the smaller particles as mentioned in the figure.Inset shows the same plot translated to viscosity.

Recently, the rheological response of binary colloidal glasses to an applied shear has been investigated extensively in experiments [3]. To understand the mechanism behind, we have developed an MCT model for binary mixtures by extending the integration through transients-mode coupling theory (ITT-MCT) model developed by Fuchs and Cates [5] for studying a one-component system. In Fig. 1, we have shown the flow behavior of a binary mixture by plotting the yield stress σ_y for a range of shear rates $\dot\gamma$ at different concentrations of the smaller particles. We observe a non-vanishing yield stress for concentrations 0 and 1 while for other concentrations the curves first show a non-Newtonian behavior and then become Newtonian at lower shear rates.

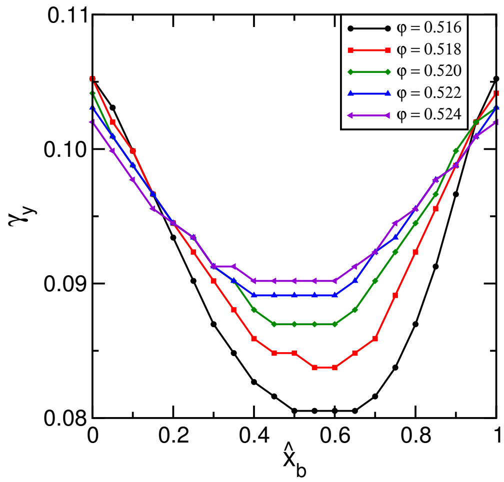

FIG. 2: Yield strain γ_y verses the relative packing fraction of smaller particles $\hat{x}_b$ for different packing fractions.

In Fig. 2, we investigate the effect of mixing on yielding behavior of the mixture at size-ratio $\delta = 0.6$ for different packing fractions. We notice that yielding occurs at 10% for lowest mixings while the yield strain lowers down for higher mixings. The effects of mixing and assymetry on rheological behavior will be investigated further in details. In a previous work [4], we investigated the rheological properties of a square-well system (SWS) by using the ITT-MCT model developed for one-component system [5]. A SWS mimics the behavior of a colloid-polymer mixture. Some recent experiments indicate that highly asymmetric binary mixtures, *i.e.*, mixtures with size-ratio $\delta \sim 0.1$, are expected to exhibit properties similar to attraction dominated colloid-polymer mixtures. Thus, the model formulated will be used to investigate highly asymmetric binary mixtures and to test the above mentioned experimental observation.

Funding from Helmholtz-Gemeinschaft (VH-NG 406) is acknowledged. M. P. is supported by DLR-DAAD fellowship No. 141.

[*] Corresponding author: `madhu.priya@dlr.de`

[1] W. Götze and Th. Voigtmann, Phys. Rev. E **67**, 021502 (2003).
[2] Th. Voigtmann, Europhys. Lett. **96**, 36006 (2011).
[3] T. Sentjabrskaja *et al.*, Soft Matter **9**, 4524 (2013);Soft Matter **10**, 6546 (2014).
[4] M. Priya and Th. Voigtmann, J. Rheol. **58**, 1163 (2014).
[5] M. Fuchs, M. E. Cates, Faraday Discuss. **123**, 267 (2003).

Analysis of residual stresses in colloidal glasses

S. Fritschi,[1] M. Fuchs,[1] and Th. Voigtmann[2]

[1]*Physik-Department, Universität Konstanz, 78457 Konstanz, Germany*
[2]*Institut für Materialphysik im Weltraum, Deutsches Zentrum für Luft- und Raumfahrt (DLR), 51170 Köln, Germany**

Amorphous solids that are produced by flowing them into shape, entailing a quench into a nonequilibrium glassy state, display residual stresses [1]. The internal stresses that build up during flow do not relax fully after removing the external flow rate, so that some part of them persists in the solid that is formed by kinetic arest in the fluid. They persist indefinitely in the ideal glass.

The appearance of such residual stresses is known empirically since centuries, and is relevant for the mechanical properties of safety glasses, smartphone glass covers, the fatigue of railway rails for high-speed trains, and even the unique properties of spider silk. A theoretical understanding of residual stresses is complicated by the fact that they are true nonequilibrium nonlinear phenomena. Mode-coupling theory has been able to give a qualitative account recently [1], based on the persistant memory of density fluctuations in the glass.

Figure 1 shows an example from simulations of a binary mixture of hard disks in two dimensions [2]. A constant shear rate $\dot\gamma$ is switched on instantaneously at $t = 0$, and switched off after a strain $\dot\gamma t = 1$ has been reached. In the figure, times have been shifted such that the origin corresponds to the cessation of flow.

After switch-on of the shear flow, the stress $\sigma(t)$ rises at first linearly, indicating an elastic regime for small strains. The steady-state value σ_{ss} under flow is reached after a strain of around 10%, after a pronounced stress overshoot. The latter feature is well known in various colloidal and metallic glasses and indicates the cross-over from reversible deformation to flow through the breaking of nearest-neighbor cages.

The relaxation of the stress $\sigma(t)$ following cessation is characterized by a nonzero plateau that remains for long times. Remarkably, this pleateau depends on the previous shear rate even for the same initial thermodynamic state of the system. This demonstrates that the appearance of residual stresses is a nonlinear-response phenomenon that is not captured by standard linear-response arguments (such as Onsager's response formalism).

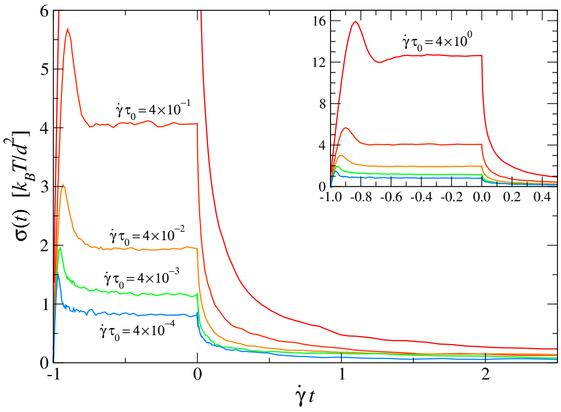

FIG. 1: Transient shear stress $\sigma(t)$ from Brownian dynamics simulations of a 2D hard-disk binary mixture at packing fraction $\varphi = 0.81$, for various shear rates as labeled. Steady shear is switched off at $t = 0$, and switched on at $-\dot\gamma t = 1$.

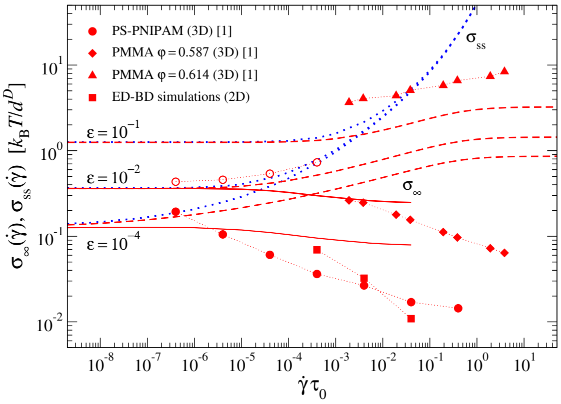

FIG. 2: Residual stress σ_∞ as a function of pre-shear rate $\dot\gamma$ (given in bare Péclet numbers $\dot\gamma\tau_0$). Solid lines: schematic model of mode-coupling theory (various distances from the glass transition ε); dashed lines: schematic model with only plastic stress relaxation. Symbols are from experiment and simulation as labeled. Dotted line: steady-state flow curve $\sigma_{\text{ss}}(\dot\gamma)$.

The dependence of this residual-stress plateau σ_∞ on the previous shear rate is shown in Fig. 2. Different symbols correspond to experiments and our simulation at various states in the glass. At low shear rates, σ_∞ approaches the steady-state value σ_{ss} attained under flow, i.e., the system is unable to relax any of the stresses imposed under slow flow. Generically, σ_∞ decreases with increasing $\dot\gamma$, although for colloidal hard spheres close to random-close packing, the opposite trend is observed in experiment (triangles in Fig. 2). A schematic model of mode-coupling theory allows to disentangle two effects: stress relaxation occurs via plastic events but also anelastically. The latter mechanism is important to understand that stronger past flow allows to relax more of the flow-induced anisotropic structure, producing a material with fewer frozen-in residual stresses.

Part of this work was supported by the Helmholtz-Gemeinschaft, Helmholtz-Hochschul-Nachwuchsgruppe VH-NG 406, and the DFG Research Unit FOR1394, project P3.

---

* Corresponding author: `thomas.voigtmann@dlr.de`

[1] M. Ballauff *et al.*, Phys. Rev. Lett. **110**, 215701 (2013).
[2] S. Fritschi, M. Fuchs, and Th. Voigtman, Soft Matter **10**, 4822 (2014).

2 Publications and Patents

2.1 Peer-Reviewed Publications

[1] S. W. Basuki, A. Bartsch, F. Yang, K. Rätzke, A. Meyer, and F. Faupel, *Decoupling of Component Diffusion in a Glass-Forming* $Zr_{46.75}Ti_{8.25}Cu_{7.5}Ni_{10}Be_{27.5}$ *Melt Far above the Liquidus Temperature*, Physical Review Letters **113**, 165901 (2014).

[2] S. Binder, P. Galenko, and D. Herlach, *The effect of fluid flow on the solidification of Ni2B from the undercooled melt*, Journal of Applied Physics **115**, 053511 (2014).

[3] P. Born, N. Rothbart, M. Sperl, and H.-W. Hübers, *Granular structure determined by terahertz scattering*, Europhysics Letters **106**, 48006 (2014).

[4] P. Born, V. Schön, S. Blum, D. Gerstner, P. Huber, and T. Kraus, *Self-Assembly of Gold Nanoparticles at the Oil-Vapor Interface: From Mono- to Multilayers*, Langmuir **30**, 13176 (2014).

[5] J. Brillo, G. Lauletta, L. Vaianella, E. Arato, E. Ricci, D. Giuranno, and R. Novakovic, *Surface Tension of Liquid Ag-Cu Binary Alloys*, ISIJ International **54**, 2115 (2014).

[6] J. Brillo and R. Schmid-Fetzer, *A model for the prediction of liquid–liquid interfacial energies*, Journal of Materials Science **49**, 3674 (2014).

[7] O. Budenkova, F. Baltaretu, S. Steinbach, L. Ratke, A. Roosz, A. Ronaföldi, J. Kovacs, A.-M. Bianchi, and Y. Fautrelle, *Modelling of Al-7wt%Si-1wt%Fe ternary alloy: application to space experiments with a rotating magnetic field*, Materials Science Forum pp. 46–51 (2014).

[8] G. Ehlen, H. Wang, and D. M. Herlach, *Concentration dependent growth velocities in undercooled Al-rich Al-Ni alloy systems*, Materials Science Forum **790**, 485 (2014).

[9] Z. Evenson, S. E. Naleway, S. Wei, O. Gross, J. J. Kruzic, I. Gallino, W. Possart, M. Stommel, and R. Busch, β*-relaxation and low-temperature aging in a Au-based bulk metallic glass: From elastic properties to atomic-scale structure*, Physical Review B **89**, 174204 (2014).

[10] S. Fritschi, M. Fuchs, and T. Voigtmann, *Mode-Coupling Analysis of Residual Stresses in Colloidal Glasses*, Soft Matter **10**, 4822 (2014).

[11] P. Galenko, M. Kolbe, D. Herlach, and M. Rettenmayr, *Kinetics of dendrite growth and dendritic fragmentation in the undercooled* $Co_{81.2}Cu_{18.8}$ *alloy's melt*, Metallurgical Research & Technology **111**, 295 (2014).

[12] A. D. Gardner, K. Richter, H. Mai, and D. Neuhaus, *Experimental Investigation of Air Jets to Control Shock-Induced Dynamic Stall*, Journal of the American Helicopter Society **59**, 1 (2014).

[13] A. D. Gardner, K. Richter, H. Mai, and D. Neuhaus, *Experimental investigation of high-pressure pulsed blowing for dynamic stall control*, CEAS Aeronautical Journal **5**, 185 (2014).

[14] D. Herlach, *Colloids as model systems for metals and alloys: a case study of crystallization*, The European Physical Journal – Special Topics **223**, 591 (2014).

[15] D. M. Herlach, *Non-Equilibrium Solidification of Undercooled Metallic Melts*, Metals **4**, 196 (2014).

[16] D. Holland-Moritz, F. Yang, J. Gegner, T. Hansen, M. Ruiz-Martin, and A. Meyer, *Structural aspects of glass-formation in Nb-Ni melts*, Journal of Applied Physics **115**, 203509 (2014).

[17] W. Hornfeck and P. Kuhn, *Octogonal symmetry in low discrepancy beta-manganese*, Acta Crystallographica Section A **70**, 441 (2014).

[18] H. Kobatake and J. Brillo, *Thermophysical properties of Cr-Fe-Ni alloys and introduction of the research in DLR*, Kinzoku (Materials science & technology) **84**, 106 (2014).

[19] H. Kobatake, J. Schmitz, and J. Brillo, *Density and Viscosity of ternary Al-Cu-Si liquid alloys*, Journal of Materials Science **49**, 3541 (2014).

[20] P. Kuhn, J. Horbach, F. Kargl, A. Meyer, and T. Voigtmann, *Diffusion and interdiffusion in binary metallic melts*, Physical Review B **90**, 024309 (2014).

[21] E. Murray, P. Born, A. Weber, and T. Kraus, *Robust, ultrasmall organosilica nanoparticles without silica shells*, Journal of Nanoparticle Research **16**, 2462 (2014).

[22] R. Novakovic and J. Brillo, *Thermodynamics, thermophysical and structural properties of liquid Fe-Cr alloys*, Journal of Molecular Liquids **200**, 153 (2014).

[23] S. Papenkort and T. Voigtmann, *Channel flow of a tensorial shear-thinning Maxwell model: Lattice Boltzmann simulations*, Journal of Chemical Physics **140**, 164507 (2014).

[24] P.-F. Paradis, T. Ishikawa, G.-W. Lee, D. Holland-Moritz, J. Brillo, W.-K. Rhim, and J. Okada, *Materials properties measurements and particle beam interactions studies using electrostatic levitation*, Materials Science and Engineering R: Reports **R76**, 1 (2014).

[25] M. Priya and T. Voigtmann, *Nonlinear rheology of dense colloidal systems with short-ranged attraction: A mode-coupling theory analysis*, Journal of Rheology **58**, 1163 (2014).

[26] A. M. Puertas and T. Voigtmann, *Microrheology of colloidal systems*, Journal of Physics: Condensed Matter **26**, 243101 (2014).

[27] J. Schmitz, J. Brillo, and I. Egry, *Surface tension of liquid Al-Cu and wetting at the Cu/Sapphire solid-liquid interface*, The European Physical Journal – Special Topics **223**, 469 (2014).

[28] J. Schmitz, I. Egry, and J. Brillo, *Anisotropy in wetting of oriented sapphire surfaces by liquid Al-Cu alloys*, Journal of Materials Science **49**, 2286 (2014).

[29] T. Voigtman, *Nonlinear glassy rheology*, Current Opinion in Colloid & Interface Science **19**, 549 (2014).

[30] H. Wang, D. M. Herlach, and R. P. Lu, *Dendrite growth in* $Cu_{50}Zr_{50}$ *glass-forming melts, thermodynamics vs. kinetics*, EPL **105**, 36001 (2014).

[31] H. Wang, F. Liu, and D. M. Herlach, *Modeling the growth kinetics of a multi-component stoichiometric compound*, Journal of Materials Science **49**, 1537 (2014).

[32] T. Wang, M. Grob, A. Zippelius, and M. Sperl, *Active microrheology of driven granular particles*, Physical Review E **89**, 042209 (2014).

[33] A. Yakymovych, Y. Plevachuk, S. Mudry, J. Brillo, H. Kobatake, and H. Ipser, *Viscosity of liquid Co-Sn alloys: thermodynamic evaluation and experiment*, Physics and Chemistry of Liquids **52**, 562 (2014).

[34] F. Yang, D. Holland-Moritz, J. Gegner, P. Heintzmann, F. Kargl, C. C. Yuan, G. Simeoni, and A. Meyer, *Atomic dynamics in binary Zr-Cu liquids*, EPL **107**, 46001 (2014).

[35] F. Yang, T. Unruh, and A. Meyer, *Coupled relaxation processes in a glass forming ZrTiNiCuBe liquid*, EPL **107**, 26001 (2014).

[36] A. Yazdi, A. Ivlev, S. Khrapak, H. Thomas, G. Morfill, H. Löwen, A. Wysocki, and M. Sperl, *Glass-transition properties of Yukawa potentials: From charged point particles to hard spheres*, Physical Review E **89**, 063105 (2014).

[37] H. Yoshida, H. Mizuno, T. Kinjo, H. Washizu, and J.-L. Barrat, *Generic transport coefficients of a confined electrolyte solution*, Physical Review E **90**, 052113 (2014).

[38] P. Yu, S. Frank-Richter, A. Börngen, and M. Sperl, *Monitoring three-dimensional packings in microgravity*, Granular Matter **16**, 165 (2014).

[39] Y. Zhang, J. Gao, H. Yasuda, M. Kolbe, and G. Wilde, *Particle size Distribution and composition in Phase-separated* $Cu_{75}Co_{25}$ *alloys under various magnetic fields*, Scripta Materialia **82**, 5 (2014).

[40] Y. Zhang, C. Simon, T. Volkmann, M. Kolbe, D. Herlach, and G. Wilde, *Nucleation transitions in undercooled* $Cu_{70}Co_{30}$ *immiscible alloy*, Applied Physics Letters **105**, 041908 (2014).

[41] G. Zimmermann, E. Schaberger-Zimmermann, S. Steinbach, and L. Ratke, *Formation of intermetallic phases in AlSi7Fe1 alloy processed onboard the ISS*, Materials Science Forum **790**, 40 (2014).

2.2 Books and Book Chapters

[1] W. A. Wakeham, I. Egry, J. Brillo, Y. Nagasaka, M. Assael, J. F. Brennecke, M. Massel, and C. Shi, *New Fluids*, in *Advances in Transport Properties of Fluids*, edited by M. Assael, A. R. H. Goodwin, V. Vesovic, and W. A. Wakeham (The Royal Society of Chemistry, 2014), vol. IX of *Experimental Thermodynamics*, pp. 173–225.

2.3 Other Publications

[1] D. M. Herlach, *Prof. Dr. Dr. h.c. Lorenz Ratke on his 65th birthday*, International Journal of Materials Research **105**, 709 (2014).

3 Presentations

3.1 Institute Seminar

Speakers that have contributed to the institute's seminar in 2014.

Prof. Ingo Steinbach, Ruhr-Universität Bochum, Germany (Jan 28, 2014): Why solidification? Why phase fields?

Prof. Reinhard Höhler, Université Pierre & Marie Curie, Paris, France (Feb 4, 2014): Multiple light scattering as a probe of dynamics in turbid soft condensed matter

Dr. Till Kranz, Universität Göttingen, Germany (Feb 13, 2014): Granular Fluids at High Density

Prof. Arno Kwade, TU Braunschweig, Germany (Feb 18, 2014): Challenges in Particle Technology

Prof. Leo Silbert, University of Illinois, USA (Feb 20, 2014): Structure of Jammed and Glassy Media

Prof. Thorsten Pöschel, Universität Erlangen, Germany (Apr 8, 2014): Vibrated Granular Matter in Microgravity

Dr. Pinaki Chaudhuri, Universität Düsseldorf, Germany (Apr 29, 2014): Onset of shear flow in confined soft glasses

Prof. Dominique Langevin, Université Paris Sud, France (May 6, 2014): Aqueous Foams

Dr. Koji Kajikawa, Japan Steel Works, Muroran, Japan (May 13, 2014): Cases of high temparature liquid property application in the Japan Steel Works, Ltd.

Stefan Frank-Richter, DLR-MP (May 20, 2014): Binary Mixtures of Granular Packings

Prof. Matthias Ballauff, Helmholtz-Zentrum Berlin, Germany (May 26, 2014): Thermosensitive Colloidal Atoms and Molecules – Do we understand the Glassy State?

Marc Engelhardt, DLR-MP (May 27, 2014): Diffusion in Ternary Metallic Alloys

Dr. Tobias Kraus, Leibniz Institute for New Materials, Saarbrücken, Germany (Jun 3, 2014): Wet Routes to New Materials

Dr. Enzo Liotti, Oxford University, UK (Jun 10, 2014): In situ studies of solidification by synchrotron X-rays radiography

Elke Sondermann, DLR-MP (Jun 12, 2014): Massediffusion in flüssigem Al-Ni untersucht mittels Röntgenradiographie auf MAPHEUS 4

David Heuskin, DLR-MP (Jun 17, 2014): Messung von Diffusionskoeffizienten in hochschmelzenden metallischen Flüssigkeiten mit Scherzellentechnik

Dr. Fatollah Varnik, Ruhr-Universität Bochum, Germany (Jun 24, 2014): Signature of elasticity in plasic deformation of amorphous solids: Insights from molecular dynamics simulations

Pascal Heintzmann, DLR-MP (Jul 3, 2014): Thermodynamic Properties of Zirconium Alloys

Dr. Tom Rother, DLR Neustrelitz (Jul 8, 2014): Radiative Transfer for Atmospheric Particles

Dr. Reinhard Miller, MPI für Kolloid- und Grenzflächenforschung Potsdam, Germany (Jul 15, 2014): Emulsions in Microgravity

Prof. Eun Soo Park, Seoul National University, Korea (Sep 9, 2014): Formation of Bulk Metallic Glasses and Their Composites from Undercooled Melts

Prof. Swantje Bargmann, TU Hamburg Harburg, Germany (Oct 28, 2014): Continuum Materials Modeling

Prof. Stephan Schlemmer, Universität Köln, Germany (Nov 4, 2014): Laboratory Astrochemistry

Dr. Burkhard Dünweg, MPI für Polymerforschung, Mainz, Germany (Nov 10, 2014): Lattice Boltzman Simulations

Prof. Tanja Schilling, Université du Luxembourg (Nov 25, 2014): Crystallization in colloidal model systems

Prof. Michael Dreyer, ZARM Bremen, Germany (Dec 2, 2014): Capillary Channel Flow

3.2 Talks given by institute members

Invited talks of institute members given at international conferences, symposia, and seminars.

Granular Stress-Birefringence in Three Dimensions
S. Frank-Richter; Twente University, The Netherlands, June 2014.

Containerless Processing in the Study of Metastable Solids from Undercooled Melts
D. M. Herlach; 3rd International Conference on Materials Engineering for Advanced Technologies, Brisbane, Australia, January 2014.

Rapid solidification of undercooled melts
D. M. Herlach; plenary lecture, 4th International Conference on Advances in Solidification Processes (ICASP), Beaumont Estate, Old Windsor, UK, July 2014.

Dendrite growth in undercooled melts of intermetallic compounds
D. M. Herlach; key note lecture, 15th International Conference on Rapidly Quenched and Metastable Materials, Shanghai, China, August 2014.

Nucleation and Dendrite growth in undercooled melts of metals and alloys
D. M. Herlach; plenary lecture, 3rd iMat Microstructure and Materials Science Conference, Teheran, Iran, November 2014.

Undercooled melts: ordering, nucleation, dendrite growth
D. M. Herlach; Workshop Directional Nucleation and Growth of Molecular Crystals, International Solvay Institutes of Physics and Chemistry, Brussels, Belgium, November 2014.

Structure and Dynamics in Undercooled Melts
D. Holland-Moritz; Key Lab of Electromagnetic Processing of Materials, Northeastern University Shenyang, China, August 2018.

Nahordnung in binären glasbildenden Legierungsschmelzen
D. Holland-Moritz; Deutsche Tagung für Forschung mit Synchrotronstrahlung, Neutronen und Ionenstrahlen an Großgeräten, Bonn, September 2014.

Interdiffusion in liquid metals measured in-situ
F. Kargl; DIMAT 2014, Münster, August 2014.

Thermophysical Properties of liquid and supercooled CaO-Al2O3
F. Kargl; ISIJ Conference, Nagoya, Japan, September 2014.

Dendrite Growth in Undercooled Fe-B Alloy Melts
C. Karrasch; Northwestern Polytechnical University Xi'An, China, September 2014.

Dendrite Growth in Undercooled Fe-B Alloy Melts
C. Karrasch; Key Lab of Electromagnetic Processing of Materials, Northeastern University Shenyang, Chine, September 2014.

Surface tension measurement of liquid Al-Si alloys
H. Kobatake; European Conference on Thermophysical Properties, Porto, Portugal, September 2014.

Thermophysical properties of liquid alloys under oxygen influence
H. Kobatake; Asian Microgravity Symposium, Seoul, Korea, October 2014.

The Measurement of Self-Diffusion Coefficients in Liquid Metals with Quasielastic Neutron Scattering
A. Meyer; keynote lecture, QENS/WINS 2014 Conference, Autrans, France, May 2014.

Diffusion of mass in liquid BMGs using levitation in combination with QENS
A. Meyer; 27th Bulk Metallic Glass Conference BMG10, Shanghai, China, June 2014.

Materials Physics in Space – Tranpsort of Mass in Liquid Metals and Alloys
A. Meyer; LAMA Kolloquium, Universität Gießen, November 2014.

Self- and Interdiffusion in Liquid Alloys
A. Meyer; Materialphysikalisches Kolloquium, Universität Münster, December 2014.

Elastic Heterogeneities in Granular Solids
H. Mizuno; Glastag Augsburg, Germany, October 2014.

Lattice Boltzmann Simulation of Complex Fluids in Microchannels
S. Papenkort; Condensed Matter Conference CMD25, Paris, August 2014.

Forschen auf der Raumstation: Wissenschaft ohne Oben und Unten
M. Sperl; Odysseum Cologne, March 2014.

Granular Matter in Space
M. Sperl; Sino-German Workshop, Beijing, China, May 2014.

Higher-Order Singularities at the Glass Transition and Random-Close Packing
M. Sperl; keynote lecture, Conference on Packing and Jamming of Particulate Systems, Erlangen, Germany, September 2014.

Reach out beyond Gravity – Soft and Granular Matter in Space
M. Sperl; T-MAPPP Summer School, Imperial College, London, UK, September 2014.

Glassy Dynamics in a Cup of Coffee: Higher-Order Glass-Transition Singularities
M. Sperl; Kavli Institute for Theoretical Physics, University of California, Santa Barbara, USA, October 2014.

Materials Physics in Space: Dynamics and Rheology in Granular Matter
M. Sperl; LAMA Colloquium, Universitaet Giessen, Germany, November 2014.

The Flow of Glass-Forming Fluids
Th. Voigtmann; Physics Colloquium, Université du Fribourg, Switzerland, February 2014.

The Flow of Dense Fluids
Th. Voigtmann; Physics Colloquium, Université du Luxembourg, March 2014.

Combining Microscopic Theory with Macroscopic Simulation
Th. Voigtmann; Annual European Congress on Rheology, Karlsruhe, April 2014.

Nonlinear Rheology of Attractive Glasses
Th. Voigtmann; Meeting of the Hellenic Rheological Society, Heraklion, Greece, July 2014.

Nonlinear Glassy Rheology
Th. Voigtmann; Symposium on Chemical Engineering of Colloidal Suspensions, Helmholtz-Zentrum Berlin, October 2014.

Nonlinear Glassy Rheology
Th. Voigtmann; keynote lecture, 1st Advanced Workshop on Out-of-Equilibrium Matter, San Luis Potosí, Mexico, December 2014.

Flowing Glasses, Micro & Macro
Th. Voigtmann; 1st Advanced Workshop on Out-of-Equilibrium Matter, San Luis Potosí, Mexico, December 2014.

Nonlinear Glassy Rheology
Th. Voigtmann; COST Workshop Flowing Matter, Lisbon, Portugal, December 2014.

Metastable Phase Formation in Undercooled Fe-Co Alloy Melts
T. Volkmann; 4th International Conference on Advances in Solidification Processes (ICASP), Beaumont Estate, Old Windsor, UK, July 2014.

3.3 Doktorandenrunde

The PhD students of the institute organize a seminar as part of their graduate program.

Marc Engelhardt (Apr 11, 2014): Messung von Diffusionskoeffizienten in ternären AlCuAg Legierungen und deren Subsystemen

Elke Sondermann (May 22, 2014): Interdiffusion von Al-Ni-Schmelzen

Pascal Heintzmann (Jun 18, 2014): Thermodynamische Eigenschaften von Zirkon-Basislegierungen

Tobias Kordel, VDEh-Betriebsforschungsinstitut (Sep 17, 2014): Messtechnik für die Stahlerzeugung

4 Lecture Courses and Lectures

Einführung in die Metallphysik
Ruhr-Universität Bochum, 2 SWS (WS 2013/14)
D. Holland-Moritz

Einführung in die Röntgen- und Neutronenstreuung
Ruhr-Universität Bochum, 2 SWS (SS 2014)
D. Holland-Moritz

Physik für Ingenieure
Ruhr-Universität Bochum, 2 SWS (WS 2014/15)

Einführung in die Metallphysik
Ruhr-Universität Bochum, 2 SWS (WS 2014/15)
D. Holland-Moritz

Heterogene Gleichgewichte
RWTH Aachen, 2 SWS (WS 2014/15)
F. Kargl, J. Brillo

Classical Field Theory
Heinrich Heine-Universität Düsseldorf, 4 SWS (WS 2014/15)
Th. Voigtmann

Oberseminar Materialphysik im Weltraum
Ruhr-Universität Bochum, 2 SWS (WS 2014/15)
A. Meyer

5 Graduations

Bachelor

- Dominique Jonas Daab, *Entwicklung eines Mapheus-Forschungsraketenmoduls zum Betrieb eines Ofens zur Bestimmung der Wärmeleitfähigkeit flüssiger metallischer Legierungen mit Hilfe der konzentrischen Zylindermethode*, FH Aachen, October 2014.
- Melissa Lückerath, *Untersuchung der Zusammensetzung und Eigenschaften spannungsoptischer Materialien*, FH Rhein-Sieg, March 2014.
- Steffen Pappert, *Optimierung eines Ofens zur Messung der Wärmeleitfähigkeit von Schmelzen mittels der stationär konzentrischen Zylindermethode*, FH Aachen, March 2014.
- Liam Redmond, *Granulare Lichtstreuung in einer Bodenreferenzmessung für Experimente unter Schwerelosigkeit*, FH Aachen, August 2014.
- Marcus Reinartz, *Untersuchung zur Nichtgleichgewichtserstarrung einer intermetallischen Phase Fe2B mit Übergitterstruktur*, Universität zu Köln, July 2014.
- Johannes Schmitz, *Optimierung und Test eines Lichtstreuexperimentes für Kurzzeitmessungen unter Mikrogravitationsbedingungen*, August 2014.
- Sebastian Subatzus, *Versuchsaufbau zur Schallmessung an Granulaten im Labor und für den Fallturm*, FH Aachen, July 2014.
- Duong Tran, *Design, Entwicklung und Verifizierung des MeGrMa Moduls*, FH Aachen, September 2014.

Diploma and Master

- Boris Eberhardt, *Microrheology in a Driven Two-Dimensional Granular System*, Universität zu Köln, Diploma thesis, December 2014.
- Michael Balter, *Entwicklung eines neuen Ofenkonzepts, für die Durchführung von Experimenten, zur gerichteten Erstarrung von Metalllegierungen unter Mikrogravitationsbedingungen*, FH Köln, December 2014.

PhD Theses

- Marc Engelhardt, *Messung von Diffusionskoeffizienten in ternären AlCuAg Legierungen und deren Subsytemen*, RWTH Aachen, August 2014.
- Stefan Frank-Richter, *Ausbau der Methode der granularen Spannungsoptik in drei Dimensionen für Laboruntersuchungen und für die Implementierung auf der Raumstation*, July 2014.
- Pascal Heintzmann, *Untersuchung thermophysikalischer Eigenschaften von Metallschmelzen mittels Röntgenradiographie, sowie elektrostatischer und elektromagnetischer Levitation*, December 2014.

6 Awards

- D. M. Herlach, member of Arbeitskreis Metall- und Materialphysik (DPG, DGM, VDEh)
- D. M. Herlach, member of DPG Vorstandsrat
- D. M. Herlach, deputy of DLR at BV MatWerk
- D. Holland-Moritz, nomination as Concurrent Professor, Northeastern University Shenyang, China
- F. Kargl, member college 6, Institut Laue Langevin (ILL), France
- A. Meyer, nominated chairman of the Science Advisory Council of the European Spallation Source ESS, Sweden.

7 Fellows

- Georg Ehlen: Ruhr-Universität Bochum (2011–2014)
- Dr. Zachary Evenson: DLR-DAAD postdoctoral fellow (2013–2015)
- Dr. Somayeh Farhadi: DLR-DAAD postdoctoral fellow (2013/14)
- Ran Jin: Sino-German cooperation (2014)
- Shitong Liu: DLR-DAAD fellow (2014)
- Dr. Hideyuki Mizuno: DLR-DAAD postdoctoral fellow (2014/15)
- Christian Karrasch: Ruhr-Universität Bochum
- Raphael Kobold: Ruhr-Universität Bochum
- Stefanie Koch: Ruhr-Universität Bochum
- Dr. Vincent Krakoviack (ENS Lyon, France): DFG Research Unit long-term guest (2014)
- Chiara Maran: Master student, University of Genua (2014/15)
- Alexandre Meurisse: ESA cooperation
- Dr. Hailong Peng: DLR-DAAD postdoctoral fellow (2013–2015)
- Pierre Pichon: doctoral fellow (2012–15)
- Dr. Madhu Priya: DLR-DAAD postdoctoral fellow (2013–2015)
- Danilo Rosselo: Master student, University of Genua (2014/15)
- Chae Woo Ryu: DLR-DAAD fellow (2014/15)
- Dr. Leonardo Silbert (Southern Illinois University, USA): DFG Research Unit long-term guest (2014)
- Reeti Singh: Ruhr-Universität Bochum
- Anoosheh Yazdi: Heinrich-Heine Universität Düsseldorf
- Dr. Chen Chen Yuan: DLR-DAAD postdoctoral fellow (2012–14)
- Dr. Qiang Wang: Sino-German cooperation (2014)
- Ting Wang: DLR-DAAD fellow (2012–2015)
- Nannan Zhang: DLR-DAAD fellow (2014/15)

8 Events and Campaigns

- EML Facility Checkout Experiment (FCE) 1.0, onboard the International Space Station (ISS).
- Drop Tower, Bremen, January 2014: granular matter experiments.
- 24th DLR Parabolic Flight campaign, February 2014: X-RISE, ESL, and TEMPUS experiments.
- Drop Tower, Bremen, April 2014: granular sound experimnt.
- Drop Tower, Bremen, June 2014: granular light scattering.
- Measurement campaign at European Synchrotron Radiation Facility (ESRF), October 2014: High-Resolution Diffraction Topography.
- 25th DLR Parabolic Flight campaign, October 2014: TEMPUS experiment.
- BESSY II, THz beamline, Berlin, October 2014: THz spectroscopy in granular matter.
- Drop Tower campaign, Bremen, November 2014: ESL experiment.
- Institute Lauge Langevin (ILL), Dezember 2014: Neutron scattering on electrostatically levitated melts.
- Frequent measurement campaigns at Forschungsneutronenquelle Heinz-Maier-Leibnitz (FRM II), Garching, TU München: Neutron time-of-flight spectrometer ToF-ToF and neutron radiography beamline ANTARES.
- Frequent measurement campaigns at Institut Lauge-Langevin (ILL), Grenoble, France: High flux neutron diffractometer D20, neutron time-focussing time-of-flight spectrometer IN6, and small momentum transfer diffractometer D16.

9 Workshops organized by the institute

Focus Session: Slow Dynamics in Glasses and Granular Matter (DPG-Tagung, Dresden, April 3–4, 2014)

M. Sperl from the Institute of Materials Physics in Space co-organized a focus session at the Spring Meeting of the German Physical Society (DPG), section Dynamics and Statistical Physics.

570. WE-Heraeus-Seminar "Nonlinear Response in Complex Systems and Nonequilibrium Liquids" (DLR-MP, September 1–5, 2014)

This workshop focused on nonlinear response phenomena, specifically in nonequilibrium liquids complex materials. In 19 invited lectures, key speakers (bold face below) gave an overview over recent developments in topics including stochastic processes far from equilibrium, nonlinear rheology of dense fluids and amorphous solids, experimental developments and computer simulations techniques for colloidal suspensions, granular matter, active-particle systems and other classical driven many-particle systems. These overview lectures were rounded off by contributed talks and lively poster sessions.

The workshop was funded by the Wilhelm und Else Heraeus-Stiftung, the most important private institution funding physics in Germany, supported by the DFG Research Unit FOR1394, and organized by Th. Voigtmann and the Institute of Materials Physics in Space.

J.-L. Barrat, U Grenoble, France: From heterogeneous elasticity to plasticity mechanisms in disordered systems

M. E. Cates, U Edinburgh, UK: Frictional Contacts and Shear Thickening in non-Brownian Suspensions

T. Franosch, U Innsbruck, Austria: Exact Nonlinear Response Theory in the Driven Lattice Lorentz Gas

R. Benzi, U Roma Tor Vergata, Italy: From liquid to solid: soft glassy dynamics at the jamming transition

D. Evans, Australian National University: Dissipation and the Foundations of Classical Statistical Thermodynamics

M. Fuchs, U Konstanz, Germany: Higher harmonics generation in glasses under large amplitude oscillatory perturbation

J. F. Brady, California Institute of Technology, USA: Colloidal dispersion sheared at constant pressure

W. Schirmacher, U Mainz, Germany: Theory of heterogeneous viscoelasticity

P. Harrowell, U Sydney, Australia: Elasticity and Disorder: Calculating the Shear Modulus in Viscoelastic Liquids and Glasses

M. Falk, Johns-Hopkins-University Baltimore, USA: Relating molecular dynamics simulations to the statistical mechanics of localization and failure in amorphous solids

J. Vermant, ETH Zürich, Switzerland: Superposition Flows to Investigate Nonlinear Rheology

E. Weeks, Emory University Atlanta, USA: Stresses and Rearrangements in Flowing Emulsions

S. Fielding, U Durham, UK: Flow instabilities in soft glassy materials

S. Mandal, U Innsbruck, Austria: Signature of elasticity in supercooled hard sphere liquids under shear

A. Zaccone, TU München, Germany: Direct relation between microstructure and thermodynamics of sheared colloidal glass

A. Zippelius, U Göttingen, Germany: Dense Granular Flow

K. Suzuki, Canon Inc., Japan: Theory of Dense Sheared Granular Flows

K. Saitoh, U Twente, The Netherlands: Non-affine response and stochastics of overlaps in two-dimensional jammed soft particles

K. Kroy, U Leipzig, Germany: Inelastic Mechanics of Polymer Networks and Cells

C. Bechinger, U Stuttgart, Germany: Gravitaxis and collective phenomena of active Brownian particles

T. Schilling, U Luxembourg: Crystallization in colloidal model systems

F. Ladieu, CEA Paris, France: A new control parameter for the glass transition of Glycerol

M. Krüger, MPI for Intelligent Systems, Stuttgart, Germany: Theory of driven colloidal suspensions in confinement

C. Schroer, U Münster, Germany: Understanding active and nonlinear microrheology on supercooled liquids in terms of properties of the underlying Potential Energy Landscape

I. Pagonabarraga, U Barcelona, Spain: Mesoscopic moeling of active suspensions: Collective response and emergent structures

E. Del Gado, ETH Zürich, Switzerland: Densification and gelation of calcium-silicate-hydrates during cement hydration

Frontiers in Solidification Research – Critical Issues and Future Directions in Solidification Science (DLR-MP, September 29–30, 2014)

This workshop was organized by D. Holland-Moritz and S. Steinbach in honor of Prof. Dr. Dr. h. c. Lorenz Ratke and Prof. Dr. Dieter Herlach in order to celebrate their important scientific contributions to the field of materials physics and especially solidification research, which span several decades. The following invited lectures were scheduled motivating extensive panel discussions in order to identify critical issues and future directions at the forefront of solidification science:

Frans Spaepen, Harvard SEAS, Cambridge, USA: Modeling phase transformations with colloids

Lindsay A. Greer, University of Cambridge, UK: Fast and slow crystallization on glass-forming liquids

Reiner Kirchheim, Universität Göttingen, Germany: Probes for a structural characterization of melts solidified as a glass

Jürgen Eckert, IFW Dresden, Germany: Tailoring structure formation and properties of metastable alloys and composites

Laszlo Granasy, Wigner Research Centre for Physics, Budapest, Hungary: Phase-field modeling of polycrystalline solidification

Peter W. Voorhees, Northwestern University, Evanston, USA: Solidification in 4D

Markus Rettenmayr, Universität Jena, Germany: Steep gradients: Directional solidification, coarsening, droplets, phase separation and more

Christoph Beckermann, University of Iowa, USA: Concurrent growth and coarsening of dendrites

Ulrike Hecht, ACCESS e.V., Aachen, Germany: Crystallographic aspects of eutectic pattern formation

Zhongyun Fan, Brunel University, UK: Recent advances in the understanding of heterogeneous nucleation

Irina Smirnova, TU Hamburg-Harburg, Germany: Particle formation on and in the aerogel

Jacques Lacaze, CIRIMAT, Toulouse, France: Rosettes

Andreas Ludwig, Montanuniversität Leoben, Austria: Reproducible occurrence of meandering flow regimes during dendritic solidification

Yves Fautrelle, SIMAP, Grenoble, France: Solidification influenced by thermo-electric effect

Douglas M. Matson, Tufts University, Medford, USA: Influence of convection on metastable transformations

Hideyuki Yasuda, Kyoto University, Japan: Remelting of primary dendrite in Cu-Fe alloys – In-situ X-ray imaging

Charles-André Gandin, Centre for Material Forming, Sophia Antipolis, France: Multiscale modeling of solidification structures and segregations

Taketoshi Hibiya, Keio University, Tokyo, Japan: Molten Silicon and Microgravity

Kenneth F. Kelton, Washington University, St. Louis, USA: Correlations of structural ordering in supercooled metallic liquids with fragility and crystal nucleation

Gerhard Wilde, Westfälische Wilhelms-Universität Münster, Germany: Quantitative determination of nucleation rates at high liquid undercooling

Jianrong Gao, Northeastern University, Shenyang, China: Competitive growth and the coupled zone in undercooled Ni-Sn alloys

Ivan Egry: A short history of microgravity levitation

10 Third-Party Funding

European Space Agency (ESA) – AO 1999, selected flight experiments

Microstructure formation in casting of technical alloys under diffusive and magnetically controlled convective conditions (MICAST)
L. Ratke, coordinator; G. Müller (D); Y. Fautrelle (F); M. D. Dupony (F); A. Roosz (HUN); G. Zimmermann (D); J. Lacaze (F)
rated *excellent*

Metastable Solidification of Composites: Novel Peritectic Structures and In-Situ Composites (METCOMP)
M. Kolbe, coordinator; G. Eggeler (D); L. Granaszy (HUN); **D. M. Herlach**; A. Ludwig (A); M. Rappaz (CH)
rated *excellent*

High Precision Thermophysical Property Data of Liquid Metals for Modelling of Industrial Solidification Processes (THERMOLAB)
H. J. Fecht, coordinator (D); L. Battezzati (I); **J. Brillo**; A. Passerone (I); E. Ricci (I); S. Seetharaman (S); R. Aune (S); J. Etay (F)
rated *outstanding*

Undercooling and Demixing of Copper-Based Alloys (COOLCOP)
J. Brillo, coordinator; **M. Kolbe**; D. Chatain (F); L. Battezzati (I); A. Serneels (B); L. Tikana (D)
rated *very good*

Study and modelling of nucleation and phase selection phenomena in undercooled melts: Application to hard magnetic alloys of industrial relevance (MAGNEPHASE)
W. Löser, coordinator (D); L. Granasy (HUN); R. Hermann (D); **D. Holland-Moritz**; **T. Volkmann**; J. Fransaer (B); rated *very good*

Non-Equilibrium Solidification, Modelling for Microstructure Engineering of Industrial Alloys (NEQUISOL)
D. M. Herlach, coordinator; C.-A. Gandin (F); A. García-Escorial (E); H. Henein (CDN)
rated *excellent*

Solidification Morphologies of Monotectic Alloys (MONOPHAS)
L. Ratke, coordinator; B. Tonn (D); A. Ludwig (A); R. Mathiesen (N); J. Agren (S); L. Granasy (H)
rated *excellent*

Solidification along a Eutectic Path in Ternary Alloys (SETA)
S. Rex, coordinator (D); L. Froyen (B); G. Faivre (F); H. Nguyen-Thi (F); **L. Ratke**
rated *excellent*

Thermophysical Properties of Liquid Metals for Industrial Process Design (ThermoProp)
H.-J. Fecht, coordinator (D); R. Wunderlich (D); L. Battezzati (I); **J. Brillo**; J. Etay (F); E. Ricci (I); S. Seetharaman (S)
consolidation of ESA MAP project AO 1999, 2004, and 2009 – rated *outstanding*

European Space Agency (ESA) – AO 2000, selected flight experiments

Investigations of thermophysical properties of Si in the melt and in the undercooled state under microgravity conditions (SEMITHERM)
K. Samwer, coordinator (D): B. Damaschke (D); **I. Egry**; **G. Lohöfer**; E. Ricci (I); E. Arato (I); T. Hibiya (JPN); W. von Ammon (D); T. Tsukuda (JPN); T. Fuhiwara (JPN)
rated *very good*

Magnetohydro-dynamics of levitated drops
R. Wunderlich, coordinator (D); G. Gerbeth (D); **I. Egry**; J. Priede (LV); J. Etay (F); Y. Fautrelle (F)
rated *very good*

European Space Agency (ESA) – AO 2004, selected flight experiments

In-situ X-ray Monitoring of Advanced Metallurgical Processes under Microgravity and Terrestrial Conditions (XRMON)
R. H. Mathiesen, coordinator (N); G. Zimmermann (D): H. Nguyen-Thi (F); L. Froyen (F); **M. Kolbe/F. Kargl**; C.-A. Gandin (F); D. Browne (IRL); F. García-Moreno (D)
rated *excellent*

Chill Cooling for the Electro-Magnetic Levitator in Relation with Continuous Casting of Steel (CCEMLCC)
C.-A. Gandin, coordinator (F); **D. M. Herlach**; **T. Volkmann**; V. Uhlenwinkel, H. Henein, D. Juul Jensen (DK); M. Kallio, F. Costes, M. Bobadilla
rated *excellent*

Non-equilibrium multiphase transformations: eutectic solidification, spinoidal decomposition and glass formation (MAGNEPHASE)
P. Galenko, coordinator; **D. M. Herlach**; R. Parfeniev (RUS); B. Melekh (RUS); M. Volkov (RUS); A. Ivanov (RUS)
rated *excellent*

Electrical Resistivity measurements of high temperature metallic melts (RESISTIVITY)
G. Lohöfer, coordinator; G. Pottlacher (A)
rated *excellent*

European Space Agency (ESA) – AO 2009, selected flight experiments

Thermophysical properties of liquid metallic alloys – modelling of industrial solidification processes and development of advanced products (THERMOLAB – ISS)
H.-J. Fecht, coordinator (D); L. Battezzati (I);
J. Brillo; A. Dommann (CH); U. Erb (CDN);
J. Etay (F); H. Fukuyama (JPN); T. Hibiya (JPN);
R. Hyers (USA); T. Ishikawa (JPN); J. Z. Jiang (CHN);
K. Kelton (USA); G. W. Lee (ROK); W. Lojkowski (PL);
I. Manna (IND); D. Matson (USA); S. Ozawa (JPN);
K. Pericleous (UK); E. Ricci (I); S. Seetharaman (S);
T. Tanaka (JPN); R. Valiev (RUS); M. Watanabe (JPN);
R. Wunderlich (D)
rated *outstanding*

Thermophysical properties and solidification behaviour of undercooled Ti-Zr-Ni liquids showing an icosahedral short-range order (ICOPROSOL)
D. Holland-Moritz, coordinator; R. Hyers (USA);
K. Kelton (USA); **G. Lohöfer**
rated *excellent*

Gravity dependence of CET in peritectic TiAl alloys (GRADECET)
U. Hecht, coordinator (D); D. Daloz (F);
L. Gránásy (HUN); A. Griesche (D); J. Lapin (SK);
S. McFadden (IRL); **A. Meyer**; M. Rebow (PL);
L. Sturz (D); G. Tegze (HUN); M. Zaloznik (F)
rated *excellent*

Thermophysical properties of liquid alloys under oxygen influence (OXYTHERM)
J. Brillo, coordinator; E. Arato (I); H. Fritze (D);
H. Fujii (JPN); L. Hennet (F); G. Kaptay (HUN);
R. Novakovic (I); S. Ozawa (JPN); E. Ricci (I);
M. Watanabe (JPN)
rated *excellent*

Peritectic alloy rapid solidification with electromagnetic convection (PARSEC)
T. Volkmann, coordinator; J. Fransaer (B);
R. Hyers (USA); M. Krivilev (RUS); W. Löser (D);
D. Matson (USA); K. Pericleous (UK)
rated *excellent*

Liquid phase separation in metallic alloys (LIPHASE)
M. Kolbe, coordinator; L. Battezzati (I); **J. Brillo**;
D. Chatain (F); S. Curiotto (F); J. Gao (CHN);
H. Yasuda (JPN)
rated *excellent*

Compaction and Sound Transmission in Dense Granular Media (COMPGRAN)
M. Sperl, coordinator; R. Behringer (USA);
E. Clement (F); S. Luding (NL); M. Schroeter (D)
rated *excellent*

Influence of diffusive and convective mass transport on microstructure formation in Al-based alloys (DIFFSOL)
A. Griesche, coordinator (D); H. Emmrich (D);
J. Horbach; G. Kaptay (HUN); **A. Meyer**;
B. Nestler (D); H. Nguyen-Thi (F); Y. Fautrelle (F);
X. Ruiz (E); Z. Saghir (CDN); V. M. Shevtsova (B);
R. Siquieri (D); **T. Voigtmann**; G. Zimmermann (D)
rated *very good*

Non-equilibrium solidification, modelling for microstructure engineering of industrial alloys (NEQUISOL III)
D. M. Herlach, coordinator; U. Fritsching (D);
C.-A. Gandin (F); H. Henein (CDN);
V. Uhlenwinkel (D)
rated *very good*

Liquid phase diffusion in semiconductors (LIPIDIS)
S. Dost, coordinator (CDN); B. Lent (CDN);
T. Masaki (JPN); **A. Meyer**; **F. Kargl**; B. Nestler (D);
Z. Saghir (CDN); A. Senchenkov (RUS);
H. Struchtrup (CDN); D. Vizman (ROM); A. Croll (D);
E. Dieguez (E); T. Duffar (F); A. Egorov (RUS)
rated *very good*

Gravitational effects on heat and mass transport phenomena in directional solidification of upgraded metallurgical silicon for photovoltaic applications (SISSI)
T. Duffar, coordinator (F); J. Friedrich,
coordinator (D); J. Baruchel (F); M. Bellmann (N):
S. Binetti (I); T. Carlberg (S); A. Croll (D);
J. Derby (USA); E. Dieguez (E); S. Dost (CDN);
F. Dupret (B); H. Emmerich (D); A.-J. Faber (NL);
C.-A. Gandin (F); J.-P. Garandet (F); M. Gonik (RUS);
A. Meyer; **F. Kargl**; K. Kakimoto (JPN);
N. Mangelinck (F); W. Miller (D); B. Nestler (D)
rated *outstanding*

ESA Topical Teams

Atomic Transport in Liquids and Semiconductors (ATLAS)
A. Griesche, coordinator (D); **A. Meyer**;
J.-P. Garandet (F); Z. Saghir (CDN); W. Miller (D);
W. Wołczyński (PL); A. Mialdun, D. Melnikov,
I. Ryzhkov, V. Shevtsova, S. Van Vaerenbergh (B);
J. Agren (S); J. Friedrich (D); F. Faupel (D);
H. Emmerich (D); B. Nestler (D); G. Wilde (D)

Solidification of Containerless Undercooled Melts SOL–EML
D. M. Herlach (coordinator), **P. Galenko,**
D. Holland-Moritz, M .Kolbe, T. Volkmann;
J. Fransaer (B); G. Phanikumar (IND);
Ch.-A. Gandin (F); J. Gao, L. Granasy (HUN);
H. Henein (CDN); R. W. Hyers (USA);
K. F. Kelton (USA); W. Löser (D); D. M. Matson,

T. Okutani (JPN): K. Pericleous (UK);
M. P. Volkov (RUS); H. Yasuda (JPN)

Space Grains
S. Aumaître (F); R. Behringer (USA); M. Berhanu (F); E. Clément (F); J. Crassous (F); D. Durian (USA); P. Evesque (F); E. Falcon (F); S. Fauve (F); A. Garcimartin (E); Y. Garrabos (F); M. Hou (CHN); X. Jia (F); C. Lecoutre (F); F. Ludewig (B); S. Luding (NL); S. Merminod (F); E. Opsomer (B); D. Ozcodi (E); M. Schroeter (D); **M. Sperl**; R. Stannarius (D); N. Vandewalle (B); **P. Yu**

ESA User Support

FRC Support for Columbus Multi Unser Facilities, USOC Implementation and Operations, EML
S. Schneider

FRC Support for Columbus Multi Unser Facilities, USOC Implementation and Operations, MSL
S. Steinbach

FRC Support for Columbus Multi Unser Facilities, USOC Implementation and Operations, TEMPUS 24
D. Heuskin

FRC Support for Columbus Multi Unser Facilities, USOC Implementation and Operations, TEMPUS 25
S. Klein

Industry

MSL-EML Development and Procurement of the Experiment Part of the Science Reference Simulator Phase C2/D
S. Schneider (Astrium; 2008–2014)

EML Ground Support Program Phase 2 – MP
S. Schneider (Astrium; 2011–2014)

Entwicklung und wissenschaftliche Erprobung eines Hochtemperaturofens für Diffusionsexperimente bis zu 1600 °C unter Mikrogravitation
A. Meyer (Astrium; 2012–2015)

Update Testmodell Sample Coupling Electronics (SCE), Modul zur elektrischen Leitfähigkeitsmessung innerhalb der elektromagnetischen Levitationsanlage für die ISS
G. Lohöfer (Astrium; 2012–2015)

Metallographische Schliffe
M. Kolbe (Gebrüder Kufferath AG; 2013–2014)

Advanced Research on Silicon Nucleation in Europe (ARSINE)
D. Herlach (RGS; 2013–2015)

PEEK-Bauteile
D. Neuhaus (Vacuum Barrier Systems; 2014)

Herstellung Öfen (Graphit, Al2O3) mit Flugproben für MAXUS-9
F. Kargl (SSC; 2014–2016)

Deutsche Forschungsgemeinschaft (DFG)

Transport Processes in Melts under External Fields
Th. Voigtmann; Project within the Zukunftskolleg der Universität Konstanz, funded through the DFG Excellence Initiative
(2009–2014)

Nonlinear mechanical response of supercooled melts under applied stress
Th. Voigtmann; M. Fuchs, Universität Konstanz
Project in the Research Unit FOR1394: Nonlinear Response to Probe Vitrification (2010–2013; renewed 2013–2016)

Slow dynamics in homogeneously driven granular systems
M. Sperl; A. Zippelius, Universität Göttingen
Project in the Research Unit FOR1394: Nonlinear Response to Probe Vitrification (2010–2013; renewed 2013–2016)

Structural Arrest in Multicomponent Glass-forming Zr-melts
A. Meyer; F. Faupel, Universität Kiel
(2011–2015)

Untersuchungen zum anomalen dendritischen Wachstum in unterkhlten Schmelzen von Al-Ni und Cu-Zr Legierungen
D. M. Herlach (2011–2014)

Thermophysical Properties of Al-Si-Mg-Cu melts
B. Hallstedt, RWTH Aachen; **J. Brillo**; R. Schmid-Fetzer, TU Clausthal; T. Hickel, J. Neugebauer, MPIE Düsseldorf; M. Rettenmayr, Universität Jena
DFG Paketantrag PAK461: Integrated approach to develop thermodynamic and thermophysical key data for solidification of aluminium alloys
(2012–2014)

Electrostatic levitation investigation of the temperature rheological and volumetric changes of Molten Zr-based bulk metallic glass forming alloys
A. Meyer; R. Busch, Universität Saarbrücken
(2012–2015)

Reaktive Benetzung an der fest/flüssig Grenzfläche im Au-Sn Legierungssystem
B. Nestler, KIT; **J. Brillo** (2013–2015)

Analyse ternärer eutektischer Mikrostrukturen durch 3D-Phasenfeldsimulationen und gerichtete Erstarrungsexperimente von AlAgCu-Legierungen
L. Ratke; B. Nestler, KIT (2013–2015)

Crystal growth velocity in deeply undercooled melts of pure Zr and glass forming Zr-based alloys
D. M. Herlach; B. Nestler, KIT; R. Liu, Yanshan University, Qinhuangdao, China (2013–2016)

Active microrheology of dense microswimmer suspensions
Th. Voigtmann (2014–2016)

Other

Nonlinear Response in Complex Fluids
Th. Voigtmann; Funding for WE-Heraeus-Seminar (Wilhelm und Else Heraeus Stiftung; 2013–2014)

FixDust Herstellung von Proben für Spulenbedampfungsprojekt der ESA
S. Klein (Universität Konstanz, 2014–2016)

11 Author Index

Page numbers in **bold face** indicate corresponding authors. Page numbers in *italic type* indicate coauthors. Authors affiliated with the institute appear in **bold face**.

DLR at a glance

DLR is the national aeronautics and space research centre of the Federal Republic of Germany. Its extensive research and development work in aeronautics, space, energy, transport and security is integrated into national and international cooperative ventures. In addition to its own research, as Germany's space agency, DLR has been given responsibility by the federal government for the planning and implementation of the German space programme. DLR is also the umbrella organisation for the nation's largest project execution organisation.

DLR has approximately 8000 employees at 16 locations in Germany: Cologne (headquarters), Augsburg, Berlin, Bonn, Braunschweig, Bremen, Goettingen, Hamburg, Juelich, Lampoldshausen, Neustrelitz, Oberpfaffenhofen, Stade, Stuttgart, Trauen, and Weilheim. DLR also has offices in Brussels, Paris, Tokyo and Washington D.C.

Institute of Materials Physics in Space

Research at DLR's Institute of Materials Physics in Space is devoted to the exploration of the fundamental mechanisms that underly liquid properties and solidification processes. Through the absence of gravitationally driven phenomena, like convection and sedimentation, investigations in weightlessness provide well-defined experimental conditions. This enables accurate measurements that allow for a benchmarking of simulation and theory, as well as a parametrization and a further development of earth-bound experiments. Embedded in a closely associated and strong ground based program with simulation, theory and experiments, the institute's research in space comprises key experiments towards an understanding of the physical mechanisms involved. This in turn forms the basis for a quantitative description of solidification processes and a computer assisted materials design from the melt.

The institute employs a team of about 55 staff members, about 38 of them scientists.

DLR **Deutsches Zentrum**
für Luft- und Raumfahrt e.V.
in der Helmholtz-Gemeinschaft

Institut für Materialphysik im Weltraum
51170 Köln

www.dlr.de/mp
e-mail: materialphysik@dlr.de